POLITECNICO DI MILANO

Dipartimento di Energia

Corso di Dottorato in Scienze e Tecnologie Energetiche e Nucleari

SILICON NANOSTRUCTURES FOR ENERGY APPLICATIONS

Tesi di dottorato di:

Erika Biserni

Relatore: Prof. A. Li Bassi

Correlatore: Dr. P. Bruno

Tutor: Dr. M. Passoni

Coordinatore del Corso di Dottorato: Prof. C. E. Bottani

XXVII Ciclo

Anno 2014

Abstract

This dissertations reports the research activity done by the author at the Center for Nano Science and Technology (CNST) of the Italian Institute of Technology (IIT) and funded by IIT through a dedicated scholarship. Focus of the work is the synthesis and characterization of silicon nanostructured thin films and their engineering to make them suitable for specific energy applications in the fields of energy production and storage.

The silicon nanostructured films are prepared by Pulsed Laser Deposition (PLD) and characterized by suitable microscopic and spectroscopic techniques to understand their properties and allow for their tailoring by means of a good control over the film features –namely, porosity at the nanoscale and formation of nanocrystals. The synthesis heads for exploitation in innovative devices with a stronger relevance being given silicon anodes for lithium-ion batteries. In addition, good confidence with the fabrication process opens the way for explorative studies on the properties of the material and the possibilities to tune them to make them suitable for application in photovoltaics and thermoelectrics.

Thanks also to a fruitful network of national and international collaborations, it was possible not only to study and engineer the material properties, but also, in the case of anodes for lithium ion batteries, to realize proper working devices.

Besides nanoporous silicon films, PLD allows to grow hierarchically nanostructured films composed of Si nanocrystals embedded in a columnar porous amorphous matrix, that can be of interest in various energetic fields, with Quantum-Dot photovoltaics being one of the most challenging ones. Nanoporous silicon, in turn, can be successfully applied in the development of nanostructured porous silicon-based anodes for Lithium-ion batteries, which is the core activity of this dissertation. The work reported discusses the investigation of innovative solutions to address the two main concerns of silicon anodes in lithium ion microbatteries, i.e. volume expansion and the formation of a stable Solid Electrolyte Intephase layer, by means of suitably designed anodes. Thanks to coupling of silicon and carbon, all the proposed anodes show very good stability over cycling, even reaching up to 1000 cycles. In all cases, the approach to fabrication is driven by the need to minimize the processing effort, both in terms of number of steps required and of temperatures involved, so as to orient the work to possible up-scaling.

Moving to larger scale production, the dissertation involves also the fabrication of silicon-based anodes using methods and techniques typical of the industrial production. On the way to large-scale fabrication of silicon-carbon anodes, this study can outline a starting point and a strategy for improvement.

Finally, nanoporous silicon can find application in the field of thermoelectric materials, since controlling the porosity provides a means to reduce the thermal conductivity of the material,

which is one of the key figures to evaluate a thermoelectric material. Following this direction, the thermal conductivity of silicon films grown by PLD is characterized.

Estratto in Lingua Italiana

L’ attività di ricerca descritta in questo lavoro di tesi è stata principalmente svolta presso il Centre for Nanoscience and Technology dell’Istituto Italiano di Tecnologia di Milano e finanziata tramite una borsa tematica. Il lavoro è incentrato sulla fabbricazione e caratterizzazione di film nanostrutturati di silicio e sulla loro ingegnerizzazione finalizzata ad applicazioni nella produzione e immagazzinamento dell’energia.

I film nanostrutturati sono preparati tramite Pulsed Laser Deposition (PLD) e caratterizzati tramite tecniche di microscopia e spettroscopia per investigarne le proprietà e consentirne quindi lo sfruttamento tramite il controllo della porosità alla nanoscala e della formazione di nanocristalli.

L’ingegnerizzazione dei film ha come obiettivo le applicazioni in campo energetico, con una maggiore rilevanza data alla realizzazione di anodi per batterie agli ioni di litio. Inoltre, l’esperienza acquisita col processo di fabbricazione e lo studio delle proprietà del materiale aprono la strada a possibili applicazioni in campo fotovoltaico e termoelettrico.

Grazie anche a una preziosa rete di collaborazioni nazionali ed internazionali, è stato possibile non solo studiare approfonditamente le proprietà del materiale, ma anche, nel caso degli anodi per batterie, realizzare dispositivi.

La tecnica di PLD consente di fabbricare anche film nanostrutturati composti da una matrice amorfa contenente nanocristalli, che possono essere di interesse per diverse applicazioni energetiche e in particolare per il fotovoltaico a quantum-dot. Nanocristalli a parte, i film di silicio nanoporoso possono essere impiegati con successo come anodi per batterie agli ioni di litio e questo è l’ambito principale di sviluppo del lavoro riportato in questa tesi. L’attività di ricerca è incentrata sullo studio di soluzioni innovative che diano risposta, con un appropriata ingegnerizzazione del film, alle due principali criticità del silicio in questo ambito: l’espansione volumetrica durante la litiazione e la formazione di uno strato di Solid Electrolyte Interphase stabile. Grazie all’accoppiamento di silicio e carbonio, tutti gli anodi presentati mostrano una eccellente stabilità durante la ciclazione, raggiungendo anche i 1000 cicli di funzionamento stabile. In tutti i casi analizzati l’approccio alla fabbricazione è guidato dalla necessità di minimizzare il “costo” di processo in termini di numero di step richiesti e di temperature coinvolte, nell’ottica di un possibile sviluppo su più larga scala.

Proprio in virtu` dell’attenzione all’approccio di larga scala, una parte dell’attività di ricerca è stata dedicata alla fabbricazione di anodi di silicio-carbonio con metodi e tecniche tipici della produzione industriale degli elettrodi di grafite, ed è qui riportata con uno studio preliminare che costituisca un punto di partenza per un possibile sviluppo industriale.

Infine, i film di silicio nanoporoso possono trovare applicazione in ambito termoelettrico, dal momento che l’introduzione e il controllo della porosità consente di ridurre, rispetto al bulk, la conducibilità termica del materiale, che è una delle grandezze cruciali per l’utilizzo di un materiale come termoelettrico. I film fabbricati per PLD sono quindi stati caratterizzati nella loro conducibilità termica per valutarne questa possibile applicazione.

Table of Contents

Introduction to the dissertation

Being silicon the most widely used material in the electronic and photovoltaic industry, thanks to its abundance, low cost and non-toxicity, specific technology has been developed and deep knowledge has been acquired on its properties, especially at the bulk scale. Only partially, however, have its properties at the nanoscale been investigated and exploited accordingly.

Besides their application in optic devices[1]–[3] (e.g. light emitting devices, filtered photodetectors), biomedical devices[4]–[7] (e.g. for drug delivery, eye diseases, tumor imaging, and tissue engineering) and in sensors[8]–[11], silicon nanostructures have the potential to be successfully used in different fields of the energy production and storage. In this framework, the work at the basis of this dissertation deals with the fabrication and characterization of porous silicon nanostructured films for energy applications.

The study, which is mainly experimental, is given a strongly applicative cut and has two parallel concerns. On the one hand, understanding the properties of the silicon nanostructured material allows for their tailoring by suitable processing. On the other hand, the synthesis heads for exploitation in innovative devices. The approach is based on the fabrication of tailored silicon nanostructures by Pulsed Laser Deposition (PLD), their characterization by suitable microscopic and spectroscopic techniques and the optimization of their functional properties for the target application. Pulsed Laser Deposition (PLD) was chosen as the physical vapour deposition technique to grow thin film silicon structures, thanks to its versatility and good achievable control over the morphology and composition of the deposited film through a careful managing of the process parameters.

The main applicative energy field explored is that of silicon anodes for lithium-ion batteries. In addition, good confidence with the fabrication process opened the way for explorative studies on the properties of the material and the possibilities to tune them to make them suitable for application in photovoltaics and thermoelectrics.

In the development of anodes for lithium ion batteries, which is the core field of this doctoral work, the study went more applicative than just explorative. Thanks also to a fruitful network of national and international collaborations, it was possible not only to study and engineer the material properties, but also to realize proper working devices.

After a short introduction of the general concepts related to lithium-ion batteries, and to the standard materials used, Chapter 1 introduces the main open issues in research on silicon anodes for lithium ion batteries.

Chapter 2 explores to some extent the possibilities to grow Si nanostructured films of different morphology by PLD and to synthesize Si nanocrystals embedded in an amorphous matrix. The main goals are the understanding and tuning of the material properties by means of a good control over its features –namely, porosity at the nanoscale and formation of nanocrystals. The deposition process is developed at room temperature; this becomes particularly advantageous if any organic substrate is involved or if the final target is to export the results to larger scale processing.

The Si nanostructures described in Chapter 2 showed characteristics and properties suitable for interesting exploitation in the field of Lithium Ion Batteries (LIB), but the issues described in Chapter1 needed to be tackled. Chapter 3 presents then four different anode architectures relying on tailoring silicon-based films produced by Pulsed Laser Deposition to overcome these difficulties. Such porous structures can accommodate the large volume expansion associated with silicon lithiation. In order to promote the formation of a stable SEI layer and improve conductivity and mechanical stability, Carbon is coupled to Si, either as a separate capping layer or as integrated in the Si film.

The interest towards industrial-scale manufacturing of LIB has led to a collaboration with the Competence-E group at the Karlsruhe Institute of technology of Karlsruhe, Germany, where the author has spent a research period of three months. The work, described in Chapter 4, focussed on the preparation of silicon-carbon anodes by slurry-based processes, commonly in use in industrial battery manufacturing. Continuity with PLD-films can be found in the scale that features the anodes developed at KIT, which are based on silicon nanoparticles and keep, also in their final structure, a nanostructured morphology.

Finally, Chapter 5 deals with the characterization of thermal conductivity of nanostructured hierarchical silicon porous films produced by PLD from the experience described in Chapter 2.

Controlling the porosity provides a means to reduce the thermal conductivity of Si with respect to the bulk material, thus opening the route to its possible application as a thermoelectric material.

To sum up, the common root to the investigations reported in this dissertation lies in the silicon nanostructures being conceptually similar the one to the other and differing in the way each one is optimized to fulfill the requirements of the specific application, with a stronger relevance being given to the work on Lithium-ion batteries.

References

[1] V. Torres-Costa and R. J. Martín-Palma, "Application of nanostructured porous silicon in the field of optics. A review," *J. Mater. Sci.*, vol. 45, no. 11, pp. 2823–2838, Feb. 2010.

[2] N. M. Ahmed, Y. Al-Douri, A. M. Alwan, A. A. Jabbar, and G. E. Arif, "Characteristics of Nanostructure Silicon Photodiode using Laser Assisted Etching," *Procedia Eng.*, vol. 53, pp. 393–399, 2013.

[3] A. K. Sharma, S. H. Zaidi, P. C. Logofatu, and S. R. J. Brueck, "Optical and electrical properties of nanostructured metal-silicon-metal photodetectors," *IEEE J. Quantum Electron.*, vol. 38, no. 12, pp. 1651–1660, Dec. 2002.

[4] R. J. Martin-Palma, "Biomedical applications of nanostructured porous silicon: a review," *J. Nanophotonics*, vol. 4, no. 1, p. 042502, Sep. 2010.

[5] F. Erogbogbo, K.-T. Yong, I. Roy, R. Hu, W.-C. Law, W. Zhao, H. Ding, F. Wu, R. Kumar, M. T. Swihart, and P. N. Prasad, "In vivo targeted cancer imaging, sentinel lymph node mapping and multi-channel imaging with biocompatible silicon nanocrystals.," *ACS Nano*, vol. 5, no. 1, pp. 413–23, Jan. 2011.

[6] F. Erogbogbo, K.-T. Yong, I. Roy, G. Xu, P. N. Prasad, and M. T. Swihart, "Biocompatible luminescent silicon quantum dots for imaging of cancer cells.," *ACS Nano*, vol. 2, no. 5, pp. 873–8, May 2008.

[7] Z. Li, Y. Chen, X. Li, T. I. Kamins, K. Nauka, and R. S. Williams, "Sequence-Specific Label-Free DNA Sensors Based on Silicon Nanowires," *Nano Lett.*, vol. 4, no. 2, pp. 245–247, Feb. 2004.

[8] P. N. Patel, V. Mishra, and A. K. Panchal, "Theoretical and experimental study of nanoporous silicon photonic microcavity optical sensor devices," *Adv. Nat. Sci. Nanosci. Nanotechnol.*, vol. 3, no. 3, p. 035016, Aug. 2012.

[9] S. Ozdemir and J. Gole, "The potential of porous silicon gas sensors," *Curr. Opin. Solid State Mater. Sci.*, vol. 11, no. 5–6, pp. 92–100, Oct. 2007.

[10] F. Demami, L. Ni, R. Rogel, A. C. Salaun, and L. Pichon, "Silicon nanowires based resistors as gas sensors," *Sensors Actuators B Chem.*, vol. 170, pp. 158–162, Jul. 2012.

[11] S. E. Lewis, J. R. DeBoer, J. L. Gole, and P. J. Hesketh, "Sensitive, selective, and analytical improvements to a porous silicon gas sensor," *Sensors Actuators B Chem.*, vol. 110, no. 1, pp. 54–65, Sep. 2005.

Chapter 1
Silicon negative electrodes in Lithium-ion batteries: an introduction

1.1 Introduction to LIB: general concepts

A battery is made of electrochemical cells that convert and store electrical energy in the form of chemical energy. To meet the voltage and current required by specific applications, the cells are connected in parallel (to increase the extracted current) or in series (to increase the voltage).

A basic cell is made of two electrodes (two materials with different positive standard reduction potentials) connected by an electronic load and an electrolyte, i.e. an ion-conducting material. During discharge, electrons flow, through the external circuit, from the negative electrode (that undergoes an oxidation reaction) to the cathode (reduction reaction), and consequently cations are attracted from the negative to the positive electrodes to which they diffuse through the electrolyte. The negative electrode generally takes the name of anode (because it provides electrons in discharge). By means of electron transfer through the external circuit, these half reactions allow then for the conversion of chemical energy to electrical energy. [1] To avoid short-circuiting a separator is put in between the two electrodes to physically prevent their direct contact while allowing ions to pass through. Short-circuiting would result in capacity loss, parasitic reactions, and heat generation. This can also lead to catastrophic situations causing fires and explosions.

Two final parts required to complete a commercial cell are the current collectors, that provide mechanical support and electrical contact to the electrode active materials. Connector strips are used to connect the positive and the negative electrodes of the single cells in a stack to a common positive and negative terminal [1], [2].

1.2 Quantities Characterizing Batteries

The quantities that characterize batteries are briefly summarized in Table 1.1

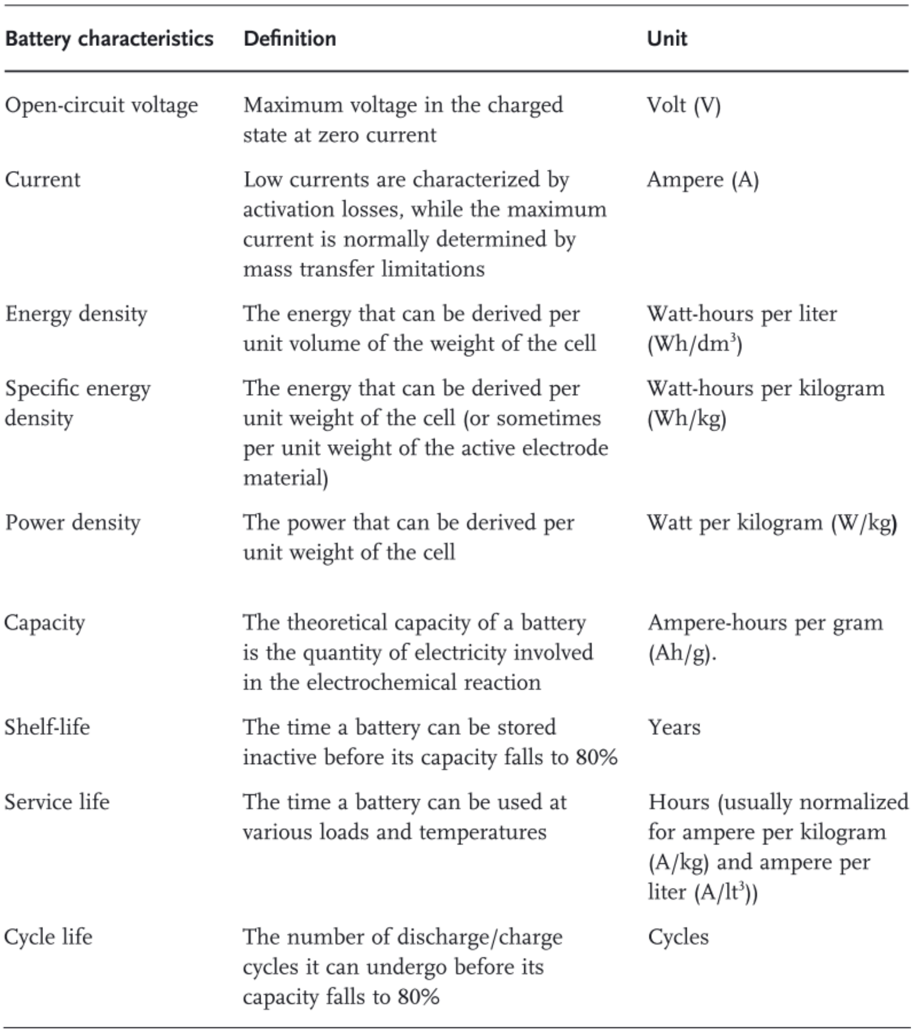

Battery characteristics	Definition	Unit
Open-circuit voltage	Maximum voltage in the charged state at zero current	Volt (V)
Current	Low currents are characterized by activation losses, while the maximum current is normally determined by mass transfer limitations	Ampere (A)
Energy density	The energy that can be derived per unit volume of the weight of the cell	Watt-hours per liter (Wh/dm^3)
Specific energy density	The energy that can be derived per unit weight of the cell (or sometimes per unit weight of the active electrode material)	Watt-hours per kilogram (Wh/kg)
Power density	The power that can be derived per unit weight of the cell	Watt per kilogram (W/kg)
Capacity	The theoretical capacity of a battery is the quantity of electricity involved in the electrochemical reaction	Ampere-hours per gram (Ah/g).
Shelf-life	The time a battery can be stored inactive before its capacity falls to 80%	Years
Service life	The time a battery can be used at various loads and temperatures	Hours (usually normalized for ampere per kilogram (A/kg) and ampere per liter (A/lt^3))
Cycle life	The number of discharge/charge cycles it can undergo before its capacity falls to 80%	Cycles

Table 1.1. Some key quantities characterizing batteries[1]

Cell voltage

The theoretical standard cell voltage, E0 (cell) is given by the difference between the standard electrode potential of the cathode, E0(cathode), and of the anode, E0(anode) as:

$$E_0(cell) = E_0(cathode) - E_0(anode) \quad [1]$$

The theoretical cell voltage is modified by the Nernst equation, which takes into account the nonstandard state of the reacting component. The Nernstian potential will change with time ; then, the nominal voltage is determined by the cell chemistry at any given point of time. The operating voltage produced is further modified as a result of discharge reactions actually taking place and will always be lower than the theoretical voltage due to polarization and the resistance losses (IR drop) of the cell.

Kinetic factors should also be considered to gain a better understanding of what the actual cell voltage may be, since the charge transfer and the rates of the reactions at the electrodes are usually the limiting factors. Usually, at low current densities overpotential losses arise from an activation energy barrier related to electron transfer reactions, while at a higher current density, the transport of ions becomes rate limiting giving rise to a current limit. In addition, ohmic losses increase with increasing current, and can be further enhanced by the increased formation of insulating phases during the progress of charging.

Capacity

The theoretical capacity of a cell is the quantity of charge that can be stored in the device.

The capacity is often expressed as specific capacity, in terms of the mass taken as reference, or as areal capacity with reference to the active area of an electrode (this quantity is used generally for microbattery applications at the level of electrode materials development).

It is important to note that the mass entering the gravimetric capacity calculation may refer to the final battery mass including packaging or it may be reported with respect to the mass of the electroactive components alone. In practice, the full battery capacity could never be realized, as there is a significant mass contribution from nonreactive components such as separators, electrolytes, current collectors and substrates, as well as packaging. Additionally, the chemical reactions cannot be carried out to completion, either due to unavailability of reactive components, inaccessibility of active materials or poor reactivity at the electrode/electrolyte interface. Moreover, the capacity is strongly dependent upon the load and can decrease rapidly at high drain rates, due to increased overpotential losses and ohmic losses (at higher drain rates, i.e. high operating currents, a cell is discharged faster). An active component may also be less available due to side reactions, such as formation of passivation layers on the active components, the so-called Solid Electrolyte Interphase (SEI) layer.

Specific Energy Density and Power Density

The specific energy density, Wh/kg, is the energy that can be derived per unit mass of the cell (or sometimes per unit mass of the active electrode material). It is the product of the specific capacity and the operating voltage in one full discharge cycle. Both the current and the voltage may vary within a discharge cycle and, therefore, the specific energy, E is calculated by integrating the product of the current and the voltage over time: $E = \int VI\, dt$.

1.3 Lithium Ion batteries

Li-ion cell is a cell where the ionic species that inserts and deinserts in the two electrodes is Li+.
The active anode material in commercial cells is graphitic carbon, because Li ions can reversibly intercalate into (forming the intercalation compound LiC_6) and deintercalate from the sheets of graphite without significant volume changes.

The active cathode material is usually an oxide of a transition metal that can coordinate Li, and the most widely studied cathode materials include $LiCoO_2$, $LiNiO_2$, and $LiMn_2O_4$, with $LiCoO_2$ being widely diffused in commercial batteries. Recently, due to its low decomposition temperature (180°C), $LiCoO_2$ has been replaced for by NMC materials (oxides containing Ni, Mg and Co) to improve battery safety.

All Li-ion cells employ non-aqueous electrolytes with a lithium-containing salts ($LiPF_6$, Li-TFSI or other salts) dissolved in solvent mixtures of organic liquids, such as EC, PC, diethyl carbonate (DEC), or ethyl methyl carbonate (EMC). LiPF6 currently is the most widely used salt. However, it reacts with trace amounts of water in solution to produce HF, which is shown to have a detrimental effect on the stability of the anode materials.
Besides the salts and solvents, additives are also used to modify the reactivity of the anode as well as to reduce the flammability of the electrolyte. Numerous options for the choice of salts and/or solvents in such batteries are known to exist in the marketplace and recently also solid polymer electrolytes have been used.
The quality of the electrolytes is very important to a Li-ion cell. During the charging process, when Li ions intercalate into the anode material, electrolyte solution is reduced to form a passivation film on the anode, the solid electrolyte interphase (SEI). Although the mechanism of the SEI formation are still to be fully understood in some electrolyte-electrode couples, it is clear that to be beneficial to the anode operation, the SEI is should be an electron insulator while allowing Li

ions to penetrate freely, so as to stabilize the anode. It is worth mentioning here that the SEI formation involves part of the active material, that then becomes inactive and does no longer take part in lithiation processes.

1.4 Silicon negative electrodes in LIB

In order to address power and energy demands of mobile electronics and electric cars, Li-ion technology is urgently being optimized by using alternative materials, with nanostructuring being a key means to open new opportunities in terms of energy density, high rate of charge and discharge, and better cyclability [3]. In particular, with rapid advances in the fields of microelectronic devices, microsensors, micromachines, RF-ID tags, MEMS, and drug delivery systems, the development of integrated power sources that enable the continued device operation is of great importance. To meet these demanding applications, microbatteries with high energy and power per unit area are urgently required and in this context, lithium-ion technology is very promising. It is more important for microbatteries to achieve high capacity per footprint (mAh cm^{-2}) than per unit weight (mAh g^{-1}) or volume (mAh L^{-1}) [4], [5]. In addition, the microbattery fabrication process should be compatible with state-of-the-art integrated circuit (IC) techniques, to lower the cost.

In order to further improve the areal capacity of microbatteries, three-dimensional (3D) nanostructured electrodes have been developed and investigated [6]–[11] which are generally realized by vacuum deposition or electroplating of active material onto a 3D metallic current collector, usually made of Ni or Ti, which are more expensive than conventional Al and Cu foils. In addition, 3D electrode fabrication usually involves wet chemistry, such as hydrothermal synthesis or etching, which is not compatible with the current IC technology. Therefore, when taking cost, complexity, and incompatibility into consideration, 3D nanostructured electrodes need more development to pitch into the microbattery market.

Besides the 3D concept, research is also heading for different materials with higher capacity.

As far as the anode material is concerned, commercial graphite shows excellent capacity retention during battery cycling; nevertheless, despite its good cycling stability and low cost, the low theoretical capacity of 372 mAh g^{-1} can be insufficient for the huge demands of the next generation of high energy density electronic devices as well as electric vehicles [12]. To meet the requirements, several elements that can reversibly alloy with lithium were investigated, including Si, Sn, Al, Ge, as well as mixed compounds thereof [13]–[16]. Because of its exceptional theoretical capacity, silicon is one of the most promising candidates among these elements to be used as anode material and has recently attracted very much attention.

Silicon alloys with lithium up to $Li_{15}Si_4$ [17], [18] at room temperature, this resulting in almost 10 times larger a capacity (3579 mAh g^{-1} for $Li_{15}Si_4$) than that of graphite (372 mAh g^{-1} [19]), which is the standard commercial material for negative electrodes. However, slurry coating of Si-based anodes is mainly facing two drawbacks. First, they suffer from poor cycle life due to detrimental volume changes (i.e., theoretically up to 280% volume expansion [20]) of the host lattice upon alloying and de-alloying with Li. Extended fractures lead to a complete loss of electrical contact between active material and current collector and to pulverization. Second, the SEI layer formed by silicon in contact with common electrolytes is generally unstable and it detrimentally impacts the capacity retention[21], [22].

At the state of the art, research works on strategies to cope with Si cracking, such as replacing bulk with porous materials [23], engineering the empty space [24], reducing amorphization-induced mechanical stresses by using non-crystalline silicon [17], [25]–[27] or fabricating composite anodes where Si is mixed with other less-active materials that can buffer its volume expansion [28].

Nanostructuring, introduction of voids and addition of other active materials having lower capacity (e.g., carbon) are the main routes currently being explored to bypass this problem.

More in detail, nanoporous silicon has been investigated as a suitable material for enhancing LIB performances, because he introduction of voids in the silicon anode can face the detrimental effects of volume variation [24], [29], [30]; indeed, depending on their size and distribution, pores can effectively accommodate the expansion during lithiation, as described by Wu and Cui [31]. Usually, porous silicon is obtained from bulk via electrochemical etching with hydrofluoric acid; the porous film is then used either as it is [23] or after ball-milling and mixing with other materials, such as C polymeric binders [32]–[36]. The advantages of nanostructuring have been evidenced in recent works [28], [37], [38] which demonstrated the existence of a threshold dimension in silicon particles that prevents from crack propagation upon lithiation.

Recently, Liu et al. [39] adopted the strategy of covering Si nanoparticles with a thin C layer that acts as a stable interface towards the electrolyte; in addition, their pomegranate-inspired design aims to engineering some void space within the core-shell structure for Si to expand.

Combining Si with other less-lithium-active materials is introduced as an effective strategy [28]. Examples show that SiO_2 coating on Si improves capacity retention during cycling by buffering volume expansion and confining the detrimental activity of HF possibly evolving from electrolyte decomposition [40]–[42]. Even more promising is the route of composite anodes made of Si and C, whether they be in the form of mixed micrometrical-sized powders with C black and other additives [43]–[47], or in especially designed 3D nanostructures where C covers Si as a shell [31], [48]–[52]. However, the sophisticated methodologies reported in these latter works generally require the use of expensive and extremely hazardous chemicals, such as HF or SiH_4 gas, and multistep treatments to tailor the anode nanostructure.

In alternative, physical vapour techniques are used to grow silicon nanostructures, as for example the Vapour-liquid-solid method for 1D-nanorods [50] or the Glancing Angle Deposition. This latter allows to grow porous silicon in the form of columnar films to enhance its electronic transport [53], introducing, though, limitation in its thickness (300 to 500nm).

So far, silicon planar thin-film anodes for microbatteries can only be realized within sub-µm thickness [33], [53]–[56], leading to low areal capacity. Therefore, it is of importance to develop Si thin film anodes with enhanced areal capacity compared to 3D nanostructured electrodes, meanwhile offering a long and stable lifetime by managing mechanical instability due to volume changes.

1.5 Objectives of this dissertation

In this framework, this dissertation discusses an investigation of innovative solutions to address the two main drawbacks of silicon anodes in lithium ion microbatteries, i.e. volume expansion and SEI, by means of suitably designed anodes.

The Si nanostructures synthesized by PLD and thoroughly characterized, as described in Chapter 2, show in fact characteristics and properties suitable for interesting exploitation in this field and have been then optimized for this purpose. Amorphous nanoporous Si films have been produced by Pulsed Laser Deposition at room temperature to be used as anodes in LIB. Such porous structures offer a large surface area to volume ratio, which can accommodate the large volume expansion associated with silicon lithiation. Then, in order to promote the formation of a stable SEI layer and improve conductivity and mechanical stability, Carbon has been coupled to Si, either as a separate capping layer or as integrated in the Si film. In these composite anode architecture, the Si hierarchical nanostructure was deposited by PLD and C either by Chemical Vapour Deposition (CVD) or by PLD.

References

[1] K. E. Aifantis, S. A. Hackney, and R. V. Kumar, *High Energy Density Lithium Batteries*. Weinheim, Germany: Wiley-VCH Verlag GmbH & Co. KGaA, 2010.

[2] "University of Cambridge (2005) DoIT- PoMS Teaching and Learning Packages." [Online]. Available: Http://www.doitpoms.ac.uk/tlplib/batteries/basic_principles.php.

[3] H. Li, Z. Wang, L. Chen, and X. Huang, "Research on Advanced Materials for Li-ion Batteries," *Adv. Mater.*, vol. 21, no. 45, pp. 4593–4607, Dec. 2009.

[4] A. Patil, V. Patil, D. Wook Shin, J.-W. Choi, D.-S. Paik, and S.-J. Yoon, "Issue and challenges facing rechargeable thin film lithium batteries," *Mater. Res. Bull.*, vol. 43, no. 8–9, pp. 1913–1942, Aug. 2008.

[5] T. Jimbo, P. Kim, and K. Suu, "Production Technology for Thin-film Lithium Secondary Battery," *Energy Procedia*, vol. 14, pp. 1574–1579, Jan. 2012.

[6] W. Wei, G. Oltean, C.-W. Tai, K. Edström, F. Björefors, and L. Nyholm, "High energy and power density TiO2 nanotube electrodes for 3D Li-ion microbatteries," *J. Mater. Chem. A*, vol. 1, no. 28, p. 8160, Jun. 2013.

[7] W. Wang, M. Tian, A. Abdulagatov, S. M. George, Y.-C. Lee, and R. Yang, "Three-dimensional Ni/TiO2 nanowire network for high areal capacity lithium ion microbattery applications.," *Nano Lett.*, vol. 12, no. 2, pp. 655–60, Feb. 2012.

[8] J. Zhu, J. Jiang, Y. Feng, G. Meng, H. Ding, and X. Huang, "Three-dimensional Ni/SnOx/C hybrid nanostructured arrays for lithium-ion microbattery anodes with enhanced areal capacity.," *ACS Appl. Mater. Interfaces*, vol. 5, no. 7, pp. 2634–40, Apr. 2013.

[9] Y. Liu, W. Zhang, Y. Zhu, Y. Luo, Y. Xu, A. Brown, J. N. Culver, C. A. Lundgren, K. Xu, Y. Wang, and C. Wang, "Architecturing hierarchical function layers on self-assembled viral templates as 3D nano-array electrodes for integrated Li-ion microbatteries.," *Nano Lett.*, vol. 13, no. 1, pp. 293–300, Jan. 2013.

[10] M. Roberts, P. Johns, J. Owen, D. Brandell, K. Edstrom, G. El Enany, C. Guery, D. Golodnitsky, M. Lacey, C. Lecoeur, H. Mazor, E. Peled, E. Perre, M. M. Shaijumon, P. Simon, and P.-L. Taberna, "3D lithium ion batteries—from fundamentals to fabrication," *J. Mater. Chem.*, vol. 21, no. 27, p. 9876, Jun. 2011.

[11] A. Lamberti, N. Garino, A. Sacco, S. Bianco, D. Manfredi, and C. Gerbaldi, "Vertically aligned TiO2 nanotube array for high rate Li-based micro-battery anodes with improved durability," *Electrochim. Acta*, vol. 102, pp. 233–239, Jul. 2013.

[12] Q. Si, K. Hanai, T. Ichikawa, A. Hirano, N. Imanishi, Y. Takeda, and O. Yamamoto, "A high performance silicon/carbon composite anode with carbon nanofiber for lithium-ion batteries," *J. Power Sources*, vol. 195, no. 6, pp. 1720–1725, Mar. 2010.

[13] T. T. Fister, J. Esbenshade, X. Chen, B. R. Long, B. Shi, C. M. Schlepütz, A. a. Gewirth, M. J. Bedzyk, and P. Fenter, "Lithium Intercalation Behavior in Multilayer Silicon Electrodes," *Adv. Energy Mater.*, vol. 4, no. 7, p. 1301494, May 2014.

[14] W. Li, Z. Yang, J. Cheng, X. Zhong, L. Gu, and Y. Yu, “Germanium nanoparticles encapsulated in flexible carbon nanofibers as self-supported electrodes for high performance lithium-ion batteries.,” *Nanoscale*, vol. 6, no. 9, pp. 4532–7, May 2014.

[15] S. Goriparti, E. Miele, F. De Angelis, E. Di Fabrizio, R. Proietti Zaccaria, and C. Capiglia, “Review on recent progress of nanostructured anode materials for Li-ion batteries,” *J. Power Sources*, vol. 257, pp. 421–443, Jul. 2014.

[16] Y. Liu, R. Ma, Y. He, M. Gao, and H. Pan, “Synthesis, Structure Transformation, and Electrochemical Properties of Li 2 MgSi as a Novel Anode for Li-Ion Batteries,” *Adv. Funct. Mater.*, vol. 24, no. 25, pp. 3944–3952, Jul. 2014.

[17] M. N. Obrovac and L. Christensen, “Structural Changes in Silicon Anodes during Lithium Insertion/Extraction,” *Electrochem. Solid-State Lett.*, vol. 7, no. 5, p. A93, May 2004.

[18] Y. H. Xu, G. P. Yin, and P. J. Zuo, “Geometric and electronic studies of Li15Si4 for silicon anode,” *Electrochim. Acta*, vol. 54, no. 2, pp. 341–345, Dec. 2008.

[19] Y. Kubota, M. C. S. Escaño, H. Nakanishi, and H. Kasai, “Crystal and electronic structure of Li15Si4,” *J. Appl. Phys.*, vol. 102, no. 5, p. 053704, 2007.

[20] M. N. Obrovac and L. J. Krause, “Reversible Cycling of Crystalline Silicon Powder,” *J. Electrochem. Soc.*, vol. 154, no. 2, p. A103, 2007.

[21] D. E. Arreaga-Salas, A. K. Sra, K. Roodenko, Y. J. Chabal, and C. L. Hinkle, “Progression of Solid Electrolyte Interphase Formation on Hydrogenated Amorphous Silicon Anodes for Lithium-Ion Batteries,” *J. Phys. Chem. C*, vol. 116, no. 16, pp. 9072–9077, Apr. 2012.

[22] M. Nie, D. P. Abraham, Y. Chen, A. Bose, and B. L. Lucht, “Silicon Solid Electrolyte Interphase (SEI) of Lithium Ion Battery Characterized by Microscopy and Spectroscopy,” *J. Phys. Chem. C*, vol. 117, no. 26, pp. 13403–13412, Jul. 2013.

[23] J. Zhu, C. Gladden, N. Liu, Y. Cui, and X. Zhang, “Nanoporous silicon networks as anodes for lithium ion batteries.,” *Phys. Chem. Chem. Phys.*, vol. 15, no. 2, pp. 440–3, Jan. 2013.

[24] H. Wu, G. Zheng, N. Liu, T. J. Carney, Y. Yang, and Y. Cui, “Engineering empty space between Si nanoparticles for lithium-ion battery anodes.,” *Nano Lett.*, vol. 12, no. 2, pp. 904–9, Feb. 2012.

[25] L. Y. Beaulieu, K. W. Eberman, R. L. Turner, L. J. Krause, and J. R. Dahn, “Colossal Reversible Volume Changes in Lithium Alloys,” *Electrochem. Solid-State Lett.*, vol. 4, no. 9, p. A137, Sep. 2001.

[26] X. H. Liu, J. W. Wang, S. Huang, F. Fan, X. Huang, Y. Liu, S. Krylyuk, J. Yoo, S. A. Dayeh, A. V Davydov, S. X. Mao, S. T. Picraux, and S. Zhang, “In situ atomic-scale imaging of electrochemical lithiation in silicon,” *Nat. Nanotechnol.*, vol. 7, no. November 2012, pp. 749–756, 2012.

[27] H. Xia, S. Tang, and L. Lu, “Properties of amorphous Si thin film anodes prepared by pulsed laser deposition,” *Mater. Res. Bull.*, vol. 42, no. 7, pp. 1301–1309, Jul. 2007.

[28] J. R. Szczech and S. Jin, “Nanostructured silicon for high capacity lithium battery anodes,” *Energy Environ. Sci.*, vol. 4, no. 1, p. 56, 2011.

[29] S. R. Gowda, V. Pushparaj, S. Herle, G. Girishkumar, J. G. Gordon, H. Gullapalli, X. Zhan, P. M. Ajayan, and A. L. M. Reddy, “Three-dimensionally engineered porous silicon electrodes for li ion batteries.,” *Nano Lett.*, vol. 12, no. 12, pp. 6060–5, Dec. 2012.

[30] Y. Zhao, X. Liu, H. Li, T. Zhai, and H. Zhou, “Hierarchical micro/nano porous silicon Li-ion battery anodes.,” *Chem. Commun. (Camb).*, vol. 48, no. 42, pp. 5079–81, May 2012.

[31] H. Wu and Y. Cui, “Designing nanostructured Si anodes for high energy lithium ion batteries,” *Nano Today*, vol. 7, no. 5, pp. 414–429, 2012.

[32] M. Thakur, S. L. Sinsabaugh, M. J. Isaacson, M. S. Wong, and S. L. Biswal, “Inexpensive method for producing macroporous silicon particulates (MPSPs) with pyrolyzed polyacrylonitrile for lithium ion batteries.,” *Sci. Rep.*, vol. 2, p. 795, Jan. 2012.

[33] M. He, Q. Sa, G. Liu, and Y. Wang, “Caramel popcorn shaped silicon particle with carbon coating as a high performance anode material for Li-ion batteries.,” *ACS Appl. Mater. Interfaces*, vol. 5, no. 21, pp. 11152–8, Nov. 2013.

[34] H. Li, “A High Capacity Nano-Si Composite Anode Material for Lithium Rechargeable Batteries,” *Electrochem. Solid-State Lett.*, vol. 2, no. 11, p. 547, Nov. 1999.

[35] J. Li, R. B. Lewis, and J. R. Dahn, “Sodium Carboxymethyl Cellulose,” *Electrochem. Solid-State Lett.*, vol. 10, no. 2, p. A17, 2007.

[36] G. Liu, S. Xun, N. Vukmirovic, X. Song, P. Olalde-Velasco, H. Zheng, V. S. Battaglia, L. Wang, and W. Yang, “Polymers with tailored electronic structure for high capacity lithium battery electrodes.,” *Adv. Mater.*, vol. 23, no. 40, pp. 4679–83, Oct. 2011.

[37] X. H. Liu, L. Zhong, S. Huang, S. X. Mao, T. Zhu, and J. Y. Huang, “Size-dependent fracture of silicon nanoparticles during lithiation,” *ACS Nano*, vol. 6, no. 2, pp. 1522–31, Mar. 2012.

[38] S. Kalnaus, K. Rhodes, and C. Daniel, “A study of lithium ion intercalation induced fracture of silicon particles used as anode material in Li-ion battery,” *J. Power Sources*, vol. 196, no. 19, pp. 8116–8124, Oct. 2011.

[39] N. Liu, Z. Lu, J. Zhao, M. T. McDowell, H.-W. Lee, W. Zhao, and Y. Cui, “A pomegranate-inspired nanoscale design for large-volume-change lithium battery anodes,” *Nat. Nanotechnol.*, no. February, pp. 2–7, Feb. 2014.

[40] T. Kawamura, A. Kimura, M. Egashira, S. Okada, and J.-I. Yamaki, “Thermal stability of alkyl carbonate mixed-solvent electrolytes for lithium ion cells,” *J. Power Sources*, vol. 104, no. 2, pp. 260–264, 2002.

[41] M. Broussely, P. Biensan, F. Bonhomme, P. Blanchard, S. Herreyre, K. Nechev, and R. J. Staniewicz, “Main aging mechanisms in Li ion batteries,” *J. Power Sources*, vol. 146, no. 1, pp. 90–96, 2005.

[42] J. Vetter, P. Novák, M. R. Wagner, C. Veit, K.-C. Möller, J. O. Besenhard, M. Winter, M. Wohlfahrt-Mehrens, C. Vogler, and A. Hammouche, “Ageing mechanisms in lithium-ion batteries,” *J. Power Sources*, vol. 147, no. 1, pp. 269–281, 2005.

[43] C. Erk, T. Brezesinski, H. Sommer, R. Schneider, and J. Janek, “Toward silicon anodes for next-generation lithium ion batteries: a comparative performance study of various polymer binders and silicon nanopowders.,” *ACS Appl. Mater. Interfaces*, vol. 5, no. 15, pp. 7299–307, Aug. 2013.

[44] S. D. Beattie, D. Larcher, M. Morcrette, B. Simon, and J.-M. Tarascon, “Si Electrodes for Li-Ion Batteries—A New Way to Look at an Old Problem,” *J. Electrochem. Soc.*, vol. 155, no. 2, p. A158, 2008.

[45] M. Holzapfel, H. Buqa, L. J. Hardwick, M. Hahn, A. Würsig, W. Scheifele, P. Novák, R. Kötz, C. Veit, and F.-M. Petrat, “Nano silicon for lithium-ion batteries,” *Electrochim. Acta*, vol. 52, no. 3, pp. 973–978, Nov. 2006.

[46] N. S. Hochgatterer, M. R. Schweiger, S. Koller, P. R. Raimann, T. Wöhrle, C. Wurm, and M. Winter, “Silicon/Graphite Composite Electrodes for High-Capacity Anodes: Influence of Binder Chemistry on Cycling Stability,” *Electrochem. Solid-State Lett.*, vol. 11, no. 5, p. A76, 2008.

[47] W.-R. Liu, M.-H. Yang, H.-C. Wu, S. M. Chiao, and N.-L. Wu, “Enhanced Cycle Life of Si Anode for Li-Ion Batteries by Using Modified Elastomeric Binder,” *Electrochem. Solid-State Lett.*, vol. 8, no. 2, p. A100, 2005.

[48] B. Wang, X. Li, X. Zhang, B. Luo, Y. Zhang, and L. Zhi, “Contact-engineered and void-involved silicon/carbon nanohybrids as lithium-ion-battery anodes.,” *Adv. Mater.*, vol. 25, no. 26, pp. 3560–5, Jul. 2013.

[49] B. Wang, X. Li, T. Qiu, B. Luo, J. Ning, J. Li, X. Zhang, M. Liang, and L. Zhi, “High volumetric capacity silicon-based lithium battery anodes by nanoscale system engineering.,” *Nano Lett.*, vol. 13, no. 11, pp. 5578–84, Nov. 2013.

[50] C. K. Chan, H. Peng, G. Liu, K. McIlwrath, X. F. Zhang, R. a Huggins, and Y. Cui, “High-performance lithium battery anodes using silicon nanowires,” *Nat. Nanotechnol.*, vol. 3, no. 1, pp. 31–5, Jan. 2008.

[51] J. Song, S. Chen, M. Zhou, T. Xu, D. Lv, M. L. Gordin, T. Long, M. Melnyk, and D. Wang, “Micro-sized silicon–carbon composites composed of carbon-coated sub-10 nm Si primary particles as high-performance anode materials for lithium-ion batteries,” *J. Mater. Chem. A*, vol. 2, no. 5, pp. 1257–1262, 2014.

[52] H. Kim and J. Cho, “Superior lithium electroactive mesoporous Si@carbon core-shell nanowires for lithium battery anode material.,” *Nano Lett.*, vol. 8, no. 11, pp. 3688–91, Nov. 2008.

[53] M. D. Fleischauer, J. Li, and M. J. Brett, “Columnar Thin Films for Three-Dimensional Microbatteries,” *J. Electrochem. Soc.*, vol. 156, no. 1, p. A33, 2009.

[54] H. Jung, M. Park, Y.-G. Yoon, G.-B. Kim, and S.-K. Joo, “Amorphous silicon anode for lithium-ion rechargeable batteries,” *J. Power Sources*, vol. 115, no. 2, pp. 346–351, Apr. 2003.

[55] S. Ohara, J. Suzuki, K. Sekine, and T. Takamura, “A thin film silicon anode for Li-ion batteries having a very large specific capacity and long cycle life,” *J. Power Sources*, vol. 136, no. 2, pp. 303–306, Oct. 2004.

[56] H. Jung, M. Park, S. H. Han, H. Lim, and S.-K. Joo, “Amorphous silicon thin-film negative electrode prepared by low pressure chemical vapor deposition for lithium-ion batteries,” *Solid State Commun.*, vol. 125, no. 7–8, pp. 387–390, Feb. 2003.

Chapter 2

Silicon Nanostructures by Pulsed Laser Deposition

The research here described was aimed to the synthesis of silicon nanostructures by Pulsed Laser Deposition (PLD) and their characterization from a compositional, morphological and structural point of view. The main goals were the understanding and tuning of the material properties by means of a good control over its features –namely, porosity at the nanoscale and formation of nanocrystals. For some specific process conditions, the fabrication leads to a hierarchically nanostructured film composed of Si nanocrystals embedded in a columnar porous amorphous matrix. Surprisingly, not only were "bulk" crystals grown, but also amorphous-crystalline core-shell and core-shell-shell nanostructures. The content of this chapter is presented in a scientific publication ([1]*).*

2.1 Introduction to Pulsed Laser Deposition

Pulsed Laser Deposition is a Physical Vapour Deposition technique, where the vapour phase of the ablated material is generated by the interaction with an intense pulsed laser source. A typical set-up for PLD is schematically shown in Fig. 2.1.

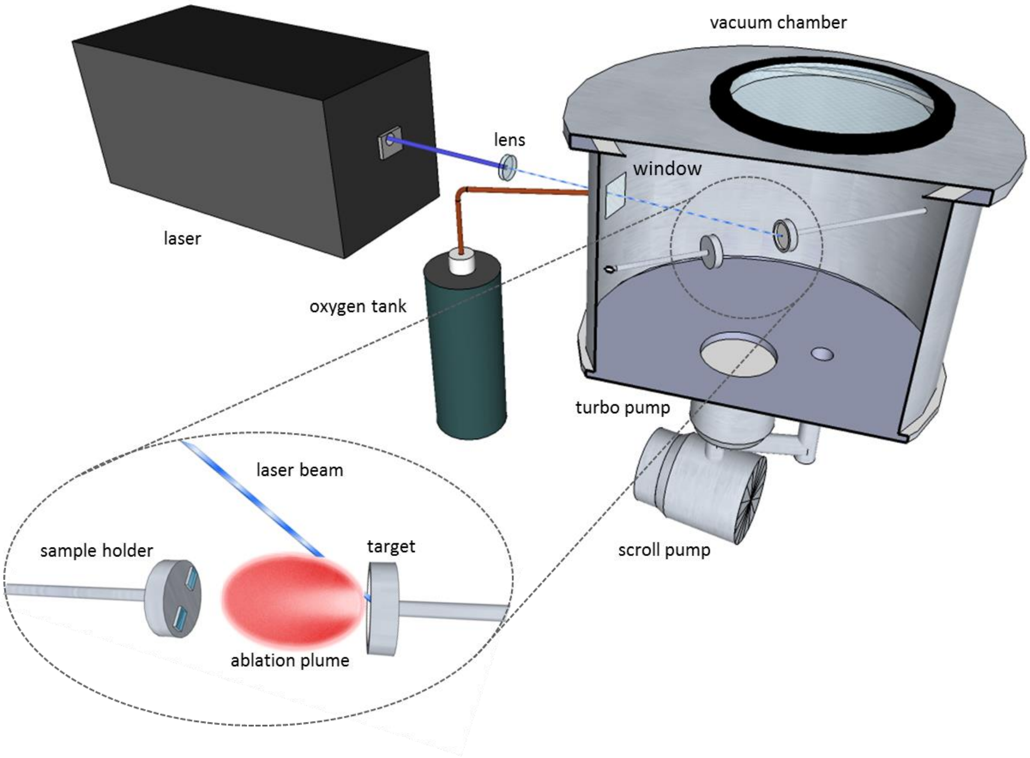

Fig 2.1: Sketch of a PLD setup [courtesy of L. Passoni and F. Garcia Ferrè]

In a high vacuum chamber, under vacuum conditions or in a low pressure of background gas, a pulsed laser beam is focussed on elementary or alloy targets. The target is usually rotated, in order to avoid repeated ablation from the same spot. During ablation, the ejected plume of plasma expands away from the interaction volume and impinges on the substrate of interest, thus allowing for film deposition.

In most cases, during deposition some droplets of target material are also deposited on the substrate surface, as reported in the literature, e.g. [2], [3], and directly experienced also in this work.

The growth and quality of the resulting film will generally depend on a number of experimental parameters, such as those characterizing ablation, e.g. laser fluence, wavelength, pulse duration and repetition rate, and those that define the interactions of ablated species, e.g. the background gas pressure (if any), the type of background gas, the kinetic energies of the various species, the target-to-substrate distance and the target temperature.

In particular, the presence of a background gas and its pressure are of great importance because they affect the film growth by defining a certain confinement of the ablation plasma plume. This confinement and the collision rate of ablated species increase with increasing background pressure, resulting in cluster nucleation and reduction of kinetic energies of the species that are collected on the substrate[4]. In addition, the choice of the background gas defines whether the deposition be reactive (e.g. the growth of oxides starting from metallic targets in oxygen atmosphere) or not and the different molecular weight of the background gas will determine the kinetics of the process.

The possibility of working with ideally any target materials even of complex stoichiometry, together with the degrees of freedom given by all of the above mentioned parameters, make PLD a very versatile technique for the growth of materials with tailored morphology, crystalline structure and composition.

2.2 Silicon nanostructures and silicon nanocrystals: motivation and state of the art

Being silicon the most widely used material in the electronic and photovoltaic industry, thanks to its abundance, low cost and non-toxicity, specific technology has been developed and deep knowledge has been acquired on its properties, especially at the bulk scale. Only partially, however, have its properties at the nanoscale been investigated and exploited accordingly.

In the last years a renewed and increasing interest towards the optoelectronic properties of silicon nanocrystals (Si NCs) and nanostructures has been registered as far as concerns their fabrication, characterization and possible implementation in devices, such as high efficiency solar cells [5], Si NC non-volatile memories [6], biomedical devices and sensors [7], lithium batteries [8] and thermoelectric devices [9]. In particular, the need for increasing efficiency in photovoltaics is a challenging application field and the birth of the so-called 3rd generation photovoltaics has opened new research paths for the synthesis and integration of Quantum-Dots (QD) [10]–[14] that can exploit the effects of quantum confinement. Nevertheless, up to now no QD-based solar devices showing enhanced efficiency due to quantum confinement effects have been presented.

Within this frame, the research activity here reported describes an explorative study on the synthesis of amorphous silicon nanostructures with different morphology and porosity and the obtainment of silicon NCs embedded in an amorphous matrix by Pulsed Laser Deposition at room temperature.

Si NCs embedded in a thin-film matrix can possibly find their application in QD-based photovoltaic devices, but the realization of a device was out of the scopes of the work here presented.

At the state of the art, the synthesis of silicon QDs in view of photovoltaic applications has been achieved mainly by the Plasma Enhanced Chemical Vapour Deposition (PECVD) technique [15]–[17] or through chemical precipitation from colloidal solutions [18]. Recent works have been published on fabrication and characterization of silicon QDs [15], where the “superlattice approach” is explored. The idea of the superlattice consists of depositing via silane-assisted PECVD a stack of alternated layers of Si-rich and stoichiometric dielectric material (SiOx, SiC, SiNx) and let Si QDs precipitate at the interfaces upon high-temperature annealing. Sputtering has been used in a similar approach also by Conibeer, Green and Park to fabricate silicon QDs [16], [17]. However, the seeking for a process that avoids harmful materials, such as silane, and does not involve high temperature steps would be relevant especially for future developments in the field of hybrid photovoltaics (organic-inorganic solar cells) or flexible devices deposited on plastic (polymeric) or temperature-sensitive substrates. At present, though, effective strategies for low temperature synthesis of Si QDs by physical methods are still lacking. In this direction, it is worth mentioning the work done by Kortshagen and his colleagues [19], [20], who pioneered a low pressure process for the synthesis of Si NCs in a radiofrequency powered reactor. Despite the promising results of this work, headed for obtaining silicon NCs from low pressure nonthermal plasma, it is important here to stress its major drawback related to the use of silane as a gas precursor.

Pulsed Laser Deposition appears to be an interesting and promising pathway for room- or low-temperature synthesis of Si QDs. Several examples of Si nanoparticle or nanostructured layers deposited by PLD in a background atmosphere are reported in the literature [21]–[26], starting from the work of Geohegan et al. in 1998 [27]. However, direct evidence -e.g. by high resolution Transmission Electron Microscopy (TEM)- of nanoparticle crystallinity is usually lacking, unless high temperature post-deposition annealing procedures are adopted [[12], [28] and references therein]. Most works focus on the investigation of photoluminescence (PL) properties, the interpretation of which is usually complicated by ex-situ oxidation, presence of defects, amorphous phase and surface or interface states, and no clear conclusive evidence is reported of quantum confinement effects due the presence of nm-size crystalline quantum dots (e.g. in Photoluminescence or Raman spectra).

As described in paragraph 2.1, in PLD, the background gas pressure is one of the parameters that most influence the structure and morphology of the deposited material [29], [30]. Low energy cluster deposition results in the growth of a porous layer, with porosity increasing as the pressure is increased [31], [32]. One of the main drawbacks in producing Si nanostructures is their being prone to oxidation (in-situ and ex-situ), especially for the case of porous structures. Different strategies can be implemented in order to reduce oxidation, such as depositing an additive compact silicon layer on top of the film as a protective coating [33].

Recently, Umezu et al. [21], [22] have reported Si deposition by PLD in N_2 and H_2 background atmosphere and discussed the effect of surface passivation, as it is done for CVD synthesis of nano/microcrystalline thin films. However, in this case Si nanoparticles are obtained at relatively high pressure (over 250 Pa, up to 1100 Pa), which induces foam-like structures instead of films. Moreover, structural characterization such as TEM analysis is not offering a conclusive proof of the crystalline nature of the nanostructures and Raman spectra do not give evidence of confinement effects.

In the following, we show how we fabricated silicon nanostructured films by room temperature PLD. Moreover, for some process parameters, we succeeded in inducing nucleation of Si NCs embedded in the amorphous matrix, together with unique silicon amorphous-crystalline core-shell nanostructures. The crystalline quality and the density of the Si QDs have been characterized by TEM and high resolution TEM, while Raman spectroscopy provides evidence of quantum confinement effects. TEM analysis was performed by Dr. Rosaria Brescia and Ms. Alice Scarpellini of the Italian Institute of Technology, Genova, Italy.

For our work, a KrF laser beam (λ=248 nm, pulse energy 400 mJ, pulse duration 20 ns, repetition rate 20 Hz) was focused on a rotating and translating monocrystalline <100> silicon wafer target with a fluence of ~5 J/cm^2. After reaching a system base vacuum of approximately 3×10^{-3} Pa, a background gas was fluxed in the chamber during the whole deposition. In order to grow films of various morphologies, the background gas pressure for deposition ranged between 5 and 100 Pa. The gas was either pure Ar or a mixture of Ar and H_2 (<3 vol. %). The other process parameters were chosen upon optimization of the film quality in terms of reducing the formation of droplets. The substrates for film deposition were monocrystalline <100> p-type silicon wafers, covered with a 120 nm thick evaporated Al layer in the case of samples to be studied by Raman and SEM. Target-to-substrate distance was set to 50mm and during deposition the substrate holder was rotated to widen uniformity over the deposition area.

Without undergoing any post-deposition thermal processes, the samples were imaged by a Scanning Electron Microscope (SEM) and investigated by Raman spectroscopy to characterize their morphology and structure and in particular to reveal the presence of nanocrystalline phases.

Some selected samples were analysed also by Energy-Dispersive X-ray Spectra (EDS) and TEM to examine, respectively, the film chemical composition and the presence, dimension and spatial density of nanocrystalline phases in the film. All the experimental details about characterization (instruments and acquisition methods) are described in section “methods” at the end of this chapter.

2.3 Si nanostructured films by PLD

By adjusting the background gas pressure of each deposition, we were able to obtain films of different morphology, as evidenced by SEM images of the cross section of the film. The images show that, starting from dense structures, grown at relatively low gas pressure (i.e. 5 Pa, Fig.2.2 (a)), the morphology of the film develops into an algae-like columnar hierarchical structure with increasing porosity upon increasing gas pressure (Fig. 2.2 (b-e)). The influence of deposition gas pressure on the film nanoscale morphology is in full agreement with what observed for other materials, such as titanium oxide [34], and no significant differences in the evolution of film morphology are evidenced by comparing films produced in the same pressure of Ar or Ar+H_2 (Fig. 2.2 (d),(e)). In Fig. 2.2 (f) a zoomed cut of Fig. 2.2 (d) allows to appreciate the granular structure of the hierarchical film grown at 100Pa Ar+H_2.

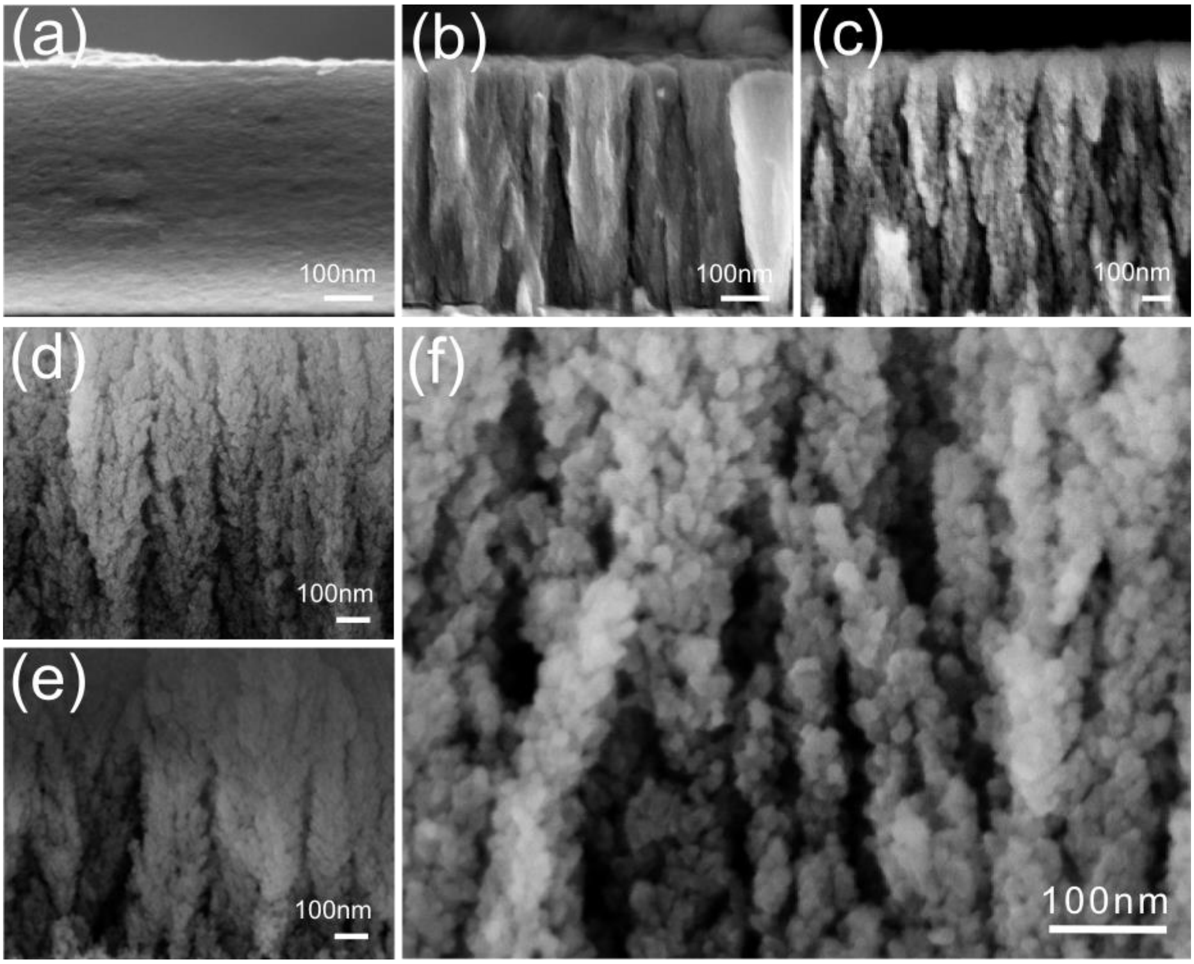

Figure 2.2: Cross section SEM images of films grown at different pressures. With increasing deposition pressure, a transition in film morphology can be observed. (a) compact structure deposited at 5Pa Ar+H_2; (b) a columnar-dense film deposited at 40Pa Ar+H2; (c) columnar porous film deposited at 60Pa Ar+H2; (d) columnar microporous algae-like film deposited at 100Pa Ar+H2 and (e) its analogous deposited at 100Pa pure Ar showing no substantial difference in morphology. In (f), zoomed image of the film deposited at 100Pa Ar+H2.

From EDS investigation on samples deposited at 100 Pa (see Table 2.1), the use of a mixture of H_2 and Ar as deposition gas instead of pure Ar is proved to have a beneficial effect on reducing the oxygen content of the film, being amorphous Si passivation by H_2 very well known in semiconductor processing [35]–[38] (a reduction factor of about 4 in oxygen content is estimated with respect to the partially oxidized analogous Si layer deposited in pure Ar). Rather than exactly assigning a value to the Si/O ratio in the two films, the EDS investigation was meant to give useful qualitative indications for improving fabrication, based on the variation in the Si/O ratio possibly induced by the mixture of H_2 in Ar. During the analysis the Al layer has never been detected, thus excluding any contribution of the silicon substrate to the EDS signal.

Sample	Si [at%]	O [at%]	Impurities (C, N) [at%]	O:Si ratio
Ar 100Pa	34,8 (+/-0,1)	58,2 (+/-1,0)	6,9 (+/-1,0)	8:5
$Ar+H_2$ 100Pa	66,6 (+/-2,5)	28,5 (+/-0,3)	4,9 (+/-1,0)	2:5

Table 2.1: Data from fitted EDS spectra for two films deposited with a background pressure of 100 Pa of pure Ar and $Ar+H_2$. The introduction of hydrogen in the gas mixture during deposition has the clear effect of reducing the oxygen content in the film through Si-H bond passivation. The oxygen to silicon ratio decreases by a factor 4 from pure Ar atmosphere (first row) to Ar+H2 atmosphere (second row).

Raman investigations evidence an amorphous structure in all of the samples but those grown at 100 Pa (both in Ar and in $Ar+H_2$), where also silicon nanocrystals are revealed. The spectra of samples produced at selected pressures from 5 to 100 Pa in $Ar+H_2$ are shown in Fig. 2.3(a).

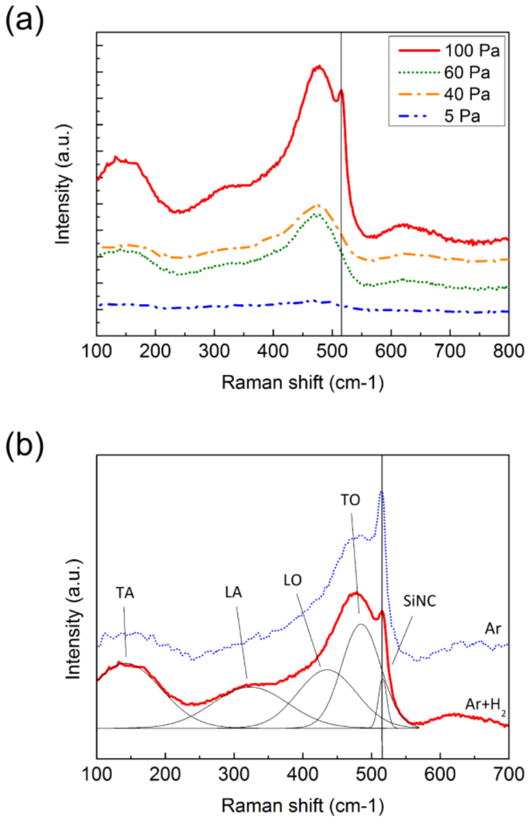

Figure 2.3: (a) Raman spectra of samples deposited at different pressures in Ar+H_2 atmosphere. **Blue dash-dot-dotted**, **green dotted** and **orange dash-dotted** (corresponding to samples deposited at 5 Pa, 40 and 60 Pa, respectively) show typical features of amorphous Si (four Gaussian bands at 142, 330, 435 and 485 cm-1 attributed to TA, LA, LO and TO modes). **Red solid** curve (sample deposited at 100Pa) shows a peak appearing at 515 cm-1, ascribable to nanocrystalline silicon (bar placed at 515 cm-1 for easier reading). (b) **Red solid curve**: Raman spectrum of a sample deposited at 100Pa Ar+H_2, well fitted by the four components of amorphous Si and an additive peak centred at 515 cm-1. **Dotted blue curve:** Raman spectrum of a sample deposited at 100Pa Ar, showing the same features as the one deposited in Ar+H_2 atmosphere.

The spectra can be well fitted by four characteristic Gaussian bands, centred around 145, 330, 430 and 490 cm^{-1}, that are generally attributed, respectively, to the transverse acoustic (TA), longitudinal acoustic (LA), longitudinal optic (LO) and transverse optic (TO) modes of amorphous silicon [39]. Crystalline bulk silicon is known to have Raman spectrum denoted by a sharp peak at 520.5 cm^{-1}, related to the TO mode.

Only in the samples produced at 100 Pa, either in Ar or in Ar+H_2, does a peak appear on top of the band referred to amorphous silicon, in a position that varies, according to the chosen point on the sample, in the range between 514 cm^{-1} and 517 cm^{-1} and with a FWHM ranging between 12 and 14.5 cm^{-1}, as can be seen in Fig. 2.3(b). This peak can be attributed to the TO mode of silicon crystals of nanometric size. The peak shift (3.5 to 6.5 cm^{-1}) and width broadening with respect to bulk crystalline silicon are agreed to be due to the quantum confinement effects via scattering of phonons away from the Brillouin zone centre (relaxation of the **q**=0 selection rule) [40], [41] .

No significant differences are detected in the spectral region under analysis for samples deposited either in pure Ar or in Ar+H_2 at the same pressure, as evidenced, e.g., by comparing the two spectra in Fig. 2.3(b). The intensity of the nanocrystalline peak varies from spot to spot on the same sample and it can be thus related to the local density of nanocrystallites under the investigation spot.

Several semi-empirical models have been proposed to relate the shift in Raman nanocrystalline peak to the dimension of the crystal itself (see [40], [42]). Using the formula proposed by He et al.[43] to estimate the crystal diameter from the peak shift,

$$d = 2\pi \left(\frac{B}{\Delta\omega}\right)^{n} ,$$

where d is the crystal diameter, $\Delta\omega$ the peak shift from bulk position, $B = 2.0$ cm^{-1}nm^2 [39], [43] and $n = 0.5$ [43], a shift of 3.5 cm^{-1} to 6.5 cm^{-1} gives a crystal size of 3.5 to 4.7 nm diameter. For more details on Raman spectroscopy, see Appendix 1.

Since no crystalline peak is traced for samples deposited at gas pressure lower than 100 Pa, we identified this value as a threshold pressure for the growth of nanocrystals under our processing conditions.

Detection of Si NCs by Raman is confirmed by TEM and High-Resolution TEM (HRTEM) investigations, that image single-crystalline spherical nanoparticles, embedded in an amorphous matrix, in both the samples fabricated at 100 Pa in Ar+H_2 and in pure Ar, i.e. over the threshold pressure.

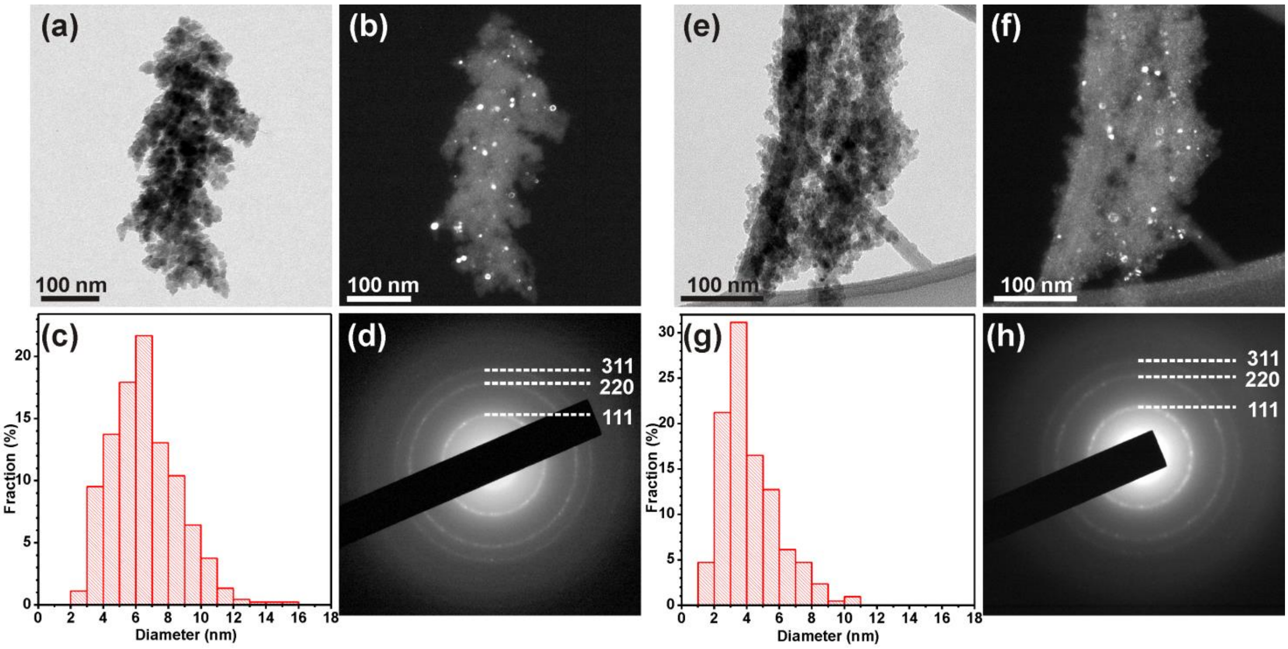

Figure 2.4: (a-d) refer to fabrication in Ar, while (e-h) to fabrication in Ar+H_2. (a, e) BF-TEM images of fragments of the two samples and (b, f) corresponding DF-TEM images, obtained by selecting a region of the inner diffraction rings. (c,g) Histograms of the particle size distribution in the two samples; the sample produced in Ar+H_2 shows smaller mean value. (d) and (h) Electronic diffraction patterns obtained by selecting the fragments in (a) and (e), respectively.

Bright field TEM (BF-TEM) (Fig. 2.4(a) for Ar and 2.4(e) for Ar+H_2) confirms the hierarchical structure observed by SEM for the film fragments, composed by ~10 nm-sized granules. Electron diffraction patterns (Fig. 2.4(d) for Ar and 2.4(h) for Ar+H_2) show rings corresponding to randomly oriented crystalline silicon grains.

Although only a weak diffraction contrast is appreciable in BF-TEM mode, dark-field (DF-TEM) images (Fig. 2.4(b), 2.5(a,c) for Ar and 2.4(f), 2.5(d,f) for Ar+H_2), clearly show that for both samples the material is formed by a matrix that includes several crystalline grains, mainly spherical (appearing bright in DF-TEM). From DF images, an average size of the crystallites can be determined as 6 (±2) nm for the sample produced in Ar and 4 (±2) nm for the sample produced in Ar+H_2, as summarized in the histograms shown in Fig. 2.4(c) for Ar and 2.4(g) for Ar+H_2. The distance of these size values from those calculated by Raman peak-shift could be due to two reasons. The one is the limits of the model adopted to evaluate quantum confinement effects in Raman scattering. The other one is the possible presence of defects in nanocrystals that introduce disorder and can thus reduce the size of coherent scattering domains.

HRTEM analyses on samples fabricated at 100 Pa in pure Ar and in Ar+H_2 confirm the presence of single-crystal Si particles, embedded in an amorphous porous matrix (Fig. 2.5(b) for Ar and 2.5(e) for Ar+H_2).

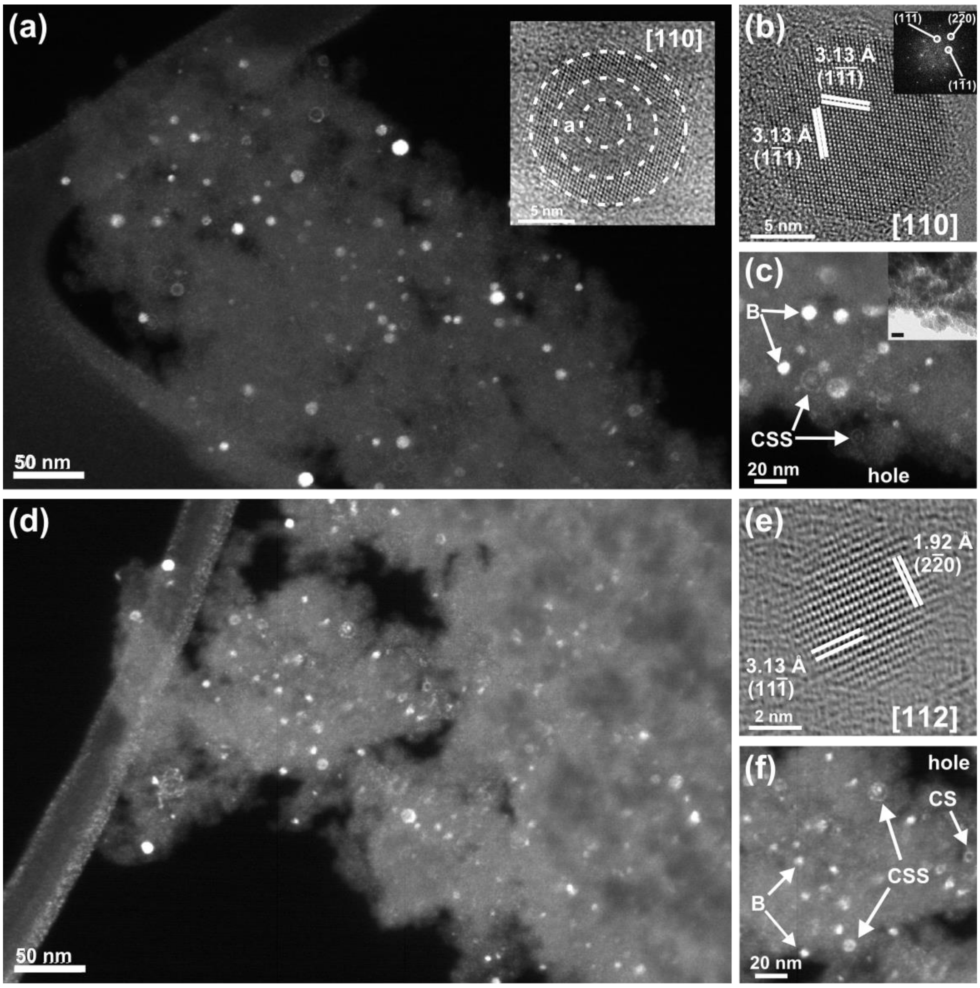

Figure 2.5: for straightforward comparison, (a-c) refer to fabrication in 100 Pa Ar, while (d-f) in 100Pa Ar+H2. (a) DF-TEM image of a region of the sample made in Ar, showing bulk nanocrystals together with CS and CSS grains, all embedded in an amorphous matrix and (c) a zoomed view of the same, where CSS and bulk grains are highlighted. The inset in (c) shows the corresponding BF-TEM image. (b) HRTEM image of a bulk grain in the same sample, with the fast Fourier transform in the inset showing the [110] pattern of single-crystal Si. (inset in (a)) HRTEM image of a core-shell-shell (CSS) crystal in the same sample, also showing [110] orientation. (d) DF-TEM image of a region of the sample made in Ar+H2 showing bulk nanocrystals together with CS and CSS grains, all embedded in an amorphous matrix and (f) a zoomed view of the same, where CS, CSS and bulk grains are highlighted. (e) HRTEM image of a bulk grain in the same sample.

Besides "bulk" nanocrystals, spherical particles of comparable size but with a more complex structure can also be found, as exhibited both by DF-TEM (bright rings or disc-ring systems, see

Figs. 2.4 (b), 2.5(a, c) for Ar and 2.4(f), 2.5(d, f) for Ar+H_2) and HRTEM analyses (inset in Fig. 2.5(a)). Upon further investigation, some of them turn out to have a unique core-shell (CS) structure, where the shell is crystalline and the core amorphous, and some of them show a thin amorphous shell in between the single-crystalline core and the outer crystalline shell (core-shell-shell, CSS). Such structures, which have never been obtained for silicon in a direct single step process, have been synthesized in this work through the PLD process.

The regions appearing dark within the CS and CSS features in DF-TEM images are not hollow, or filled with gas, but characterized by a similar composition and density as the bright regions. This is clearly demonstrated by comparing HRTEM images and Energy-Filtered TEM (EFTEM) maps of the CSS grains (Fig. 2.6(a) and (b) in Ar): all of the three regions (core, inner shell, outer shell) in the HRTEM image show the same composition, i.e. silicon, in the EFTEM maps.

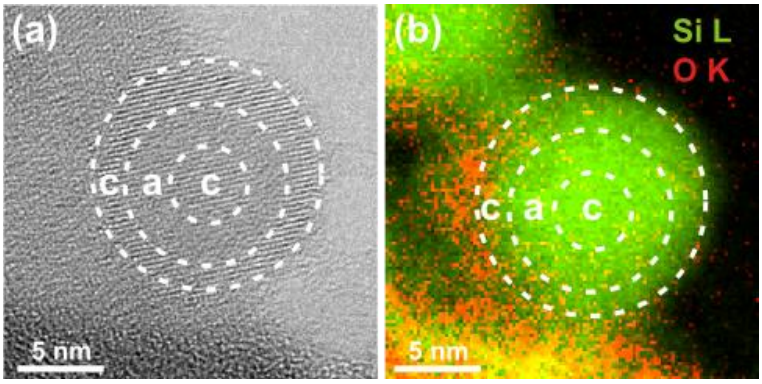

Figure 2.6: (a) HRTEM image and (b) corresponding composition of EFTEM elemental maps of O (red) and Si (green) of a CSS grain in the film grown in Ar: all of the three regions (core, inner shell, outer shell) in the HRTEM image show the same composition, i.e. mainly silicon

HRTEM observations for samples deposited at 60 Pa (not shown) confirm that crystalline nanoparticles or CS/CSS structures are absent when lower deposition pressures are employed, in agreement with Raman spectra discussed above.

Besides these observations, EFTEM elemental mapping indicates that the amorphous matrix surrounding the single-crystal grains is oxidised, as imaged in colour in Fig. 2.6(b), confirming the results obtained by EDS analysis (see above). An oxidised layer is visible (red) on the surface of Si grains (green). The sample here imaged was produced in pure Ar (no H_2) at high pressure. This sets favourable conditions for oxidation, because of two main reasons: the surface exposed to oxidation is high due to the high porosity, and no passivation effect is induced without H_2 during deposition, as proven from EDS data. Therefore, the content of oxygen in this film can be considered as an upper limit for the whole bunch of samples, since EDS measurements indicate a reduced content of oxygen in films deposited in the mixture of Ar and H_2 (H_2 <3 vol.%).

Based on the DF-TEM images, an average volume density was evaluated for the grains for both samples prepared in Ar and Ar+H_2 Based on the results of this analysis, we are able to estimate a percentage of the analyzed volume occupied by crystalline QDs of about 2% for the sample made in Ar and 0.4% for Ar+H_2 and a volumetric density of the order of $1.2 \cdot 10^5$ grains/μm^3 for the sample made in Ar and $1.0 \cdot 10^5$ for Ar+H_2. The volume of CS and CSS structures has been counted as "full", i.e. as if all of the grains were bulk-type, to estimate the volumetric density.

An estimate of density has been done by knowing weight and thickness of the film and values of 0.36 g/cm^3 at 100 Pa (corresponding to a porosity of about 85%), 0.92 g/cm^3 at 60 Pa and 1.66 g/cm^3 at 40 Pa were found (bulk silicon density being 2.33 g/cm^3), independently of the processing gas.

The so assessed synthesis of crystalline Si nanoparticles at room substrate temperature may find explanation if one considers that in PLD strong out-of-equilibrium conditions can be established during the plume expansion prior to deposition on the substrate. The laser ablation plume expansion, in fact, can be strongly spatially confined by the presence of a background gas [32], [44], [45] , with a travelling shock wave front, which slows down until it reaches the so-called stopping distance and is characterized by high pressure, temperature and density gradients at the shock front, if ablation occurs in a relatively high background pressure, resulting in strong out-of-equilibrium conditions [46]–[48]. This situation is favourable for cluster nucleation and we suppose that, if a threshold background deposition pressure is overcome, it can induce proper energetic conditions at the shock wave front leading to condensation of crystalline nanoparticles in the region of the traveling shock wave front, which can then diffuse in the background gas decreasing their kinetic energy. This process leads to low energy deposition thus producing a cluster-assembled material in which preformed Si QDs maintain, at least partially, their structure and properties.

Core-shell crystalline-amorphous nanoparticles and hollow nanospheres have been recently reported by Sturm and coworkers in the synthesis of Sm–Fe(Ta)–N structures by PLD in a 1 atm nitrogen pressure, together with a detailed and systematic analysis of the sequence of steps occurring during the ablation–deposition process and of the growth mechanisms of such nanostructures [49]. They involve the formation of nanocrystals and core-shell or void-shell structures from solidification of a multi-component system, with the main determining parameter for the formation of either core–shell or filled nanocrystals being the amount of dissolved gas in the initial molten droplet. The proposed explanation cannot be directly extended to our case, due to the different material structure and experimental conditions; however, we cannot exclude that a similar mechanism may occur involving solidification of silicon aggregates in the presence of dissolved gas atoms (argon).

Alternatively, we can infer that in our case the presence of strong temperature gradients may be responsible for the observed peculiar core-shell nanostructures. A possible formation mechanism may be related to a crystallization process starting at the surface of Si clusters formed in the ablation plume, followed, in particular conditions, by a rapid local thermal annealing leading to an amorphous core. Considering that molten silicon releases latent heat at solidification, the observed unique structure can be the effect of a “recalescence” process, that is, an increase in temperature that appears while cooling through a range of temperatures in which change in structure occurs, likely caused by local heat released at solidification and mainly governed by laser energy density. This amorphization process, already observed in the case of solidification of silicon thin films [50], [51] after melting by laser irradiation, has been supposed to be mainly initiated by laser energy density, when its value is just above the melting threshold, and it seems to be the most plausible process to be invoked in the formation of our core-shell nanostructures. As suggested in the work of Sameshima et al. [50], it can be interpreted as cooling of the molten silicon layers to an isothermal supercooled state and followed by fast solidification.

2.4 Conclusions

In summary, we have shown how we grow nanostructured silicon films with different porosities by Pulsed Laser Deposition (PLD) in argon or in a mixture of argon and few percents of hydrogen as buffer gas. Without any further post-deposition steps, samples deposited at relatively high pressure (100 Pa) embed Si NCs, as revealed by Raman investigation and confirmed by TEM analysis. For all the samples, with or without nanocrystals, the porosity of the film has been controlled by suitable deposition parameters and features a wide range of structures, from very compact to columnar algae-like shaped. In-situ oxidation of the film has been effectively reduced by the presence of few percentage of hydrogen gas in the pure argon gas. The fabrication of silicon NCs via PLD represents an excellent alternative to obtain these structures at room temperature without any further high-temperature steps and offers the possibility to tailor the properties of the crystals and of the amorphous matrix.

As for the possible applications for PLD-grown Si NCs, the proposed synthesis approach can be exploited in the near future to obtain Si NCs in different matrices (e.g. silicon oxide, carbide or nitride) and therefore realize a system of Si QDs embedded in a compact host matrix, possibly allowing for efficient charge transport through the QD network. Also the novel core-shell nanostructures here introduced can be beneficial to this purpose, since the Si crystalline shell could in principle work as a stable mechanical support and efficient electrical conducting pathway, while the amorphous core should lead to an improvement of the material optical characteristics (low-grade amorphous silicon with long range disorder in its atomic structure behaves like a direct-bandgap semiconductor with two-orders higher optical absorption coefficient as compared with its crystalline counterpart).

Up to now, the partially oxidized amorphous silicon matrix is not believed to provide sufficient electrical conductivity to be suitable for straightforward integration in a solar cell device, but the proposed approach can nevertheless be developed more extensively to address this target, e.g. by further reducing oxidation, and/or doping the matrix.

Nanocrystals apart, the approach here described opens the way to meaningful application in different fields of the energy production and storage. By suitably adjusting the process parameters, it is possible to engineer the nanostructured silicon films so that they have suitable properties for the target application. In particular, the following chapter will show how silicon films grown by PLD have been successfully optimized to be used as anodes in lithium-ion batteries. In addition, a preliminary work addressing the field of thermoelectric materials will be presented in Chapter 5.

2.5 Methods

In order to characterize morphology and thickness of the samples, images were taken both in cross section and top-view by a Supra 40 Zeiss Scanning Electron Microscope (SEM, accelerating voltage 2-4 kV).

With the same instrument, Energy-Dispersive X-ray Spectra (EDS) investigation was performed using an accelerating voltage of 5 kV, to excite Kα electronic levels of O and Si, the signal being collected by a Si(Li) detector. We used Kα of Silicon (1.74 keV) for system calibration and every EDS analysis (250000 counts) was repeated three times on different equivalent areas of the sample. We investigated the samples prepared at 100 Pa, in order to assess the degree of oxidation and to test the effect of using the mixture of Ar and H_2 (<3 vol. %), instead of pure Ar, as deposition gas.

Amorphous/crystalline structure of the films was characterized by confocal Raman spectroscopy. Raman spectra were acquired upon excitation by a He-Cd laser (325 nm), or the second harmonic (532 nm) of an air-cooled Nd:YAG laser. The laser power for the 532 nm beam was lowered down to 0.3 mW (sample surface), in order to avoid laser-induced sample annealing. Spectra were typically recorded in the range 200-2000 cm^{-1} in the Stokes region and were calibrated against the 520.5 cm^{-1} line of an internal silicon wafer reference. The signal to noise ratio was enhanced by repeated acquisitions.

Selected samples were analysed by Transmission Electron Microscopy (TEM) in order to reveal the presence, spatial dispersion and dimension of nanocrystals, as well as the structure of the film. For the TEM investigation the samples were prepared by scratching the film by means of a diamond tip, dispersing the fragments in few mL toluene and dripping the suspension on a commercial copper grid covered with a few nm thick carbon film on top of a carbon net.

Diffraction-contrast TEM imaging and electron diffraction analysis were carried out with a Jeol JEM 1011 instrument, equipped with a thermionic tungsten source, operated at 100 kV. High-Resolution TEM (HR-TEM), Energy-Filtered TEM (EFTEM) and Scanning TEM-High Angle Annular Dark Field (STEM-HAADF) analyses were performed with a Jeol JEM 2200FS instrument, equipped with a Schottky FEG W source, operated at 200 kV, and with a CEOS image aberration corrector and an in-column energy filter.

References

[1] E. Biserni, A. Scarpellini, R. Brescia, D. Dellasega, A. Li Bassi, and P. Bruno, “Room temperature fabrication of silicon nanocrystals by pulsed laser deposition,” *J. Nanoparticle Res.*, vol. 16, no. 6, p. 2461, May 2014.

[2] M. N. R. Ashfold, F. Claeyssens, G. M. Fuge, and S. J. Henley, “Pulsed laser ablation and deposition of thin films.,” *Chem. Soc. Rev.*, vol. 33, no. 1, pp. 23–31, Jan. 2004.

[3] H. Krebs, M. Weisheit, J. Faupel, E. Sueske, T. Scharf, C. Fuhse, M. Stoermer, K. Sturm, M. Seibt, H. Kijewski, D. Nelke, E. Panchenko, and M. Buback, “Pulsed Laser Deposition (PLD) - a Versatile Thin Film Technique,” in *Advances in Solid State Physics*, vol. 43, B. Kramer, Ed. Berlin, Heidelberg: Springer Berlin Heidelberg, 2003, pp. 505–518.

[4] D. H. Lowndes, C. M. Rouleau, T. G. Thundat, G. Duscher, E. A. Kenik, and S. J. Pennycook, “Silicon and zinc telluride nanoparticles synthesized by low energy density pulsed laser ablation into ambient gases,” *J. Mater. Res.*, vol. 14, no. 02, pp. 359–370, Feb. 1999.

[5] G. Conibeer, “Applications of Si Nanocrystals in Photovoltaic Solar Cells,” in *Silicon Nanocrystals*, L. Pavesi and R. Turan, Eds. Weinheim, Germany: Wiley-VCH Verlag GmbH & Co. KGaA, 2010, pp. 555–582.

[6] R. Muralidhar, M. A. Sadd, and J. B. E. White, “Silicon Nanocrystal Nonvolatile Memories,” in *Device Applications of Silicon Nanocrystals and Nanostructures*, N. Koshida, Ed. Boston, MA: Springer US, 2009, pp. 223–249.

[7] E. Borsella, M. Falconieri, N. AHerlin, V. Loschenov, Y. Nie, I. Rivolta, A. Ryabova, and D. Wang, “Biomedical and Sensor Applications of Silicon Nanoparticles,” in *Silicon Nanocrystals*, L. Pavesi and R. Turan, Eds. Weinheim, Germany: Wiley-VCH Verlag GmbH & Co. KGaA, 2010, pp. 507–536.

[8] H. Kim, M. Seo, M. Park, and J. Cho, “A Critical Size of Silicon Nano-Anodes for Lithium Rechargeable Batteries,” *Angew. Chemie Int. Ed.*, vol. 49, no. 12, pp. 2146–2149, 2010.

[9] T. Suzuki, Y. Ohishi, K. Kurosaki, H. Muta, and S. Yamanaka, “Thermal Conductivity of Size-Controlled Bulk Silicon Nanocrystals Using Self-Limiting Oxidation and HF Etching,” *Appl. Phys. Express*, vol. 5, no. 8, p. 081302, Jul. 2012.

[10] L. Tsakalakos, “Nanostructures for photovoltaics,” *Mater. Sci. Eng. R Reports*, vol. 62, no. 6, pp. 175–189, Nov. 2008.

[11] G. Conibeer, R. Patterson, L. Huang, J.-F. Guillemoles, D. Kőnig, S. Shrestha, and M. A. Green, “Modelling of hot carrier solar cell absorbers,” *Sol. Energy Mater. Sol. Cells*, vol. 94, no. 9, pp. 1516–1521, 2010.

[12] D. König, K. Casalenuovo, Y. Takeda, G. Conibeer, J. F. Guillemoles, R. Patterson, L. M. Huang, and M. a. Green, “Hot carrier solar cells: Principles, materials and design,” *Phys. E Low-dimensional Syst. Nanostructures*, vol. 42, no. 10, pp. 2862–2866, Sep. 2010.

[13] A. Nozik, “Quantum dot solar cells,” *Phys. E Low-dimensional Syst. Nanostructures*, vol. 14, no. 1–2, pp. 115–120, Apr. 2002.

[14] A. Luque, A. Martí, and A. J. Nozik, “Solar Cells Based on Quantum Dots : Multiple Exciton Generation and Intermediate Bands,” *MRS Bull.*, vol. 32, no. MARCH, pp. 236–241, 2007.

[15] A. M. Hartel, D. Hiller, S. Gutsch, P. Löper, S. Estradé, F. Peiró, B. Garrido, and M. Zacharias, “Formation of size-controlled silicon nanocrystals in plasma enhanced chemical vapor deposition grown SiOxNy/SiO2 superlattices,” *Thin Solid Films*, vol. 520, no. 1, pp. 121–125, Oct. 2011.

[16] S. Park, E. Cho, G. Conibeer, and M. a. Green, “Study of silicon quantum dot p-n or p-i-n junction devices on c-Si substrate,” *2008 Conf. Optoelectron. Microelectron. Mater. Devices*, pp. 316–319, Jul. 2008.

[17] G. Conibeer, M. Green, R. Corkish, Y. Cho, E.-C. Cho, C.-W. Jiang, T. Fangsuwannarak, E. Pink, Y. Huang, T. Puzzer, T. Trupke, B. Richards, A. Shalav, and K. Lin, “Silicon nanostructures for third generation photovoltaic solar cells,” *Thin Solid Films*, vol. 511–512, pp. 654–662, Jul. 2006.

[18] X. Cheng, R. Gondosiswanto, S. Ciampi, P. J. Reece, and J. J. Gooding, “One-pot synthesis of colloidal silicon quantum dots and surface functionalization via thiol-ene click chemistry.,” *Chem. Commun. (Camb).*, vol. 48, no. 97, pp. 11874–6, Dec. 2012.

[19] L. Mangolini and U. Kortshagen, “Plasma-Assisted Synthesis of Silicon Nanocrystal Inks,” *Adv. Mater.*, vol. 19, no. 18, pp. 2513–2519, Sep. 2007.

[20] L. Mangolini, E. Thimsen, and U. Kortshagen, “High-yield plasma synthesis of luminescent silicon nanocrystals.,” *Nano Lett.*, vol. 5, no. 4, pp. 655–9, Apr. 2005.

[21] I. Umezu, A. Sugimura, M. Inada, T. Makino, K. Matsumoto, and M. Takata, “Formation of nanoscale fine-structured silicon by pulsed laser ablation in hydrogen background gas,” *Phys. Rev. B*, vol. 76, no. 4, p. 045328, Jul. 2007.

[22] I. Umezu, Y. Nakayama, and A. Sugimura, “Formation of core-shell structured silicon nanoparticles during pulsed laser ablation,” *J. Appl. Phys.*, vol. 107, no. 9, p. 094318, May 2010.

[23] Q. Cheng, E. Tam, S. Xu, and K. K. Ostrikov, “Si quantum dots embedded in an amorphous SiC matrix: nanophase control by non-equilibrium plasma hydrogenation.,” *Nanoscale*, vol. 2, no. 4, pp. 594–600, Apr. 2010.

[24] W. Marine, L. Patrone, B. Luk’yanchuk, and M. Sentis, “Strategy of nanocluster and nanostructure synthesis by conventional pulsed laser ablation,” *Appl. Surf. Sci.*, vol. 154–155, pp. 345–352, Feb. 2000.

[25] C. L. Yuan, “Room-Temperature Coercivity of Ni/NiO Core/Shell Nanoparticles Fabricated by Pulsed Laser Deposition,” *J. Phys. Chem. C*, vol. 114, no. 5, pp. 2124–2126, Feb. 2010.

[26] Y.-C. Wu, L.-W. Wang, and C.-H. Lai, “(001) FePt nanoparticles with ultrahigh density of 10 T dots/in.[sup 2] on amorphous SiO[sub 2] substrates,” *Appl. Phys. Lett.*, vol. 93, no. 24, p. 242501, 2008.

[27] R. F. Wood, J. N. Leboeuf, K. R. Chen, D. B. Geohegan, and a. a. Puretzky, “Dynamics of plume propagation, splitting, and nanoparticle formation during pulsed-laser ablation,” *Appl. Surf. Sci.*, vol. 127–129, pp. 151–158, May 1998.

[28] G. Conibeer, N. Ekins-Daukes, J.-F. Guillemoles, D. Kőnig, E.-C. Cho, C.-W. Jiang, S. Shrestha, and M. Green, “Progress on hot carrier cells,” *Sol. Energy Mater. Sol. Cells*, vol. 93, no. 6–7, pp. 713–719, Jun. 2009.

[29] D. Dellasega, G. Merlo, C. Conti, C. E. Bottani, and M. Passoni, “Nanostructured and amorphous-like tungsten films grown by pulsed laser deposition,” *J. Appl. Phys.*, vol. 112, no. 8, p. 084328, 2012.

[30] M. Fusi, V. Russo, C. S. Casari, A. Li Bassi, and C. E. Bottani, “Titanium oxide nanostructured films by reactive pulsed laser deposition,” *Appl. Surf. Sci.*, vol. 255, no. 10, pp. 5334–5337, Mar. 2009.

[31] C. S. Casari and A. Li Bassi, “Pulsed Laser Deposition of Nanostructured Oxides : from Clusters to Functional Films,” in *Advances in Laser and Optics Research*, vol. 7, W. T. Arkin, Ed. Nova Science Publishers, Inc., 2012, pp. 65–100.

[32] V. I. Merkulov, D. H. Lowndes, and G. E. Jellison, “Synthesis and Characterization of Pulsed-Laser Deposited Amorphous Carbon Films,” in *Pulsed Laser Deposition of Thin Films*, D. B. Chrisey and G. Hubler, Eds. Wiley & Sons: New York, NY, 1994, p. 115.

[33] P. Bruno, T. Salve, V. Russo, D. Dellasega, G. Filoni, C. S. Casari, C. E. Bottani, and A. L. Bassi, “Pulsed Laser Deposition of Silicon Nanostructures,” *MRS Proc.*, vol. 1322, pp. mrss11–1322–b05–34, Sep. 2011.

[34] F. Di Fonzo, C. S. Casari, V. Russo, M. F. Brunella, a Li Bassi, and C. E. Bottani, “Hierarchically organized nanostructured TiO2 for photocatalysis applications.,” *Nanotechnology*, vol. 20, no. 1, p. 015604, Jan. 2009.

[35] S. Honda, T. Mates, M. Ledinsky, J. Oswald, a. Fejfar, J. Kočka, T. Yamazaki, Y. Uraoka, and T. Fuyuki, “Effect of hydrogen passivation on polycrystalline silicon thin films,” *Thin Solid Films*, vol. 487, no. 1–2, pp. 152–156, Sep. 2005.

[36] J. I. Pankove, R. O. Wance, and J. E. Berkeyheiser, “Neutralization of acceptors in silicon by atomic hydrogen,” *Appl. Phys. Lett.*, vol. 45, no. 10, p. 1100, Nov. 1984.

[37] N. F. Mott, E. A. Davis, and R. A. Street, “States in the gap and recombination in amorphous semiconductors,” *Philos. Mag.*, vol. 32, no. 5, pp. 961–996, Nov. 1975.

[38] W. Fuhs, L. Korte, and M. Schmidt, “Heterojunctions of hydrogenated amorphous silicon and monocrystalline silicon,” *J. Optoelectron. …*, vol. 8, no. 6, pp. 1989–1995, 2006.

[39] Z. Li, W. Li, Y. Jiang, H. Cai, Y. Gong, and J. He, “Raman characterization of the structural evolution in amorphous and partially nanocrystalline hydrogenated silicon thin films prepared by PECVD,” *J. Raman Spectrosc.*, vol. 42, no. 3, pp. 415–421, Mar. 2011.

[40] H. Richter, Z. P. Wang, and L. Ley, “The one phonon Raman spectrum in microcrystalline silicon,” *Solid State Commun.*, vol. 39, no. 5, pp. 625–629, Aug. 1981.

[41] Y. Duan, J. F. Kong, and W. Z. Shen, “Raman investigation of silicon nanocrystals: quantum confinement and laser-induced thermal effects,” *J. Raman Spectrosc.*, vol. 43, no. 6, pp. 756–760, Jun. 2012.

[42] G. Faraci, S. Gibilisco, P. Russo, A. Pennisi, and S. La Rosa, “Modified Raman confinement model for Si nanocrystals,” *Phys. Rev. B*, vol. 73, no. 3, pp. 1–4, Jan. 2006.

[43] Y. He, C. Yin, G. Cheng, L. Wang, X. Liu, and G. Y. Hu, “The structure and properties of nanosize crystalline silicon films,” *J. Appl. Phys.*, vol. 75, no. 2, p. 797, 1994.

[44] D. B. Geohegan, A. a. Puretzky, G. Duscher, and S. J. Pennycook, “Time-resolved imaging of gas phase nanoparticle synthesis by laser ablation,” *Appl. Phys. Lett.*, vol. 72, no. 23, p. 2987, 1998.

[45] S. Amoruso, A. Sambri, M. Vitiello, and X. Wang, “Propagation of LaMnO3 laser ablation plume in oxygen gas,” *Appl. Surf. Sci.*, vol. 252, no. 13, pp. 4712–4716, Apr. 2006.

[46] N. Arnold, J. Gruber, and J. Heitz, “Spherical expansion of the vapor plume into ambient gas : an analytical model,” vol. 93, pp. 87–93, 1999.

[47] J. N. Leboeuf, J. M. Donato, D. B. Geohegan, C. L. Liu, A. A. Puretzky, and R. F. Wood, “Modeling of dynamical processes in laser ablation,” 2009.

[48] D. H. Lowndes, D. B. Geohegan, A. A. Puretzky, and D. P. Norton, “Synthesis of Novel Thin-Film Materials by Pulsed Laser Deposition,” *Science (80-.).*, vol. 273, no. 5277, pp. 898–903, 1996.

[49] S. Sturm, K. Z. Rožman, B. Markoli, E. Sarantopoulou, Z. Kollia, a C. Cefalas, and S. Kobe, “Formation of core-shell and hollow nanospheres through the nanoscale melt-solidification effect in the Sm-Fe(Ta)-N system.,” *Nanotechnology*, vol. 21, no. 48, p. 485603, Dec. 2010.

[50] T. Sameshima and S. Usui, “Mechanism of pulsed laser-induced amorphization of silicon films,” *Appl. Phys. Lett.*, vol. 59, no. 21, p. 2724, 1991.

[51] T. Sameshima and S. Usui, “Pulsed laser-induced amorphization of silicon films,” *J. Appl. Phys.*, vol. 70, no. 3, p. 1281, 1991.

Chapter 3
Nanostructured Silicon as Anode for Lithium-ion Batteries

The Si nanostructures described in Chapter 2 showed characteristics and properties suitable for interesting exploitation in the field of Lithium Ion Batteries (LIB). However, Silicon anodes for LIB have to cope with the issues discussed in Chapter 1. The work here presented aims at studying and tailoring Silicon-based films produced by Pulsed Laser Deposition to overcome these difficulties.

Such porous structures offer a large surface area to volume ratio, which can accommodate the large volume expansion associated with silicon lithiation. Then, in order to promote the formation of a stable SEI layer and improve conductivity and mechanical stability, Carbon has been coupled to Si, either as a separate capping layer or as integrated in the Si film. Four different anode architectures are presented in the following, which have been tested in collaboration with external groups (reported in each section).

The author has fabricated the tailored films under analysis (with the exception of CVD layer), characterized their morphology by scanning electron microscopy techniques and performed Raman investigation. A network of national and international collaborations has been set to perform TEM and HRSEM[1] *analysis, build up electrochemical cells and perform electrochemical tests. The electrochemical results have been discussed then by the author to correlate them to morphological and structural investigations.*

---

[1] TEM stands for Transmission Electron Microscopy, while HRSEM stands for High-Resolution Scanning Electron Microscopy

3.1 Anodes made of Si(PLD) + C(CVD)

*In collaboration with **University of Boulder**, Colorado (US); **IIT-Genova** and **Politecnico di Milano**, Dept. of Chemistry, Material and Chemical Engineering CMIC.*

The work here described is reported in a scientific publication ([1]*)*

SUMMARY. In this work, we address the two main drawbacks of silicon anodes in lithium ion microbatteries by a two-layer architecture obtained by means of a two-step method. We fabricate novel nanocomposite Si-C anodes by depositing nanostructured porous amorphous Si films by Pulsed Laser Deposition (PLD) at room temperature, followed by Chemical Vapour Deposition (CVD) of a thin carbon coating. The mesoporosity of the nanostructured Si films and its lack of crystallinity are expected to reduce the detrimental effects of volume variations and to avoid mechanical stressing due to amorphization in the first cycles. The thin CVD-grown carbon layer, then, is expected to promote the formation of a stable solid electrolyte interphase (SEI) layer and protect Si from direct contact with the electrolyte. We propose then a structure where the formation of SEI is shifted away from the active silicon; this simple architecture allows for a straightforward two-step process that presents so far no upper limits to the obtainable film thickness. The nanometric porosity allowing for volume expansion and the crucial role of C in the formation of a solid SEI have led to satisfactory values of capacity and capacity retention (i.e. no decay for at least 1000 cycles). Moreover, we proved the possibility of increasing the overall capacity of this anode architecture by thickening the Si+C film without any negative impact on its mechanical stability (at least up to 5µm).

Film fabrication (in collaboration with Dept. of Chemistry, Material and Chemical Engineering CMIC, Politecnico di Milano for the Chemical Vapour Deposition process)

As described in Chapter 2, the approach for growing films with desired morphology was to adjust the background gas pressure (Ar: H_2) during pulsed laser deposition, so that cluster nucleation and growth could be to some extent controlled and hence the film porosity. For this study on LIB, two target morphologies were chosen from those with columnar mesostructure already explored and described in Chapter 2. The two were grown, respectively, at lower (60Pa) and higher (100Pa) pressure to roughly assess the impact of porosity on the final anode performance (see figure 3.1 for SEM picture of as-deposited films).

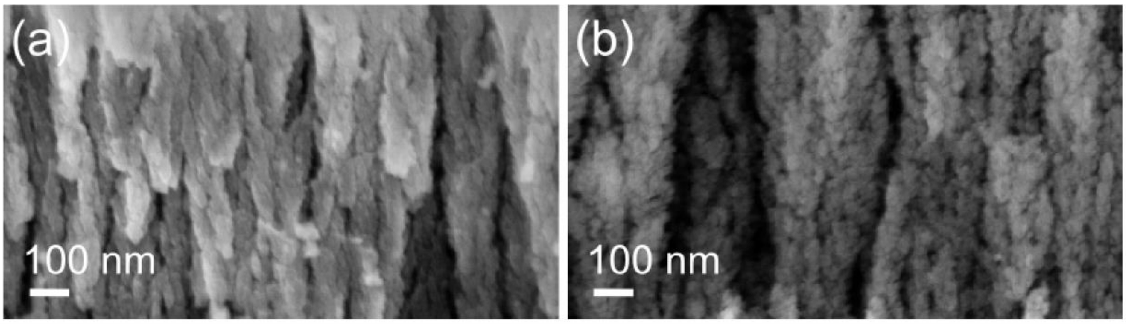

Figure 3.1. SEM micrographs of as-deposited Si films (before C deposition), grown at (a) 60Pa and (b) 100Pa Ar:H_2

Copper discs (1.3 cm diameter) were used as substrates. The increase of processing gas pressure during the PLD process leads to an increase in the film porosity, with an estimated density of 0.92 g cm^{-3} for [Si60] and 0.36 g cm^{-3} for [Si100][2].

Some of the Si films were then subjected to covering by a carbon layer grown by CVD. We use the notation [Si(xx)] or [Si(xx)+C(CVD)] to designate samples where Si is deposited by PLD at 'xx' pressure, without or with C coating by CVD, respectively.

Nominal thickness of Si films was set to 1 µm; in addition, for one chosen set of parameters, a thicker anode (2.5 µm) was also prepared with PLD silicon and CVD carbon layer, in order to prove the feasibility of increasing the anode capacity by increasing its thickness without any negative effects on the mechanical stability.

For CVD, the samples were loaded into a quartz tubular furnace where a mixture of H_2 and N_2 gas (6 sccm and 100 sccm, respectively) was fluxed while ramping the temperature up to 825°C at the rate of 10°C/min. After stabilization of the temperature (15 min), ethylene was added (20 sccm) during 5 min (or 7 minutes in the case of thicker sample) to the gas mixture, as a precursor for carbon deposition. After this time, the previous gas atmosphere of H_2 and N_2 was restored during the whole cooling down step. In addition to substrates previously covered by the Si film, some bare Cu substrates were also loaded into the furnace for the same coating process in the same conditions, so to get pure C(CVD) anodes to be used in reference cells.

Process temperature for the CVD was chosen to be right above the threshold for the ethylene decomposition but low enough to avoid any possible effect of recrystallization of the amorphous Si layer underneath. As for the reaction time, it was adjusted so to result in the formation of a continuous thin layer on top of the Si film as later shown in SEM pictures.

Raman analysis

Raman spectra were acquired on the samples before and after C deposition, upon excitation by the second harmonic (532nm) of an air-cooled Nd:YAG laser. Laser power was kept below 0.4 mW (sample surface) while sampling Si films, in order to avoid laser-induced annealing effects. Spectra were recorded in the range 100-1800cm-1 in the Stokes region and were calibrated against the 520.5cm-1 line of an internal silicon wafer reference. The signal-to-noise ratio was enhanced by repeated acquisitions.

The investigation is here discussed upon considering the spectral range as divided into two parts, each containing the features arising either from as-deposited Si film (100-600cm-1) or C layer (1000-1800cm-1).

In the range 100-600cm-1, Raman spectra recorded on all of the Si films as-deposited by PLD, without C coating, show the features of amorphous Si, i.e. the bands centred around 140, 320, 440 and 490 cm-1, related to the transverse acoustic (TA), longitudinal acoustic (LA), longitudinal optic (LO) and transverse optic (TO) modes [1], respectively (figure 3.2 (a)).

In samples produced at 100 Pa, an additional peak at 515 cm^{-1} is detected, which is attributed to the transverse optic (TO) mode of silicon crystals of nanometric size, in agreement with the literature [3], [4] and with the capability, described in Chapter 2, to grow Si nanocrystals by PLD (2.5 to 6 nm), embedded in an amorphous matrix.

Considering the spectral region between 1000 and 1800cm-1, spectra of C(CVD) covered samples were fitted with four Gaussian curves, following the procedure described by Ferrari et al. [5]. No signal from the underlying Si is observed in these samples.

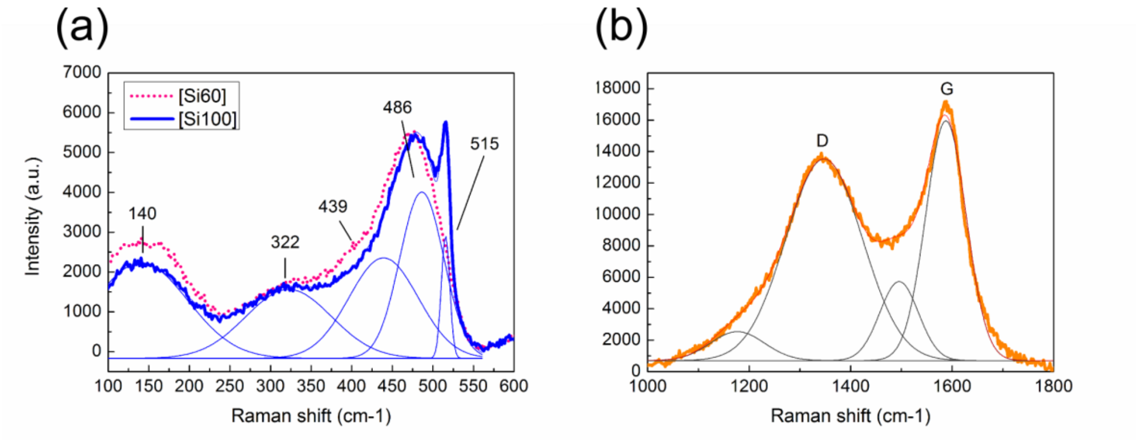

Figure 3.2. (a) Raman spectra of [Si60](dotted red) and [Si100](straight blue) deposited by PLD (laser power: 0.3mW). The four characteristic bands of amorphous Silicon are evidenced by gaussian fitting the two curves (only [Si100] shown). An additional peak at 515cm-1 features [Si100] spectrum and it is ascribed to the presence of Si nanocrystals within the amorphous film. (b) Raman spectrum (laser power: 3.7 mW) of C(CVD), fitted with four gaussian bands, following the method proposed by Ferrari et al.47. D and G bands are centered at 1348cm-1 and 1588cm-1, respectively.

The spectrum in figure 3.2(b) features the two typical bands of amorphous graphitic carbon, the one intense and broad around 1350cm-1 (D band) and the narrower one around 1581cm-1 (G band), this latter being associated to the in-plane stretching of *sp2* bonds. D band, instead, arises from the breathing mode of C-rings in disordered layers, e.g. from distorted 6-folded rings or from rings of different order [5], [6]. By evaluating the relative intensity I(D)/I(G) of the D peak to G peak, one can extract information on the degree of disorder in the film, as explained in[5]. In particular, in disordered graphite and amorphous carbon I(D)/I(G) is proposed to be proportional to the square of the graphitic cluster dimension L_a^2 and it decreases then with increasing disorder, i.e. reduced L_a[5].

In our samples, I(D)/I(G) ratio gives ~0.84, which corresponds, according to Ferrari's model, to disordered graphitic carbon with an approximate cluster dimension of 12.4 Å.

Cell assembling and electrochemical testing (in collaboration with University of Boulder, CO (US))

Electrochemical measurements were carried out using an Arbin 2000 battery test station. All cells were assembled in an Ar-filled glove-box using the porous nanostructured Si and Si-C thin films as the working electrodes and lithium metal foil as the counter-electrode. The electrolyte was 1 M $LiPF_6$ dissolved in a 1:1 (volume ratio) mixture of ethylene carbonate (EC) and diethyl carbonate

(DEC); the separator was a glass micro-fibre disc (Whatman GF/F), and the shell was a stainless steel CR2032 coin cell (VWR Inter.).

Electron Microscopy (HRSEM, TEM) and Energy-Dispersive X-ray Spectroscopy (EDS) (in collaboration with IIT-Genova)

Thickness and morphology of the Si films were investigated by the author by a Supra 40 Zeiss Scanning Electron Microscope (SEM, accelerating voltage 2-4kV), before C deposition, for samples fabricated for this purpose on Si substrates previously coated by a 100nm thick Al layer.

In order to evaluate the film morphology and composition after C deposition, before and after electrochemical testing, High Resolution Scanning Electron Microscopy (HRSEM) investigations were performed on [Si60+C(CVD)] with a JEOL JSM-7500F instrument, equipped with a cold field emission gun source operating at 10 or 15 kV. Energy-Dispersive X-ray Spectroscopy (EDS) compositional analysis was carried out using an Oxford Instrument silicon drift detector (SDD) X-Max80 (80 mm^2 effective area of detecting device) mounted on the HRSEM instrument.

TEM analysis was performed on the same samples, which were scratched from the substrate by means of a diamond tip and dropped onto a commercial holey carbon-coated Cu grid. In case of the sample subjected to electrochemical testing, the preparation was carried out in a N_2-filled glove box, so as to limit the air exposure time to only few minutes before insertion into the TEM. The analyses were carried out with a JEOL JEM 2200FS instrument, operated at 200kV, equipped with a Scanning TEM (STEM) unit. EDS compositional and spectral maps were recorded simultaneously with the acquisition of High Angle Annular Dark Field (HAADF-STEM) images, using a Bruker Quantax 400 system with a 60 mm2 XFlash 6T SDD.

Results and Discussion

The electrochemical behaviour of the anodes was then studied in half-coin cell configuration with Li metal as counter electrode between 5mV and 1.5V or 50mV and 1.5V, under constant-current conditions. At the end of each delithiation, we applied a constant-voltage for 10 minutes.

The charge/discharge curves of the first three cycles, measured between 5mV and 1.5V versus Li/Li+ at a current density of 54μA cm^{-2}, are shown in figure 3.3(a,b) for samples [Si100] (pure silicon) and [Si60+C(CVD)].

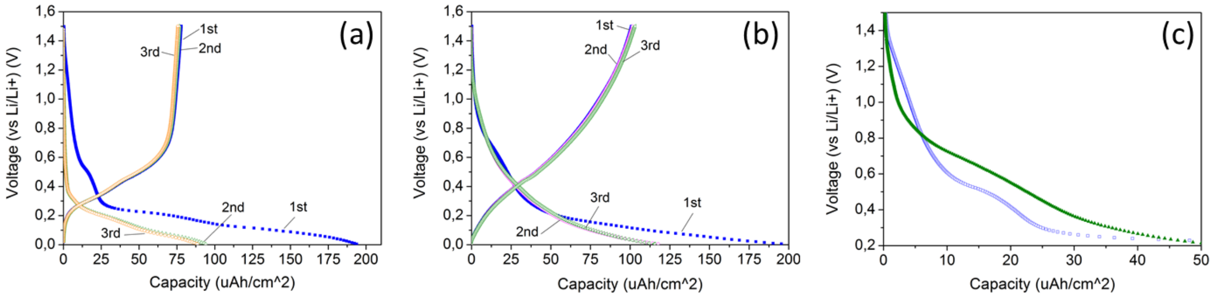

Figure 3.3. First three cycles charge/discharge curves of samples (a) [Si100] and (b) [Si60(PLD)+C(CVD)]. In (a), the plateaus of amorphous silicon lithiation (discharge) and delithiation (charge) are clearly visible. In (b), the small plateau around 0.7V in lithiation is attributed to the SEI formation at the C-electrolyte interface; 2nd delithiation curve completely overlaps to 1st delithiation curve. c) Zoomed first lithiation curves of [Si100] and [Si60(PLD)+C(CVD)] in the voltage range of SEI formation (1.0V-0.4V). The difference in shape and slope of the two curves highlights a different mechanism of SEI formation in the two samples.

The first lithiation curve in Si[100] (figure 3.3(a)) shows a rapid drop of the potential with two plateaus: the first one, around 0.5V, can be related to the SEI formation, that concurs to irreversible capacity losses; the second one, around 0.3V is attributed to lithiation of amorphous silicon. In delithiation curves, the two steps around 0.3 and 0.5V are attributed to low and high voltage delithiation of amorphous silicon[7]. The first discharge capacity is about 195µAh cm^{-2} with an initial coulombic efficiency of 42% (see Table 3.1).

COULOMBIC EFFICIENCY (%)

cycle	[Si100]	[Si60+C]
1st	42,1	55,3
2nd	84,0	92,1
3rd	87,9	95,1

IRREVERSIBLE CAPACITY LOSS (%)

cycle	[Si100]	[Si60+C]
after 2cycle	50,9	39,8
after 3cycle	54,1	40,9

Table 3.1. Coulombic efficiency and irreversible capacity loss (discharge) of samples [Si100] and [Si60+C] for the first 3 cycles, showing noticeable improvement in the samples topped by C.

In the lithiation curve of [Si60+C(CVD)], (figure 3.3(b)), the small plateau around 0.7 V is related to the formation of the SEI layer on the carbonaceous electrode surface [8], while the change in slope around 0.3V is associated to the lithiation of amorphous silicon, as in the previous case. Below 0.2V also lithiation of carbon plays a role[9]. From the 2nd cycle on, no plateau is observed during lithiation, which is the typical voltage profile of Li insertion/extraction in amorphous structure materials without phase transformation. These observations are consistent with other works [10], [11]. In delithiation profiles, the smooth change in slope around 0.5V can be ascribed to delithiation of a-Li$_x$Si to a-Si, as in the previous case. The first discharge capacity is about 195μAh cm^{-2} with an initial coulombic efficiency of 55%, this value showing improvement as against pure Si sample (see Table 3.1). The charge and discharge capacities in the subsequent cycles at the same rate are highly reversible with a discharge capacity about 115μAh cm^{-2}. Similar curves feature all the analysed C-coated Si samples (not shown).

For more clarity, data of coulombic efficiency and capacity fade (first 3 cycles) of the two samples are reported in Table 3.1.

In figure 3.3(c), 1st lithiation curves of [Si100] and [Si60+C(CVD)] have been zoomed in the potential range from 1.4V to 0.3V, typical of SEI layer formation. The strong discrepancy in slope and shape of the two curves evidences that the mechanisms driving SEI formation in the first half-cycle are different, according to the material facing interaction with the electrolyte, either Si or C. The capability of C(CVD) of forming a stable SEI layer can be observed in the good overlap between 2nd and 3rd lithiation curves in figure 3.3(b), unlike the case of [Si100].

All this proves how the beneficial role of C layer be crucial for the formation of a stable and protective SEI layer, hence for a sensitive reduction of irreversible capacity losses.

In figure 3.4 cyclic charge/discharge curves of the anodes under analysis are presented under different testing conditions together with coulombic efficiency. Cycling was performed under constant-current density with step-increasing values every 15 cycles, so to test the rate capability. The voltage range was either limited to a cut-off voltage of 50mV or extended to 5mV.

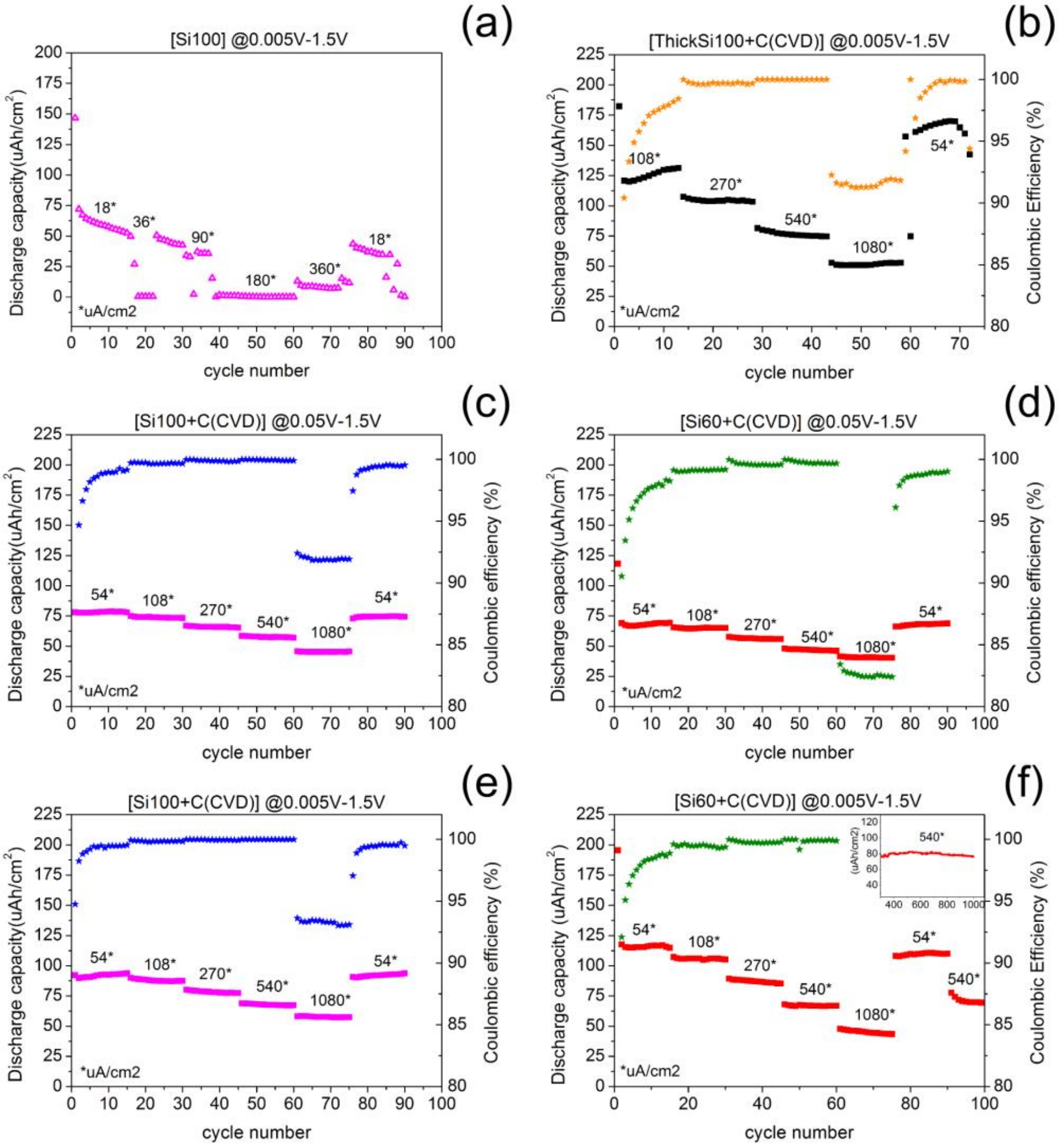

Figure 3.4. Curves of discharge capacity (squares) and coulombic efficiency (star) of (a) [Si100] @5mV; (b) [thick Si100+C(CVD)] @5mV; (c) [Si100+C(CVD)] @50mV; (d) [Si60+C(CVD)] @50mV; (e) [Si100+C(CVD) @5mV]; (f) [Si60+C(CVD) @5mV]. Integer numbers within the graphs correspond to the constant current density applied, in µAcm-2. Inset in (f) shows long cycle life of [Si60+C(CVD)] up to 1000 cycles with no capacity decay.

Figure 3.4(c) and (e) refer to sample [Si100+C(CVD)] under different voltage range, while figure 3.4(d) and (f) refer to [Si60+C(CVD)]. Figure 3.4(a) shows the reference data of [Si100] without C layer, while data in figure 3.4(b) are recorded on the [ThickSi100+C(CVD)] sample.

As from figure 3.4(a), the poorer performances of [Si100] are improved in terms of stability by the addition of C coating by CVD. The C layer dramatically enhances the capacity retention upon cycling, as evidenced by comparing the graphs in figure 3.4(a) and (c). The behaviour of an anode made of pure C(CVD) film, deposited under the same conditions of C(CVD) coatings, was also tested as reference (not shown) and gave capacity always below 10μAh cm^{-2} for current densities in the same range.

In comparing the two kinds of anode with different Si morphology and CVD-deposited C, no significant difference is detected in their electrochemical behaviour (figure 3.4(c)-(d) or (e)-(f)).

When the cut-off voltage is limited to 50mV, the carbon coated Si film shows exceptional stability at different current densities for both morphologies, grown at either 60 or 100Pa. Its capacity at 1080μA cm^{-2} still preserves ~67% of that at 54μA cm^{-2}, indicating excellent rate capability. Even for cutoff voltage of 5mV, carbon coated silicon still possesses excellent stability in capacity retention and mechanical integrity, as shown in figure 3.4(f), where a capacity of ~75μAh cm^{-2} is maintained at 540μA cm^{-2} for 1000 cycles.

The low cutoff voltage of 5mV is in fact compatible with the formation of the crystalline lithiated phase c-$Li_{15}Si_4$, which takes place around 50mV and gives the highest theoretical capacity but also the highest volume expansion (3579mAh g^{-1} and 280%, respectively [12]). More in detail, during discharge, as recently described by Ogata et al. [13], Si alloys with Li into the amorphous phases a-Li_xSi with x increasing with decreasing voltage, up to the value of 3.75 at ~50mV. Across this potential threshold, the crystalline c-$Li_{3.75}Si$ phase can start to form out of the amorphous counterpart, with a kinetics of nucleation and growth that depends on the discharge rate[14]. In general, below 50mV c-$Li_{3.75}Si$ and a-$Li_{3.75}Si$ coexist, as well as underlithiated amorphous phases a-Li_xSi (x=2-3.75). Phase change, volume expansion and mismatch between different phases can induce severe mechanical stress upon cycling. Hatchard and Dahn, though, observed that the formation of c-$Li_{3.75}Si$ is suppressed in solid films thinner than ∼2.5μm[14] and Graetz et al.[15] suggested that crack propagation cannot occur if Si particles are 300nm or less in size. We think this is our case. If each of the Si clusters composing our mesostructure is considered a particle, its diameter is by far smaller than this critical size and we believe no crystalline lithiated phase is then formed, as confirmed by having no degradation at low cutoff voltages, and possibly no cracks propagate in our films.

Because of this reason, these mesoporous silicon-based films made of clusters, can be in principle grown up to films with thickness that overcomes the Hatchard and Dahn's threshold without inducing the formation of c-$Li_{3.75}Si$ phase. The anode capacity can be directly increased by increasing its thickness, without inducing any mechanical side-effect due to possible collapse of the porous nanostructure, as proven in figure 3.4(b) from good stability upon cycling. The highest discharge capacity of ~175µAh cm^{-2} can be reached at a current density of 54µA cm^{-2}.

These samples show in general excellent coulombic efficiency (>99%) when reaching stability, indicating that conformal carbon coating on top helps to reduce the contact between electrolyte and high-surface silicon, therefore leading to a reduced SEI formation, i.e. reduced energy losses in side reactions. The initial efficiency is usually around 85% (average on first 5 cycles) and it does stabilize up to its higher value only after some cycles, due to the surface area of the nanostructured composite material. Nanoporous silicon itself appears capable of tolerating volume change, as confirmed by the high coulombic efficiency during cycling. At high current density of 1080µA cm^{-2}, a significant drop of coulombic efficiency is observed and we believe this is due to slow lithium diffusion in silicon not allowing for fast response. For application in microbatteries, however, power density is less critical for usage if compared to areal energy density and lifetime. When then current density is lowered back again to its initial value, the anodes completely recover their previous capacity and coulombic efficiency, showing that no irreversible damage of the structure, such as cracking or pulverization, has occurred.

In figure 3.5(a) and (b) high-resolution SEM (HRSEM) images of the cross section of [Si60+C(CVD)], before and after cycling with cutoff voltage of 5mV, clearly show how CVD-deposited C covers the porous Si layer underneath (1µm thick) in a conformal way, without any break in the film continuity or any voids separating the two layers.

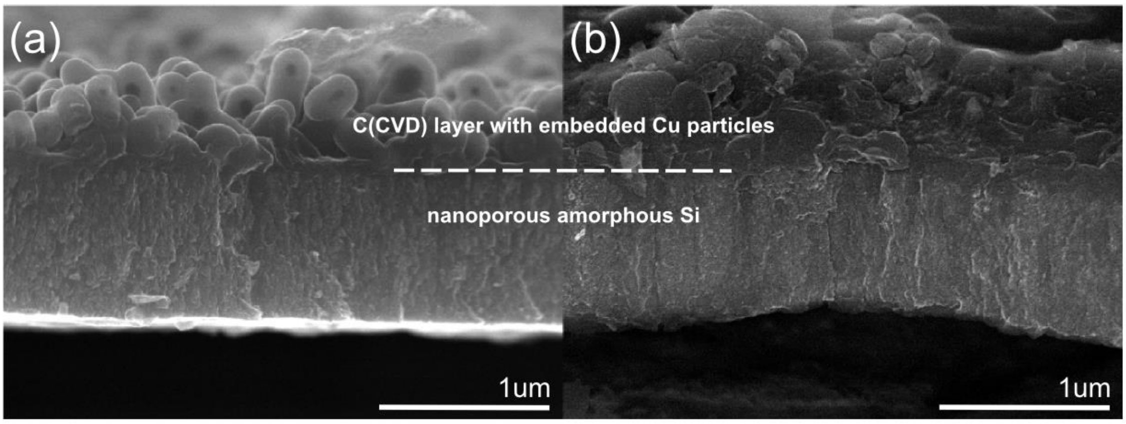

Figure 3.5. HRSEM image of sample [Si60+C(CVD)], (a) before and (b) after cycling (compare to Figure2(f)). The C layer covers the porous amorphous Si (1µm thick) in a conformal way, without breaking the film continuity.

Wave-shaped deformation in figure 3.5(b) is due to sample preparation, i.e. cell opening and anode separation after cycling. Comparison between figure 3.5(a) and (b) confirms that no trace of damage is induced in the film by testing under the harsher conditions of our analysis, i.e. charge and discharge for 1000 cycles, down to the low cutoff voltage of 5mV, with current density up to 1080μA cm^{-2} (see figure 3.4(f)). This can possibly relate to not overcoming the threshold size for cluster crack propagation described above and confirms once more the good robustness of our anodes.

HRSEM, high-resolution TEM (HRTEM) and energy-dispersive X-ray spectroscopy (EDS) analyses on the same samples do not evidence significant compositional, morphological or structural changes of the films between the pre-cycled and post-cycled state, thus allowing for non-separate discussion of the two cases. In particular, electron diffraction analyses, dark-field TEM imaging and HRTEM (not reported here) clearly show the amorphous nature of the Si films, as confirmed by Raman spectroscopic analysis.

High-angle annular dark-field-scanning TEM (HAADF-STEM images in figure 3.6(a) and (b) and EDS maps (c-f), taken on the same area as (b), picture the three overlapped layers of: Cu current collector, nanostructured Si film featured by partial oxidation, and C top covering layer.

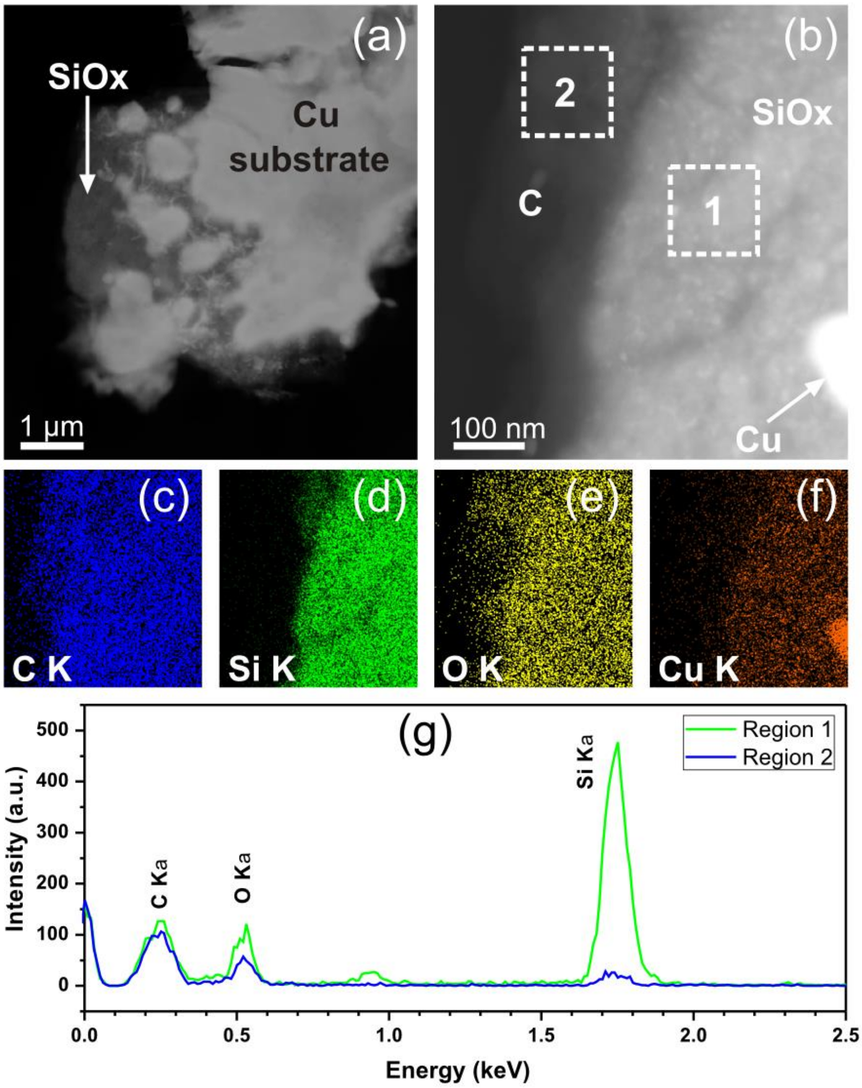

Figure 3.6 (a) Low-magnification and (b) magnified HAADF-STEM images of a fragment of sample [Si60+C(CVD)], lying in plane-view on the carbon support. Three overlapped layers are shown: Cu substrate, SiOx intermediate layer, C covering layer, as shown by the corresponding (c-f) EDS maps of (c) C, (d) Si, (e) O and (f) Cu, all obtained by integration of the Kα peak. In (g), EDS spectra (not normalized) from regions 1 and 2 of (b), including overlapping of SiOx with the C film and only the C film, respectively: while the C content is identical in the two regions (i.e., C has not deeply infiltrated the Si layer), the O content is higher in the Si film. Quantification inside the film, after subtracting the spectrum from the C area, results in the ratio Si/O=3.6.

EDS maps evidence also the presence of nanometric copper grains in C-coated samples, both cycled and non-cycled (figure 3.7).

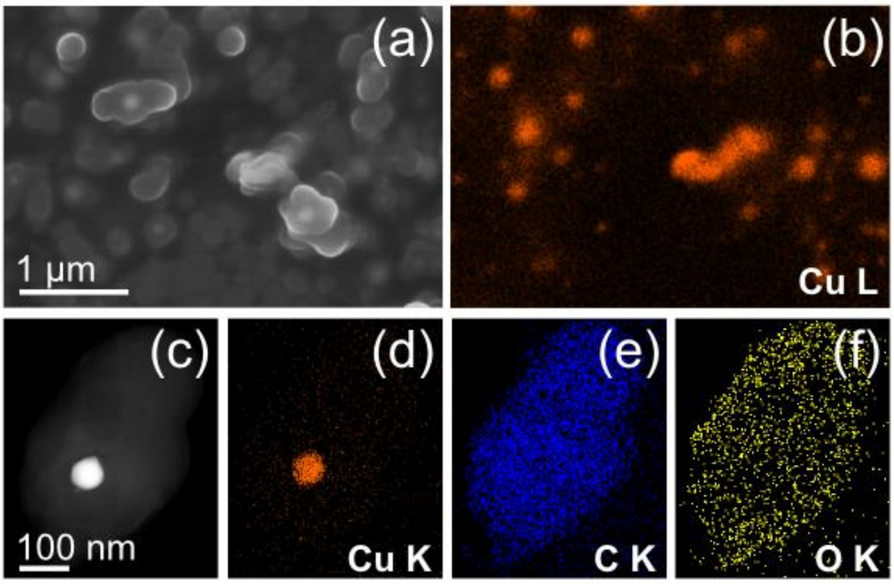

Figure 3.7. (a) Top-view SEM image and (b) corresponding EDS map of Cu (integration of the signal in the Lα series) in the globular structures. (c) HAADF-STEM image of a fragment of the covering C film, which includes a ~60 nm diameter Cu particle, and corresponding EDS maps for (d) Cu, (e) C and (f) O (integration of the signal in the Kα peaks).

In order to estimate the oxygen content in the Si film, EDS spectra (figure 3.7(g)) have been recorded on two regions of identical dimension, selected from the area imaged in figure 3.7(b). One spectrum comes from a region where Si and C are overlapped, while the other one is taken on the region where only the upper C layer with no Si is visible. While the C content is identical in the two regions (i.e. the C contribution to the spectra comes only from the C layer rather than from C possibly infiltrated in the Si layer), the O content is higher in the Si film. Estimate of the O content inside Si film, after subtracting the spectrum from the C area, results in the atomic ratio Si/O=4. This is meant to be an indication value rather than a precise quantification, due to the contribution of the SDD detector itself to the signal (see the low Si Kα peak in the blue spectrum in figure 3.7(g)).

To sum up: on the one hand, introducing a controlled degree of porosity at the nanometric scale in the Si film addresses the problem of volume expansion for silicon (~300%) upon lithiation by creating free space for expansion.

On the other hand, CVD carbon deposition is shown to enhance the mechanical stability of the final anode with respect to the simple Si anode, likely by forming a stable protective SEI layer. Moreover, the moderate temperature required by CVD can benefit the mechanical stability by internal stress relieving via annealing, as recently shown by Hassan et al. [16], and possibly by improving the adhesion of the Si film to the current collector via copper diffusion into Si.

Since from the SEM analysis there is no evident modification of the anode structure and integrity before and after cycling, we claim that the local stresses due to volume changes were not concentrated enough to overcome the threshold for cracking and pulverization. Therefore, we believe that the volume expansion of the Si film has been buffered by the presence of voids in its nanostructure.

The lack of a sharp interface (see figure 3.5) between C and Si, by the two layers being interpenetrated, allows for good electric contact and mechanical adhesion, which again contributes to overall mechanical stability. When C is deposited by CVD, it appears forming in fact a protective conformal layer on Si, which can provide a mechanical barrier to prevent the electrolyte from directly getting in contact with the Si layer underneath, this reducing SEI formation during silicon volume expansion/contraction.

Partial oxidation of Si film as emerges from EDS analysis is also thought to take an active part in the mechanical stability of the anode. As shown in the literature, a certain degree of oxidation can act as a buffer for volume expansion, yet not preventing Si from its alloying with Li in an effective way [17]–[22].

The presence of Cu within the film, as from EDS analysis, can be explained as a result of the thermal treatment during CVD, which is likely to allow for diffusion of Cu into Si and C [23]–[26] and then to strengthen the adhesion of Si film to the Cu substrate, to prevent, in principle, the loss of electrical contact between active material and current collector during cycling [27] and to buffer volume expansion of silicon due to its excellent elastic mechanical property [28], [29].

Conclusions

In conclusion, nanostructured amorphous Si anodes have been produced by PLD in hierarchical mesoporous morphology and successively covered by a C layer deposited by CVD from ethylene. The nanometric porosity allowing for volume expansion and the crucial role of C in the formation of a solid SEI have been exploited by the novel approach.

Capacity retention and rate capability were dramatically improved with respect to bare Si anodes, revealing good stability and no decay for at least 1000 cycles (540µA cm^{-2}). Moreover, the capacity of this anode architecture can be increased by thickening the Si+C film without any negative impact on its mechanical stability and, as a proof, an enhanced capacity of ~175µAh cm^{2} (54µA cm^{-2}) has been reached in anodes as thick as ∼2.5µm. Initial coulombic efficiency can be further increased by addition of a layer of alumina deposited by Atomic Layer Deposition, as shown recently[30], [31] and/or by the use of additives to the electrolyte, such as Fluoroethylene carbonate and Vinylene carbonate, which has proven to promote the formation of a stable SEI and reduce the irreversible losses [32]–[34].

Thanks to the combination of PLD and CVD in a very simple two-step process, it was possible to realize a novel anode architecture, i.e. where C layer conformally covers and protects a porous Si nanostructure, and to achieve promising results in terms of lifetime and rate capability.

Perspective work can focus on increasing the value of capacity by optimizing the involved processes so to define an optimal morphology for the novel cell architecture proposed. Thanks to its versatility, PLD can be then effectively used to deposit both Si and C in one single processing step (as shown later in this chapter), or other Physical Vapour Deposition methods coupled to CVD, thus possibly opening the route to industrially oriented upscaling.

3.2 Anodes made of Si(PLD) on Carbon Nanotubes (CNT)

*In collaboration with **University of Boulder**, Colorado (US) and **IIT-Genova***

The work here described is reported in a manuscript in preparation.

SUMMARY. Similarly to the previous case, Si and C have been coupled in a different anode structure, i.e. nanoporous Si has been grown by PLD on a CNT foil that substituted for Cu as a current collector and participated at the same time in lithiation as active material together with Si. Besides showing good conformal coverage of Si on CNT, the anodes performed in a stable way, i.e. up to 1000 cycles with no capacity fade, with good values of capacity. Because of their mechanical properties, i.e. bendability, these film-anodes can find application in thin flexible batteries, addressing, for example, wearable electronics.

Recently, flexible electronics has attracted much attention, with several works and reviews published on the topic. The possibility to realize devices on flexible substrates for wearable applications, such as roll-up displays, smart mobile devices, implantable bio-sensors and so on, asks for energy supply/storage means with the same characteristics, possibly to be integrated within a single device. Miniaturization of batteries and the need for flexibility can be met by lithium ion microbatteries with a design that provides high energy density and uses flexible substrates. The greatest challenge facing the development of flexible power sources is the fabrication of reliable and efficient shape-conformable components [35]. To further expand the practical application, many innovations of flexible LIBs have been reported mainly concentrated on selecting and developing reliable nano-engineered materials with high mechanical and electrochemical performances as well as appropriate battery structural designs. However, given that flexible electronics is in the early stages of development, no perfect evaluation standards have been established to characterize the corresponding flexible power source devices to date.

The study here presented focusses on developing Si/C anodes for lithium ion microbatteries, where the use of Si addresses the demand for high energy density and carbon is introduced in the form of a foil of nanotubes (CNT) that acts also as a substrate, avoiding the need for a current collector and thus reducing processing/fabrication steps.

CNTs are widely used as flexible conductive scaffolds for loading active electrode materials owing to the high surface area, small diameter and excellent electrical conductivity [35]. As reported by Wang et al. [36], the CNT current collectors functioned as excellent mechanical supports and enabled efficient electron transfer and lower contact resistance at the electrode–CNT interface with respect to metal current collectors, resulting in improved cycling stability, rate capacity, and gravimetric energy density. In addition, CNT provide a rough surface that can enhance the adhesion to electrode materials and thus facilitate interface contact.

In the work by Fu et al. [37], a layer of nanometer-sized silicon was coated on sheets of CNT by CVD to form a free-standing, binder-free, and flexible anode. The CNT sheet provides a high surface area and porous structure to facilitate the electrochemical kinetics between the active material Si and electrolyte. As a result, the flexible Si/CNT composite electrode showed stable cycling performance for 100 cycles without dramatic capacity loss. However, Si deposition by CVD requires high processing temperatures (625 °C) and harmful gases (SiH_4, silane).

This work proposes an alternative way to prepare Si@CNT at room temperature without harmful gases by means of PLD. These flexible, self-standing anodes showed a stable electrochemical behaviour up to 1000 cycles.

The advantages with respect to the approach presented in Section 3.1 are in the need for only one processing step, i.e. room temperature PLD, provided that the substrate for deposition, i.e. CNT foil, is available on the market. It is true, though, that preparing CNT foils, even on an industrial scale, requires more expensive and time-consuming processes than preparing a Cu laminated sheet and the more demanding requirements of flexible devices could justify this increase. All of these aspects should be considered when evaluating the whole time&cost processing effort for preparing these anodes on a large scale, but a detailed discussion goes beyond the scopes of this dissertation.

Film fabrication

Si is deposited at room temperature by PLD, choosing one of the morphologies already investigated and presented in Chapter 2, i.e. the one deposited at 60Pa Ar:H_2. These process parameters allow for a meaningful balance between introducing a considerable amount of pores in the film and preserving its mechanical stability, as discussed in the previous example (Section 3.1). Instead of using copper discs as substrates for Si growth, which had the role of current collectors in the final cell, Si was deposited on discs cut out of a commercial foil of CNT that constituted a flexible substrate.

Electron Microscopy: SEM and TEM (in collaboration with IIT-Genova)

HRSEM images were taken by means of a JEOL JSM-7500F instrument, equipped with a cold field emission gun source and operating at 5 kV, on anodes where the Si film on top of the CNT foil is 1µm thick (nominal).

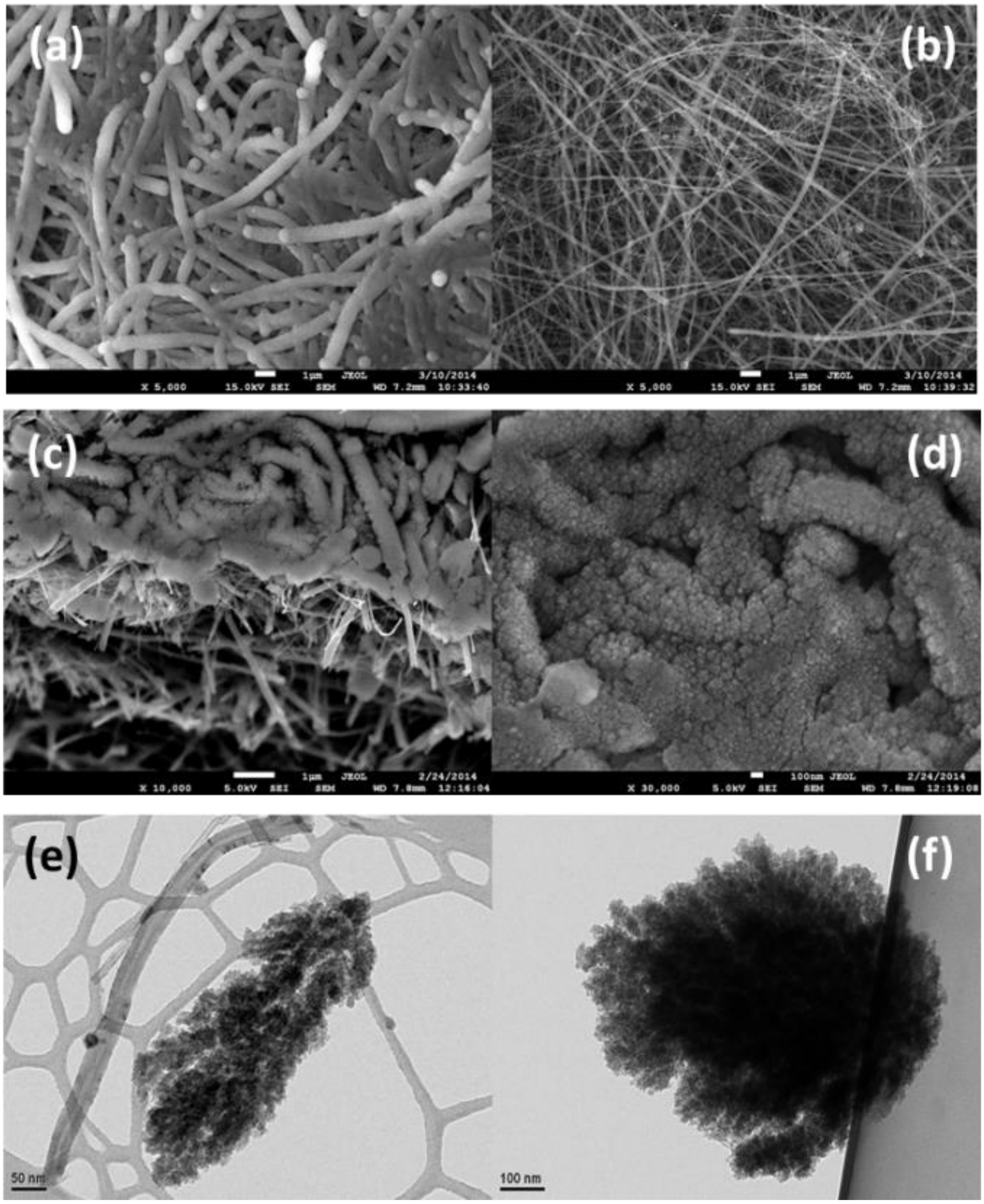

Figure 3.8. Top view SEM images of Si@CNT (a) and bare CNT foil (b). Cross-section images showing conformal covering of CNT by Si (c) and zoomed view of the Si morphology (d). TEM images of Si covering a carbon nanotube (e and f).

Imaging in top view (figure 3.8(a,b)) clearly shows the difference between the pristine sample (only CNTs in figure 3.8(b)) and the sample after the silicon film deposition (figure 3.8(a)). Figure 3.8(c) clearly shows that, due to the high presence of voids given from the CNTs, the silicon film has grown preferentially on each CNTs instead of forming a uniform layer. The Si film fabricated by

PLD exhibits the morphology (highlighted in figure 3.8(d) of the previously analyzed samples (see Chapter 2), i.e hierarchically nanostructured with mesoporosity.

TEM imaging and electron diffraction analyses were carried out with a Jeol JEM 1011 instrument, operated at 100 kV, equipped with a thermionic tungsten source. The sample, due to the really weak and soft nature of the CNTs disc, has been prepared by picking a small quantity of film with the tweezers and dispersing it in toluene, successively dropped onto a holey carbon coated grid. Bright field (BF) images in figure 3.8(e, f) confirmed the hierarchical structure of the silicon film.

From SEM and TEM images, it is clear to see that the Si film, while uniformly covering the carbon surface, keeps its granular morphology and this promotes the formation of a porosity that consists of inter-cluster voids.

In order to roughly assess the bendability of these Si@CNT anodes, a disc was bent on one of its diameters for 30 times in both directions out of its plane, so as to alternate traction-compression stresses on the film. From HRSEM images (figure 3.9(a-d)) taken from an area of the sample close to its diameter, i.e. in highest strain conditions, the film looks almost unaltered with respect to the unstressed state and Si remains attached to CNT (figure3.9(a, b)). Only in some spots, Si detaches from the nanotubes, as shown in figure 3.9(d).

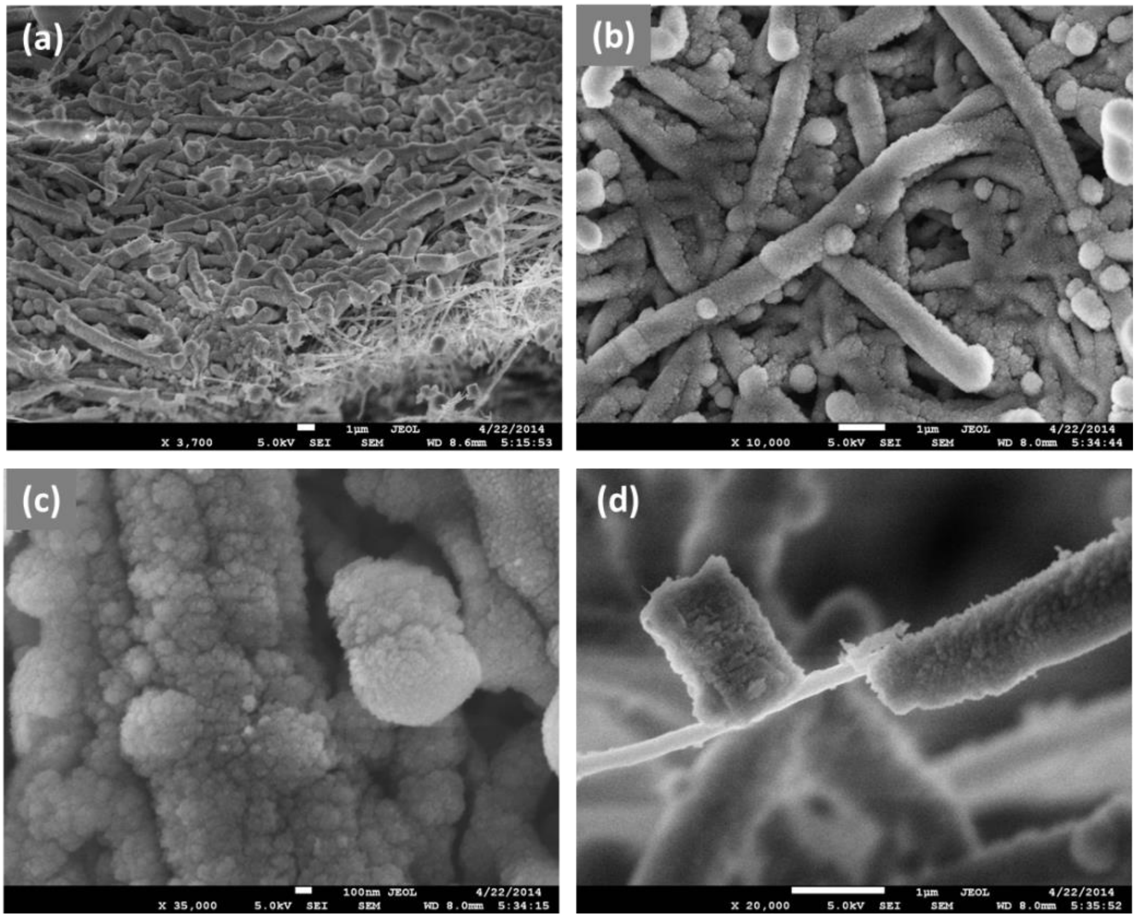

Figure 3.9 HRSEM images of Si@CNT after mechanical test. No visible damage is observed either in cross section (a) or plan view (b). (c) Zoomed view of the silicon clustered film. (d) In some spots, silicon is detached from CNT.

Cell assembling and electrochemical testing (in collaboration with University of Boulder, Colorado (US))

Films as thick as 3.5 µm were also prepared and their electrochemical behaviour tested in electrochemical cells. Half cells were assembled with Si on CNT discs as working electrodes and Li metal foil as counterelectrode. The electrolyte was 1 M $LiPF_6$ dissolved in a 1:1 (volume ratio) mixture of ethylene carbonate (EC) and diethyl carbonate (DEC); the separator was a glass micro-fibre disc (Whatman GF/F), and the shell was a stainless steel CR2032 coin cell (VWR Inter.). Cells were then tested with an Arbin 2000 battery test station under constant current conditions, within the voltage range 1.5V - 5mV.

Results and Discussion

In figure 3.10 cyclic charge/discharge curves of the anodes under analysis are presented under different testing conditions. Cycling was first performed under constant-current density with step-increasing values every 16 cycles, so to test the rate capability (figure 3.10 (a)). Then, the current density was fixed to its upper value (1080µA cm^{-2}) and the cells let charge and discharge up to 1000 times (figure 3.10(b)).

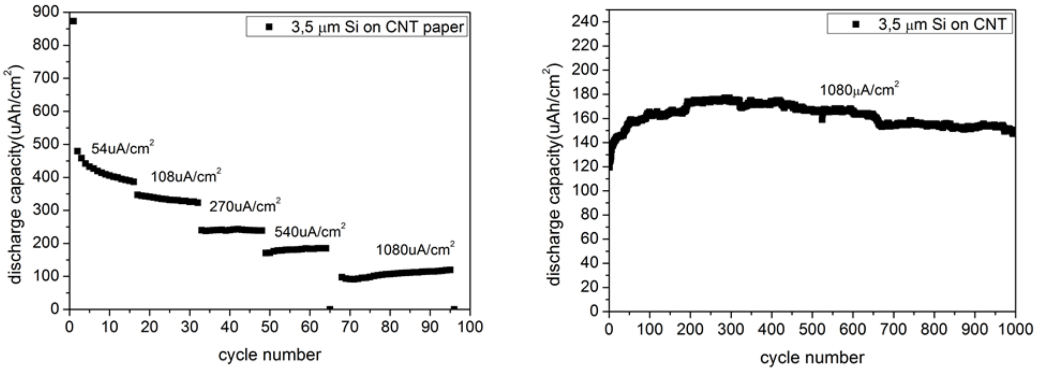

Figure 3.10. Galvanostatic charge/discharge curves of Si@CNT in (a) C-rate test and (b) longlife test, showing stable behaviour up to 1000 cycles

The initial capacity of ~870 µAh cm^{-2} is partially lost in the first cycle in irreversible processes, such as the formation of the SEI layer, resulting in a 48% losses. Upon increasing the C-rate, the cell respond with a loss in capacity, probably due to the faster kinetics imposed that does not allow to extract and insert all of the lithium available. Even under these “stressful” conditions (current density of 1080 µA cm^{-2}), the cells behave in a very stable way, showing almost with no irreversible losses up to 1000 cycles (3% losses in the last 300 cycles).

Conclusions

This study has proven the feasibility of fabricating Si-C anodes by PLD on a flexible substrate. Si growth by PLD is based on the experience acquired in previous studies, while the carbonaceous content is provided by the CNT foil that acts both as a substrate for Si deposition and as the current collector for the anode. In this way, a self-standing anode is produced where the active material is made of carbon conformally coated by silicon. The anodes show promising electrochemical behaviour, with initial capacity of ~870 µAh cm^{-2} for a 3µm-thick anode and a stable behaviour up to 1000cycles. As shown in the previous Section (3.1), the anode capacity can be increased by thickening the silicon layer.

Compared to the anodes presented in Section 3.1, these Si@CNT anodes provide comparable performances in terms of capacity and stability (at least 1000cycles reached with very low loss-per-cycle), especially because this result is obtained under “more stressful” conditions, i.e. at higher current density (1080µA/cm^2 for Si@CNT vs 540µA/cm^2 for Si(PLD)+C(CVD)).

Si@CNT is then a promising solution to fabricate self-standing Si-C nanostructured anodes in only one processing step at room temperature.

Progresses of this work should involve a thorough study of the Si layer on two key aspects, i.e. cluster dimension and thickness. The optimum thickness of the Si layer balances the need to increase the overall capacity (thick layer preferred) with that of avoiding mechanical stiffening of the anode, as required by flexible devices (thin layer preferred). The optimum cluster dimension, achieved by controlling gas pressure during deposition, should allow for good coverage and adhesion to the CNT (smaller cluster preferred) and for introducing a certain degree of porosity in the film (larger clusters preferred) to allow for volume changes.

3.3 Anodes made of Si(PLD) without C

*In collaboration with **CSHR-IIT**, Torino (IT)*

The work here described is reported in the manuscripts: “Mesoporous Silicon Nanostructures by Pulsed Laser Deposition as Li-ion Battery Anodes” E. Biserni, N. Garino, A. Li Bassi, P. Bruno, C. Gerbaldi, accepted for publication in ECS Transactions, and its updated version, with the same title and authors, to be submitted to RSC Advanced.

SUMMARY. This work is meant to investigate the effect of morphology on electrochemical properties of bare Si nanostructured porous anodes prepared by PLD, in order to optimize the Si films. BET analysis on the porosity and electrochemical tests, together with SEM observation of the film morphology allowed for identifying an optimum structure where the degree of porosity is high enough to allow for volume expansion and low enough to avoid embrittlement of the whole film. The best performing samples allowed for good initial capacity approaching 300 µA cm^{-2} and

improved stability over the initial 30 galvanostatic discharge/charge cycles. This study has the aim to optimize the film engineering as far as the Si part is concerned, but C is nevertheless required when real applications are sought, because of its "stabilizing" effect.

The promising results obtained with anodes made of Si(PLD)+C(CVD) as described in section 3.1, opened the way for a deeper investigation of the behaviour of silicon film grown by PLD. Final target is the optimization of the film morphology to be coupled with C.

Among the Si films presented in Chapter 2, we chose to study the relationship between morphology and electrochemical behaviour of films produced in Ar:H_2 at 40Pa, 60Pa and 100Pa, because their porosity results interesting for LIB applications, as shown in the work on Si(PLD)+C(CVD). After native oxide removal by means of citric acid, copper discs were used as a substrate for Si deposition by PLD, so to act as the current collector for the active anode material in lithium cell.

The thickness of Si films was set to be approximately 1 µm, as shown in images 3.11(a), (c) and (e) where the low magnification cross-sectional views of the different amorphous silicon films were acquired by a Supra 40 Zeiss Field Emission Scanning Electron Microscope (accelerating voltage 3-5 kV), together with zoomed views of their columnar mesoporous algae-like structure (figure 3.11 (b), (d), and (f)).

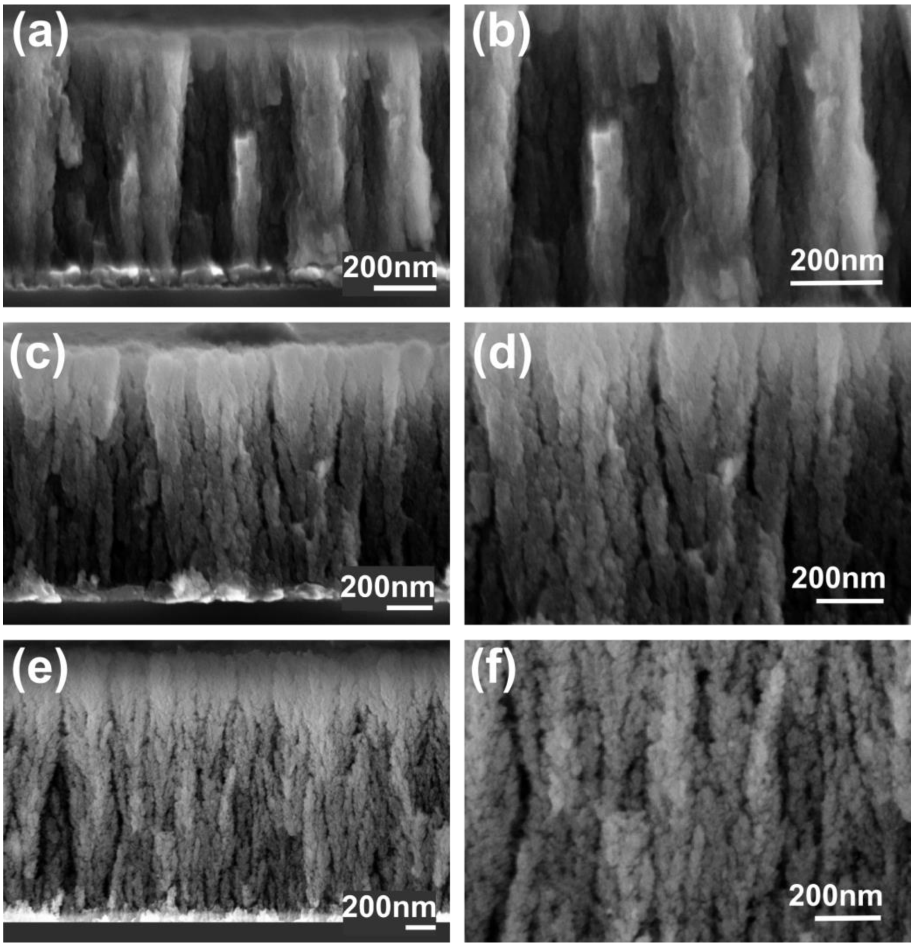

Figure 3.11 SEM cross-sectional images showing the different morphology of the mesoporous silicon nanostructured films grown at increasing background gas pressure, as presented in Chapter 2: (a, b) 40Pa, (c, d) 60Pa, (e, f) 100Pa.

Our collaborators at the CSHR-IIT in Torino (IT) performed an analysis on the film porosity, based on the Brunauer, Emmet, Teller (BET) method[2], by a Quadrasorb evo™ (Quantachrome Instruments). Prior to adsorption, approximately 100.0 mg of solid were placed in the cell and evacuated at about 50 °C for 2 h and, successively, at 200 °C for 3h.

The electrochemical response in liquid electrolyte of the samples was tested at CSHR-IIT in polypropylene three-electrode T-cells assembled as follows: a Si film disk (area 0.785 cm^2) as the working electrode, a 1.0 M lithium hexafluorophosphate ($LiPF_6$, Solvionic, France, battery grade) in a 1:1 w/w mixture of ethylene carbonate (EC) and dimethyl carbonate (DMC) electrolyte solution soaked on a Whatman® GF/A separator and a lithium metal foil (high purity lithium foils, Chemetall

---

[2] BET theory was elaborated to determine the specific surface area of a porous material and is based on the physical adsorption of a gas on the surface of the solid. The material, surrounded by gas at a certain temperature and relative vapour pressure p/p_0, adsorbs physically a certain amount of gas, proportional to the total surface of the material [50]. The determination is usually carried out at the temperature of liquid nitrogen.

Foote Corporation) as the counter electrode. For cyclic voltammetry (CV), a second lithium foil was added at the third hole of the cell, in direct contact with the electrolyte, acting as the reference electrode. Galvanostatic discharge/charge cycling (cut off potentials: 0.02 – 1.5 V vs. Li^+/Li) and CVs (between 0.02 and 1.5 V vs. Li^+/Li, at 0.1 mV s^{-1} scan rate) were carried out at ambient temperature on an Arbin Instrument Testing System model BT-2000. Clean electrodes and fresh samples were used for each test. Procedures of cell assembly were performed in the inert atmosphere of a dry glove box (MBraun Labstar, O_2 and H_2O content < 1 ppm) filled with extra pure Ar 6.0.

Results and discussion

An estimate of the densities of these films is provided in Chapter2, with a value of 0.36 g/cm^3 for the sample 100 Pa, 0.92 g/cm^3 for 60 Pa and 1.66 g/cm^3 for 40 Pa, which, if compared to the density of 2.33 g/cm^3 of bulk silicon, result in an estimated porosity of about 85%, 60% and 29%, respectively.

Accurate determination of specific surface area (SSA) in porous Si is usually performed through BET technique that analyses the adsorption/desorption isotherms of gases at low temperature [38]. Nitrogen adsorption-desorption isotherms, shown in figure 3.12 (a-c), are mainly classified as type IV isotherms with a hysteresis loop [39].

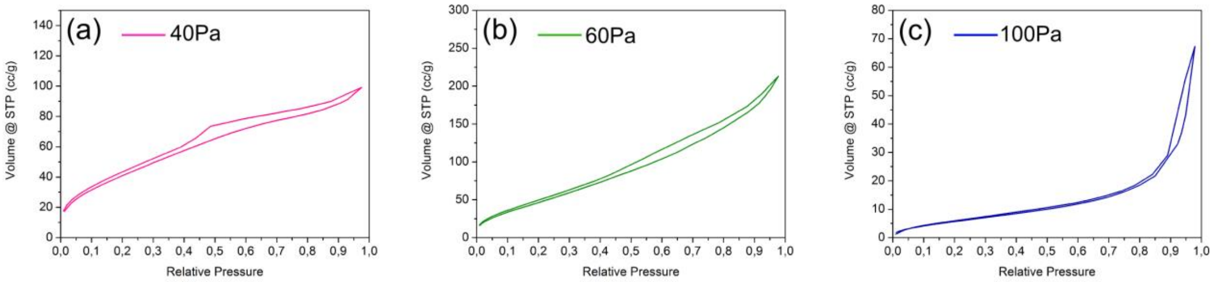

Figure 3.12 Isothermal profiles of samples prepared at increasingly higher applied deposition pressures: (a) 40Pa, (b) 60Pa, (c) 100Pa

This type of isotherm denotes a mesoporous material (pore diameters of 2–50 nm) with the hysteresis loop being associated with the capillary condensation of nitrogen within the mesopores. In details, the relative pressure at which the hysteresis of adsorption/desorption is recorded in the isothermal curves can account for the different pore size distribution in films having different morphology. By comparing BET data of figure 3.12 with SEM images presented in figure 3.11, two orders of porosity can be traced in each of the three films. The “first-order” porosity is the one given by large intra-algae pores with diameter size in a range of tens to hundreds of nanometers (see SEM images of figure 3.11) and gives rise to the hysteresis in the low partial pressure range of the isotherms. The “second order” porosity is instead the one of voids between clusters composing each single algae of the film; these have a diameter in a range up to tens of nanometers and contribute a hysteresis in the high partial pressure range to the isothermal profile. In sample 40Pa, the “first order” porosity dominates the overall porosity, as from the position of the hysteresis in the isothermal profile as well as visually confirmed by SEM pictures. On the contrary, the “second” order porosity becomes more important in films produced at higher pressure. As a consequence, the hysteresis in the isotherms shifts towards the range of higher partial pressures; this is particularly evident in sample 100 Pa, where almost only the “second” order porosity is present. Exploiting the BET theory, the following values of specific surface area were obtained for each sample prepared varying the deposition pressure: 68 m^2 g^{-1} for sample 40 Pa, 109 m^2 g^{-1} for sample 60 Pa and 189 m^2 g^{-1} for sample 100 Pa. As expected, surface area values increase almost linearly with the increase in the applied deposition pressure from 40 to 100 Pa, in good agreement with previous literature on porous films by PLD both for silicon or other materials [40], [41].

Raman analysis on the as-prepared Si nanostructured anodes before electrochemical tests reveals the amorphous character of their structure (see figure 3.13), as from the characteristic Gaussian bands centred around 145, 330, 430 and 490 cm^{-1}, that are generally attributed to the transverse acoustic (TA), longitudinal acoustic (LA), longitudinal optic (LO) and transverse optic (TO) modes of amorphous silicon, respectively [42]. In addition, only in samples 100Pa, a small peak appears at 514-517 cm^{-1}, which is attributed to the presence of Si nanocrystals in the amorphous matrix, consistently with what reported in Chapter2.

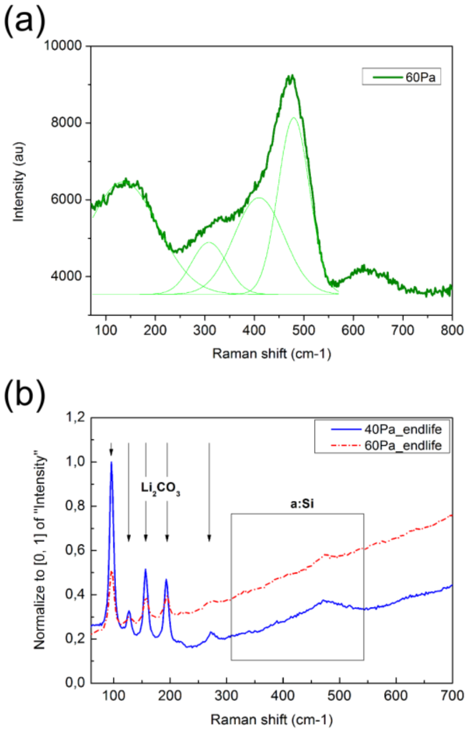

Figure 3.13 (a) Raman spectrum (thick line) of the mesoporous silicon 60 Pa sample, representative for all the samples prepared; the spectrum was fitted by the characteristic Gaussian curves of amorphous silicon (thin lines) (b) Post-mortem Raman spectra of nanoporous silicon anodes. Together with the large band of amorphous silicon, the peaks of Li2CO3 are highlighted.

After electrochemical tests, some of the cells were opened to characterize their *post-mortem* status; Raman spectra of the anodes were acquired after their washing in EC: DEC in order to remove residual glass-fiber from the separator. In addition to the bands of amorphous silicon, the spectra reveal on all of the samples the presence of intense and sharp peaks at 96, 127, 156, 193, 273 cm^{-1} that constitute the fingerprint of lithium carbonate (Li_2CO_3). As reported in several studies in the literature, Li_2CO_3 comes from the electrolyte decomposition in those systems that use $LiPF_6$ as the salt dissolved[43]–[46].

The room temperature electrochemical behaviour was evaluated in laboratory scale lithium test cells and carried out by means of cyclic voltammetry and galvanostatic discharge/charge cycling at various current regimes. Results are shown in the plots of figure 3.14 (a-c). Note that the electrodes were used as-grown on the Cu current collector, without any addition of binders and/or conducting additives.

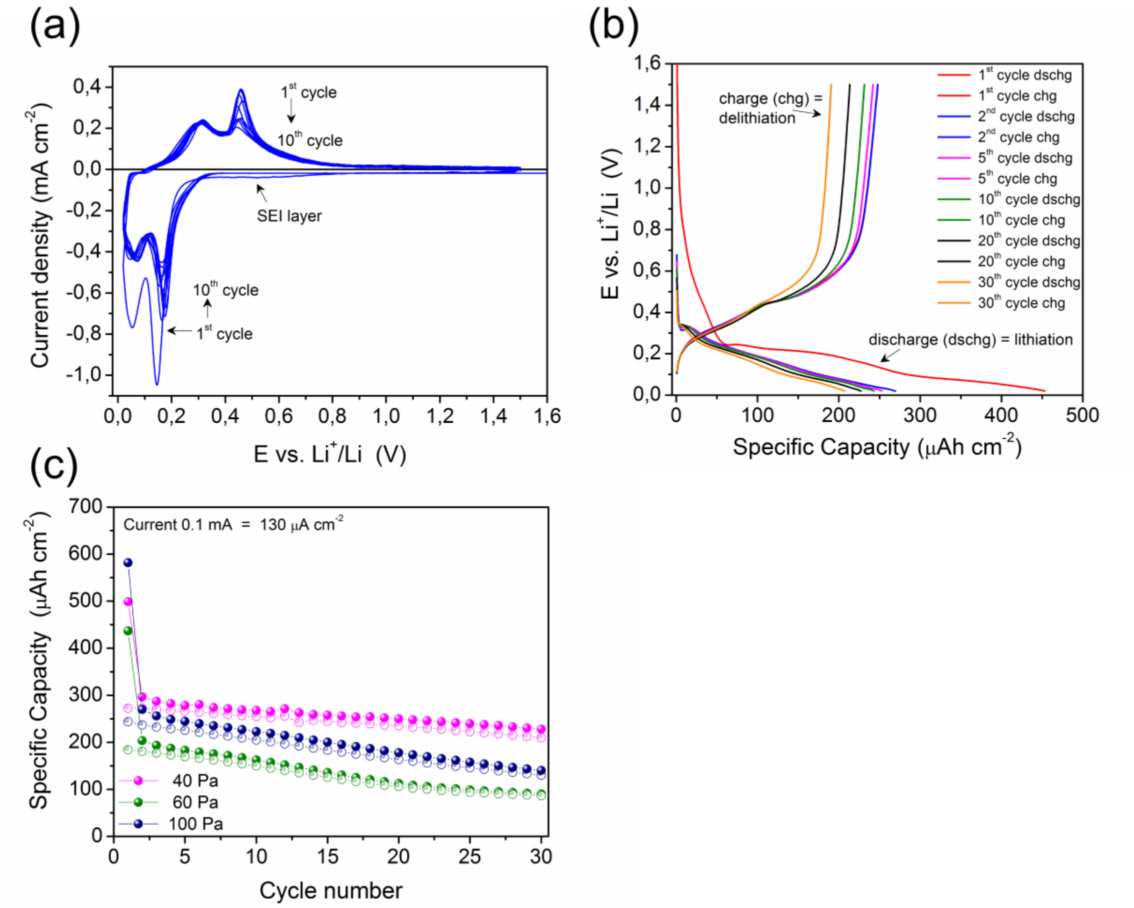

Figure 3.14 Room temperature electrochemical behaviour in lithium test cells of as-grown mesoporous silicon nanostructures: (a) cyclic voltammetry (cycles 1-10) in the potential range of 0.02–1.5 V vs. Li+/Li at a scan rate of 0.1 mV s^{-1}, (b) galvanostatic discharge/charge potential vs. specific capacity profiles, (c) specific capacity vs. cycle number.

The typical cyclic voltammetric response of the porous silicon nanostructures prepared by PLD, in particular of sample 40 Pa representative of all of the samples prepared, is shown in figure 3.14 (a) in its initial 10 cycles. It was performed at the scan rate of 0.1 mV s^{-1} between 0.02 and 1.5 V vs. Li^+/Li. The cyclic voltammograms (CV) show the typical behaviour of silicon electrodes upon reversible alloying/dealloying reactions with lithium ions [47], [48], resulting in two main couples of anodic and cathodic peaks. In details, in the initial scan towards lower potential values, it shows two cathodic peaks at below 0.2 V vs. Li^+/Li (i.e., around 0.15 V as the dominant, and around 0.05 V), characteristics of the lithiation step into amorphous silicon. These are reflected in the following anodic scan, where the two corresponding broad anodic peaks, centred at about 0.3 V and 0.47 V vs. Li^+/Li, indicate a two-step lithium extraction process from the Li–Si alloy back to amorphous Si. In the second cathodic scan, the broad cathodic peaks slightly shift towards higher potential values (e.g., the dominant centred at ca. 0.18 V). It is supposed to come from a slightly different kinetics in the alloying process due to the formation of slightly different metastable amorphous Li_xSi phases according to the previous literature [49]. Regarding the formation of the solid electrolyte interphase (SEI) layer, it appears in the first cathodic scan as a broad faint signal between 0.6 V and 0.4 vs. Li^+/Li.

The profiles of discharge (lithiation) and charge (delithiation) potential vs. time for sample 40 Pa, representative for all the samples prepared, are plotted in Figure 3 (b). The charge/discharge current rate used for each sample was 0.1 mA, corresponding to about 130 μA cm^{-2}. Profiles show the typical features of amorphous silicon electrodes, with an initial discharge cycle being rather different from the following ones due to the formation of the SEI layer and to the presence of a high oxygen content at the surface of the electrode, as usual for amorphous silicon nanoparticles. This causes the relatively large irreversible capacity loss which results in low initial coulombic efficiency for these kind of electrode materials.

The cycling performance of porous silicon nanostructures as a lithium-ion battery anode is reported in Figure 3 (c).

The first 30 galvanostatic cycles show good initial capacity higher than 200 μAh cm^{-2} for all of the three porous films, with a capacity loss of around 40 % for sample 40 Pa and 50 % for both 60 Pa and 100 Pa upon initial lithiation; this is a reasonably low value for losses if compared to similar high-surface-area silicon nanostructures reported in the literature[48]. Based on the kind of synthesis adopted in the present work, the sample having lower surface area available for reaction with the electrolyte, i.e. the one prepared at a pressure of 40 Pa, show in fact lower capacity loss during first lithiation. This reflects also in the overall electrochemical behaviour, which is superior both in terms of higher specific capacity values and stability upon reversible cycling, and results in the highest value of capacity retention (around 77 %) after 30 discharge/charge cycles in lithium cell.

Conclusions

Mesoporous silicon anode nanostructures fabricated by PLD were characterized and electrochemically tested in lithium test cells. Different deposition pressures were applied in order to evaluate the influence of this process parameter on the morphological/electrochemical characteristics of the resulting nanostructures. The samples prepared at lower deposition pressure, having porosity featured by larger average pore size and lower surface area, show good initial capacity approaching 300 µA cm^{-2} and improved stability over the initial 30 galvanostatic discharge/charge cycles.

The improved stability in samples with larger pores can be related to their lower surface area. On the contrary, the higher surface area of the samples with smaller pore dimension (samples 60 Pa and 100 Pa) is likely to be responsible for their increased capacity fade; more surface area is involved, in fact, in the side reactions with the electrolyte and, hence, more capacity is lost in forming the interphase layer. The appearance of intense peaks attributed to Li_2CO_3 in the Raman spectra confirms that losses due to the SEI formation are relevant to the working of our anodes.

Summarizing, the focus of this work was to explore the relationship between morphology and electrochemical behaviour of the mesoporous silicon films prepared by PLD and used as anodes in LIB.

Once this first investigation has been carried out, and an optimum film structure identified, the fabrication strategy has to address the improvement of cycling stability to reach long-term operation. To do so, the addition of one or more carbonaceous layers is proven to be helpful, as from the example of Si(PLD)+C(CVD) described in section 3.1.

3.4 Multilayered anodes made of Si(PLD) and C(PLD)

*In collaboration with **CSHR-IIT**, Torino (IT) and **Nanyang Technological University** (Singpore)*

The work here described is reported in a manuscript in preparation.

SUMMARY. The aim of this work is to prepare Si-C composite anodes in one single fabrication step. The anodes have a multilayered structure where Si and C are fabricated both by PLD by alternating two targets during the deposition. C has the role to improve the overall electrical conductivity (intermediate layers) and to promote the formation of a stable SEI (top layer). The effect of mild annealing (400°C) on these structures, which is supposed to improve the mechanical properties in terms of stress relaxation and adhesion to the Cu current collector, is investigated and proves to effectively increase the stability over cycling.

Moving from the conclusions of the previous sections, we here describe an improvement of Si anodes by PLD. The strategy that we adopted aimed at obtaining Si+C films with a simplified process, i.e. single-step fabrication by PLD. Reducing processing steps and processing time is one of the key aspects when upscaling is sought.

PLD allows for depositing different materials in one single batch process, either by using composite targets with the desired composition or by co-deposition from two different targets ablated at the same time (with rotating targets, this can be achieved by a single target made of separate zones of different materials that are alternatively ablated during rotation). We chose to deposit Si and C by means of two separate targets mounted on a switchable target holder to grow alternatively Si or C into a multilayered film. After deposition of the desired amount of one material, the laser was stopped for a while and the target holder switched without opening the vacuum chamber, so to expose the other target to ablation. In this way, multilayered structures were grown where Si and C were alternated 9 times (10 layers, 5 couples Si-C), starting with Si in contact with the copper collector and terminating with C on top of the whole stack. The top layer of C has the role promote the formation of a stable SEI, while the C layers in between of the stack are meant to improve the overall electrical conductivity and buffer the volume expansion of the Si layers.

Film fabrication

Three types of anodes were prepared, with Si deposited under the same conditions described in section 3.3, i.e. in 40Pa, 60Pa and 100Pa Ar:H_2, and C always deposited at 5Pa Ar:H_2. Samples are named Si/C-40, Si/C-60 and Si/C-100 where the number is the deposition pressure for Si. Deposition time for C was fixed to obtain a 70nm-thick layer, i.e. one third of the ~200nm-thickness of each coupled Si-C layer, while for Si layers grown at different pressures the deposition time was tuned to have a ~130nm-thick layer and thus obtain a final overall film thickness of 1µm. The overall thickness of 1µm was chosen to allow for comparison with the other approaches described in this chapter, while the parameters for deposition of C (gas pressure and time) were set so as to obtain a uniform layer able to cover the underlying Si. C-layer relative thickness was a non-optimized starting point balancing on the one hand the need for a well-defined C layer, possibly able to pin Si expansion, and on the other hand to have enough Si to consider the final anode as Si-based.

Except for reference samples, the anodes were then annealed in a closed furnace filled with Ar: H_2 to relieve internal mechanical stresses and possibly promote adhesion of the Si layer to copper substrate, as proven by experimental results described in section 3.1. With respect to the experience with CVD described in section 3.1, here the temperature was nearly halved, because processing at lower temperatures has to be preferred in view of larger scale applicability. The samples were heated at a rate of 4°C/min up to the temperature of 400°C, hold for 5 minutes at 400°C and then let cool down.

Electron Microscopy (SEM)

Cross-sectional views of the multilayered films were acquired by a Supra 40 Zeiss Field Emission Scanning Electron Microscope (FESEM, accelerating voltage 3-5 kV) and are shown in figure 3.15. In samples with Si grown at (a)40Pa and (b)60Pa, the alternated Si and C stack is clearly visible, unlike the more porous samples (c) with Si deposited at 100Pa. Probably, the higher porosity of the single Si layer provides a rough surface for C deposition, that can then infiltrate into Si instead of forming a separate layer.

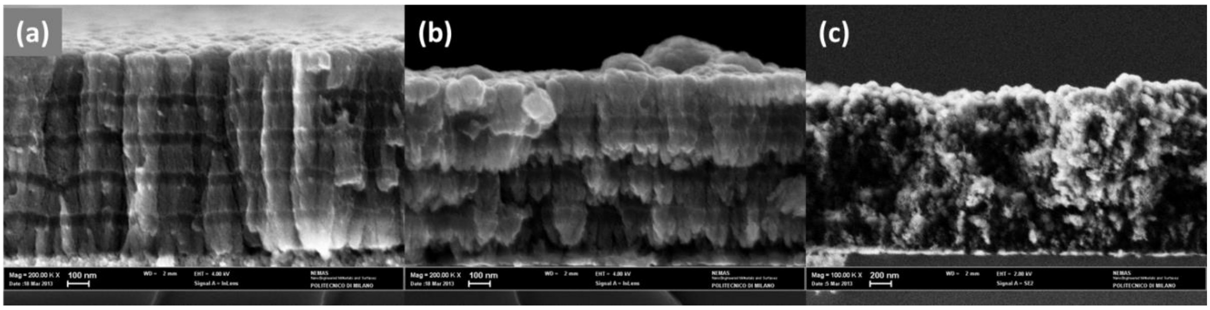

Figure 3.15 Cross-sectional views of the multilayered films where Si is grown at different pressures (a) Si/C-40; (b) Si/C-60 and (c) Si/C-100.

Cell assembling and electrochemical testing (in collaboration with IIT Torino and Nanyang Technological University (NTU)

Cells were then assembled in collaboration with the CSHR-IIT in Torino (IT) and preliminary tests were conducted during a short stay at the Nanyang Technological University of Singapore in Prof. Alex Yan Qingyu's group under the supervision of Dr. Ulaganathan Mani.

The electrochemical response in liquid electrolyte of the samples was tested at CSHR-IIT in swagelok-type cells assembled as described in section 3.3.

Results and Discussion

Multilayered Si/C anodes of the three types were tested under constant current conditions between 0.02 V and 1.5 V (vs. Li^+/Li). Galvanostatic charge/discharge curves of the reference samples (not annealed) were affected by a rapid drop in capacity during the first cycles, with less pronounced losses in samples with Si grown at 40Pa.

Annealed samples showed instead good cyclability, with Si/C-40 being the most stable anode of the series, in agreement with the findings reported in section 3.3 about the most stable silicon anode morphology. Charge/discharge curves of annealed Si/C-40 are shown in figure 3.16 for the first 100 cycles, together with coulombic efficiency. The initial capacity of ~380μAh cm^{-2} is lost at 15% in the first cycle and then stabilizes to a value of about 290μAh cm^{-2} for the following 100cycles. Also coulombic efficiency stabilizes after the first cycles, rapidly reaching 99%.

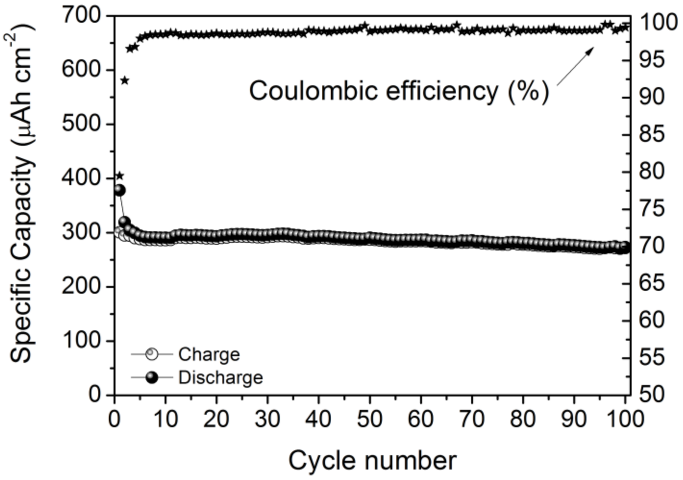

Figure 3.16 Galvanostatic charge/discharge curves of Si/C-40 with coulombic efficiency

The annealing step proves to be beneficial for the stability of the anodes, confirming the explanations provided in section 3.1 about CVD-induced effects. The annealing performed at 400°C is effective for internal stress relaxation and is supposed to promote adhesion of the Si film to copper substrate.

Conclusion

Alternated deposition of Si/C layers by PLD has proven to be a straightforward method to produce multilayered anodes in one processing step. With respect to bare silicon anodes presented in section 3.3, the addition of carbon and mild annealing at 400°C stabilize the electrochemical performance of the anodes in lithium half-cells, allowing to reach at least 100 cycles with contained capacity losses.

Further developments of this work shall include a thorough study of the effects of annealing at different temperatures. This would lead to a definition of an optimum temperature, i.e. the minimum one for the stabilizing effect to occur. This would provide useful information for the successive integration of the annealing step into the deposition process, by means of a heated sample-holder. This would further reduce fabrication steps, making it possible to deposit and anneal Silicon and carbon in one single step.

3.5 Conclusions to Chapter 3

Compared to the combined PLD-CVD approach described in Section3.1, the fabrication method for multilayered Si-C anodes described in Section 3.4 is also based on a two-step process, where the annealing step involves lower temperatures (400°C vs 825°C). Temperature in this annealing procedure has no lower limit but the one given by the effectiveness of stress relieve, while in the case of Si(PLD)+C(CVD) its lower limit is fixed by the occurrence of ethilene decomposition and hence cannot be varied. The possibility of lowering the annealing T gives then more versatility to the approach of Section 3.4, especially with the possibility of integrating the annealing step into the PLD process, by means of a heated sample-holder. It is worth noting, though, that while electrochemical tests have proven the stability of Si(PLD)+C(CVD) anodes up to 1000 cycles, the behaviour of the multilayered PLD- anodes is still to be tested for long cycling.

The long-life stability up to 1000 cycles has been proven, instead, for Si@CNT anodes, that provide an interesting solution to fabricate Si-C self-standing anodes at room T in only one processing step. This approach was designed to obtain self-standing anodes with minimized processing steps/times/cost and it appears promising for flexible battery applications.

All of the three proposed solutions address the two main critical issues of Silicon anodes in LIB, i.e. volume expansion and stable SEI formation, by engineering Si-C composite nanostructured anodes that show good stability over cycling. The process-flow to obtain them, mainly based on PLD, was designed to minimize the required steps and reduce the involved temperatures.

References

[1] E. Biserni, M. Xie, R. Brescia, A. Scarpellini, M. Hashempour, P. Movahed, S. M. George, M. Bestetti, A. Li Bassi, and P. Bruno, “Silicon algae with carbon Topping as thin-film anodes for lithium-ion microbatteries by a two-step facile method,” *J. Power Sources*, vol. 274, pp. 252–259, Oct. 2014.

[2] E. Biserni, A. Scarpellini, R. Brescia, D. Dellasega, A. Li Bassi, and P. Bruno, “Room temperature fabrication of silicon nanocrystals by pulsed laser deposition,” *J. Nanoparticle Res.*, vol. 16, no. 6, p. 2461, May 2014.

[3] H. Richter, Z. P. Wang, and L. Ley, “The one phonon Raman spectrum in microcrystalline silicon,” *Solid State Commun.*, vol. 39, no. 5, pp. 625–629, Aug. 1981.

[4] Y. Duan, J. F. Kong, and W. Z. Shen, “Raman investigation of silicon nanocrystals: quantum confinement and laser-induced thermal effects,” *J. Raman Spectrosc.*, vol. 43, no. 6, pp. 756–760, Jun. 2012.

[5] A. C. Ferrari and J. Robertson, “Interpretation of Raman spectra of disordered and amorphous carbon,” *Phys. Rev. B*, vol. 61, no. 20, pp. 14095–14107, May 2000.

[6] A. C. Ferrari and J. Robertson, “Raman spectroscopy of amorphous , nanostructured , diamond−like carbon , and nanodiamond,” *Philos. Trans. R. Soc. A*, vol. 362, no. September 2009, pp. 2477–2512, 2004.

[7] C. Pereira-Nabais, J. Światowska, A. Chagnes, A. Gohier, S. Zanna, A. Seyeux, P. Tran-Van, C.-S. Cojocaru, M. Cassir, and P. Marcus, “Insight into the Solid Electrolyte Interphase on Si Nanowires in Lithium-Ion Battery: Chemical and Morphological Modifications upon Cycling,” *J. Phys. Chem. C*, vol. 118, no. 6, pp. 2919–2928, Feb. 2014.

[8] C. Wang, A. J. Appleby, and F. E. Little, “Irreversible capacities of graphite anode for lithium-ion batteries,” *J. Electroanal. Chem.*, vol. 519, no. 1–2, pp. 9–17, Feb. 2002.

[9] G. G. Eshetu, S. Grugeon, G. Gachot, D. Mathiron, M. Armand, and S. Laruelle, “LiFSI vs. LiPF6 electrolytes in contact with lithiated graphite: Comparing thermal stabilities and identification of specific SEI-reinforcing additives,” *Electrochim. Acta*, vol. 102, pp. 133–141, Jul. 2013.

[10] S. H. Ng, J. Wang, D. Wexler, S. Y. Chew, and H. K. Liu, “Amorphous Carbon-Coated Silicon Nanocomposites: A Low-Temperature Synthesis via Spray Pyrolysis and Their Application as High-Capacity Anodes for Lithium-Ion Batteries,” *J. Phys. Chem. C*, vol. 111, no. 29, pp. 11131–11138, Jul. 2007.

[11] W.-R. Liu, J.-H. Wang, H.-C. Wu, D.-T. Shieh, M.-H. Yang, and N.-L. Wu, “Electrochemical Characterizations on Si and C-Coated Si Particle Electrodes for Lithium-Ion Batteries,” *J. Electrochem. Soc.*, vol. 152, no. 9, p. A1719, 2005.

[12] M. N. Obrovac and L. J. Krause, “Reversible Cycling of Crystalline Silicon Powder,” *J. Electrochem. Soc.*, vol. 154, no. 2, p. A103, 2007.

[13] K. Ogata, E. Salager, C. J. Kerr, a. E. Fraser, C. Ducati, a. J. Morris, S. Hofmann, and C. P. Grey, “Revealing lithium–silicide phase transformations in nano-structured silicon-based lithium ion batteries via in situ NMR spectroscopy,” *Nat. Commun.*, vol. 5, pp. 1–11, Feb. 2014.

[14] T. D. Hatchard and J. R. Dahn, “In Situ XRD and Electrochemical Study of the Reaction of Lithium with Amorphous Silicon,” *J. Electrochem. Soc.*, vol. 151, no. 6, p. A838, 2004.

[15] J. Graetz, C. C. Ahn, R. Yazami, and B. Fultz, “Highly Reversible Lithium Storage in Nanostructured Silicon,” *Electrochem. Solid-State Lett.*, vol. 6, no. 9, p. A194, 2003.

[16] F. M. Hassan, V. Chabot, A. R. Elsayed, X. Xiao, and Z. Chen, “Engineered si electrode nanoarchitecture: a scalable postfabrication treatment for the production of next-generation li-ion batteries.,” *Nano Lett.*, vol. 14, no. 1, pp. 277–83, Jan. 2014.

[17] Y. Nagao, H. Sakaguchi, H. Honda, T. Fukunaga, and T. Esaka, “Structural Analysis of Pure and Electrochemically Lithiated SiO Using Neutron Elastic Scattering,” *J. Electrochem. Soc.*, vol. 151, no. 10, p. A1572, Oct. 2004.

[18] C. Chou and G. S. Hwang, “Lithiation Behavior of Silicon-Rich Oxide (SiO1/3): A First-Principles Study,” *Chem. Mater.*, vol. 25, no. 17, pp. 3435–3440, 2013.

[19] P. R. Abel, Y.-M. Lin, H. Celio, A. Heller, and C. B. Mullins, “Improving the stability of nanostructured silicon thin film lithium-ion battery anodes through their controlled oxidation.,” *ACS Nano*, vol. 6, no. 3, pp. 2506–16, Mar. 2012.

[20] K. Kim, J.-H. Park, S.-G. Doo, and T. Kim, “Effect of oxidation on Li-ion secondary battery with non-stoichiometric silicon oxide (SiOx) nanoparticles generated in cold plasma,” *Thin Solid Films*, vol. 518, no. 22, pp. 6547–6549, Sep. 2010.

[21] H. Yoo, J.-I. Lee, H. Kim, J.-P. Lee, J. Cho, and S. Park, “Helical silicon/silicon oxide core-shell anodes grown onto the surface of bulk silicon.,” *Nano Lett.*, vol. 11, no. 10, pp. 4324–8, Oct. 2011.

[22] J. Yang, Y. Takeda, N. Imanishi, C. Capiglia, J. Y. Xie, and O. Yamamoto, “SiO x -based anodes for secondary lithium batteries,” *Solid State Ionics*, vol. 152–153, pp. 125–129, 2002.

[23] T. Buonassisi, M. a. Marcus, A. a. Istratov, M. Heuer, T. F. Ciszek, B. Lai, Z. Cai, and E. R. Weber, “Analysis of copper-rich precipitates in silicon: Chemical state, gettering, and impact on multicrystalline silicon solar cell material,” *J. Appl. Phys.*, vol. 97, no. 6, p. 063503, 2005.

[24] T. Heiser and A. Mesli, “Determination of the Copper Diffusion Coefficient in Silicon from Transient Ion-Drift,” *Appl. Phys. A*, vol. 57, no. 4, pp. 325–328, 1993.

[25] R. W. Olesinski and G. J. Abbaschian, “The Cu−Si (Copper-Silicon) system,” *Bull. Alloy Phase Diagrams*, vol. 7, no. 2, pp. 170–178, Apr. 1986.

[26] E. R. Weber, “Transition metals in silicon,” *Appl. Phys. A Solids Surfaces*, vol. 30, no. 1, pp. 1–22, Jan. 1983.

[27] M. E. Stournara, X. Xiao, Y. Qi, P. Johari, P. Lu, B. W. Sheldon, H. Gao, and V. B. Shenoy, “Li segregation induces structure and strength changes at the amorphous Si/Cu interface.,” *Nano Lett.*, vol. 13, no. 10, pp. 4759–68, Oct. 2013.

[28] V. A. Sethuraman, K. Kowolik, and V. Srinivasan, “Increased cycling efficiency and rate capability of copper-coated silicon anodes in lithium-ion batteries,” *J. Power Sources*, vol. 196, no. 1, pp. 393–398, Jan. 2011.

[29] M. Au, Y. He, Y. Zhao, H. Ghassemi, R. S. Yassar, B. Garcia-Diaz, and T. Adams, “Silicon and silicon–copper composite nanorods for anodes of Li-ion rechargeable batteries,” *J. Power Sources*, vol. 196, no. 22, pp. 9640–9647, Nov. 2011.

[30] Y. Seok Jung, A. S. Cavanagh, Y. Yan, S. M. George, and A. Manthiram, “Effects of Atomic Layer Deposition of Al2O3 on the Li[Li0.20Mn0.54Ni0.13Co0.13]O2 Cathode for Lithium-Ion Batteries,” *J. Electrochem. Soc.*, vol. 158, no. 12, p. A1298, Jan. 2011.

[31] K. Leung, Y. Qi, K. R. Zavadil, Y. S. Jung, A. C. Dillon, A. S. Cavanagh, S.-H. Lee, and S. M. George, “Using atomic layer deposition to hinder solvent decomposition in lithium ion batteries: first-principles modeling and experimental studies.,” *J. Am. Chem. Soc.*, vol. 133, no. 37, pp. 14741–54, Sep. 2011.

[32] I. A. Profatilova, C. Stock, A. Schmitz, S. Passerini, and M. Winter, “Enhanced thermal stability of a lithiated nano-silicon electrode by fluoroethylene carbonate and vinylene carbonate,” *J. Power Sources*, vol. 222, pp. 140–149, Jan. 2013.

[33] J. M. Martínez de la Hoz and P. B. Balbuena, “Reduction mechanisms of additives on Si anodes of Li-ion batteries.,” *Phys. Chem. Chem. Phys.*, vol. 16, no. 32, pp. 17091–8, Jul. 2014.

[34] Y.-M. Lin, K. C. Klavetter, P. R. Abel, N. C. Davy, J. L. Snider, A. Heller, and C. B. Mullins, “High performance silicon nanoparticle anode in fluoroethylene carbonate-based electrolyte for Li-ion batteries.,” *Chem. Commun. (Camb).*, vol. 48, no. 58, pp. 7268–70, Jul. 2012.

[35] L. Li, Z. Wu, S. Yuan, and X.-B. Zhang, “Advances and challenges for flexible energy storage and conversion devices and systems,” *Energy Environ. Sci.*, 2014.

[36] K. Wang, S. Luo, Y. Wu, X. He, F. Zhao, J. Wang, K. Jiang, and S. Fan, “Super-Aligned Carbon Nanotube Films as Current Collectors for Lightweight and Flexible Lithium Ion Batteries,” *Adv. Funct. Mater.*, vol. 23, no. 7, pp. 846–853, Feb. 2013.

[37] K. Fu, O. Yildiz, H. Bhanushali, Y. Wang, K. Stano, L. Xue, X. Zhang, and P. D. Bradford, “Aligned carbon nanotube-silicon sheets: a novel nano-architecture for flexible lithium ion battery electrodes,” *Adv. Mater.*, vol. 25, no. 36, pp. 5109–14, Sep. 2013.

[38] S. Brunauer, P. H. Emmett, and E. Teller, “Adsorption of Gases in Multimolecular Layers,” *J. Am. Chem. Soc.*, vol. 60, no. 2, pp. 309–319, Feb. 1938.

[39] K. S. W. Sing, “Reporting physisorption data for gas/solid systems with special reference to the determination of surface area and porosity (Recommendations 1984),” *Pure Appl. Chem.*, vol. 57, no. 4, pp. 603–619, Jan. 1985.

[40] L. Passoni, F. Ghods, P. Docampo, A. Abrusci, J. Martí-Rujas, M. Ghidelli, G. Divitini, C. Ducati, M. Binda, S. Guarnera, A. Li Bassi, C. S. Casari, H. J. Snaith, A. Petrozza, and F. Di Fonzo, “Hyperbranched quasi-1D nanostructures for solid-state dye-sensitized solar cells.,” *ACS Nano*, vol. 7, no. 11, pp. 10023–31, Nov. 2013.

[41] C. S. Casari and A. Li Bassi, “Pulsed Laser Deposition of Nanostructured Oxides : from Clusters to Functional Films,” in *Advances in Laser and Optics Research*, vol. 7, W. T. Arkin, Ed. Nova Science Publishers, Inc., 2012, pp. 65–100.

[42] Z. Li, W. Li, Y. Jiang, H. Cai, Y. Gong, and J. He, “Raman characterization of the structural evolution in amorphous and partially nanocrystalline hydrogenated silicon thin films prepared by PECVD,” *J. Raman Spectrosc.*, vol. 42, no. 3, pp. 415–421, Mar. 2011.

[43] T. Kawamura, S. Okada, and J. Yamaki, “Decomposition reaction of LiPF6-based electrolytes for lithium ion cells,” *J. Power Sources*, vol. 156, no. 2, pp. 547–554, Jun. 2006.

[44] S. F. Lux, I. T. Lucas, E. Pollak, S. Passerini, M. Winter, and R. Kostecki, “The mechanism of HF formation in LiPF6 based organic carbonate electrolytes,” *Electrochem. commun.*, vol. 14, no. 1, pp. 47–50, Jan. 2012.

[45] D. Aurbach, A. Zaban, Y. Ein-Eli, I. Weissman, O. Chusid, B. Markovsky, M. Levi, E. Levi, A. Schechter, and E. Granot, “Recent studies on the correlation between surface chemistry, morphology, three-dimensional structures and performance of Li and Li-C intercalation anodes in several important electrolyte systems,” *J. Power Sources*, vol. 68, no. 1, pp. 91–98, Sep. 1997.

[46] U. Heider, R. Oesten, and M. Jungnitz, “Challenge in manufacturing electrolyte solutions for lithium and lithium ion batteries quality control and minimizing contamination level,” *J. Power Sources*, vol. 81–82, pp. 119–122, Sep. 1999.

[47] U. Kasavajjula, C. Wang, and A. J. Appleby, “Nano- and bulk-silicon-based insertion anodes for lithium-ion secondary cells,” *J. Power Sources*, vol. 163, no. 2, pp. 1003–1039, Jan. 2007.

[48] X. Li, M. Gu, S. Hu, R. Kennard, P. Yan, X. Chen, C. Wang, M. J. Sailor, J. Zhang, and J. Liu, “Mesoporous silicon sponge as an anti-pulverization structure for high-performance lithium-ion battery anodes,” *Nat. Commun.*, vol. 5, no. May, pp. 1–7, 2014.

[49] M. Green, E. Fielder, B. Scrosati, M. Wachtler, and J. S. Moreno, “Structured Silicon Anodes for Lithium Battery Applications,” *Electrochem. Solid-State Lett.*, vol. 6, no. 5, p. A75, May 2003.

[50] G. Fagerlund, “Determination of specific surface by the BET method,” *Matériaux Constr.*, vol. 6, no. 3, pp. 239–245, May 1973.

Chapter 4

Silicon as Anode for Lithium-ion Batteries: feasibility on a large scale

This chapter is based on the work developed during a period of three months spent at the Project Competence-E group at Karlsruhe Institute of Technology (KIT), Karlsruhe, Germany (for an introductory video on the activity of the group, see [1]*).*

Silicon-graphite anodes have been prepared by slurry-based processes, commonly in use in industrial battery manufacturing. Feasibility studies have been conducted for partially substituting Si for graphite in a 1:1 ratio (of active material) while keeping the amount of additives (i.e. binder and carbon black as conducting agent) low enough to be meaningful for industrial-oriented applications (15% -20% of the total weight). Some technological issues had to be faced in processing and Si-graphite anodes were eventually fabricated. Electrochemical tests in full-cell configuration showed good cyclability with capacity fade in the order of 50% after 200 cycles. Feasibility of partial substitution of Si for graphite with a drop-in approach in current productive processes has been shown, but further optimization is surely needed for what concerns slurry composition and fabrication process parameters.

In parallel, anodes have been fabricated using a patented Si-based alloy as active material, in the frame of a broader collaboration/prject of the host research group with an industrial partner.

Despite the fact that this work is self-standing for what concerns techniques and aims, it is well integrated in the frame of this thesis. Continuity with PLD-films can be found in the scale that features the anodes developed at KIT, which are based on silicon nanoparticles and keep, also in their final structure, a nanostructured morphology. The nanometric size of the silicon particles plays a role in the interaction with other components and hence affects the rheology of the slurry and the final properties of the anodes.

In the last decade, an increase in the number of LIB manufacturers or of their productive capacity has been registered for applications in portable devices, stationary plants or automotive, thanks also to joint-ventures with the automotive industry[2]–[4]. Car manufacturers worldwide have launched new models of Electric Vehicles and/or Hybrid Electric Vehicles and the marked is rapidly developing in Europe, US and China, sustained also by governmental subsidies.

Currently, commercial anodes for large-scale production of LIBs are made of graphite, with well-established processes. Therefore, if on the one hand replacing graphite with silicon is appealing because of the higher reachable energy densities, on the other hand the substitution has to be “costless” from the point of view of the required technologies and processing steps. This leads the industrial-oriented research and development to a drop-in approach, where the change in raw materials does not impact on technologies and infrastructures. The film preparation, as for graphite-based anodes, needs then to be based on the coating of a slurry made by mixing dry materials, i.e. active material and conductive additives, with a viscous binder. After proper drying, the coated anodes are cut, coupled with cathode material and assembled into a cell with a suitable electrolyte.

While the work on anodes made by PLD, as described in the previous chapters, had the character of a lab-scale investigation to understand phenomena occurring in silicon-carbon nanostructured anodes and outlining innovative solutions, this work aims at going beyond the lab-scale to get closer to industrial application by adopting technologies and criteria typical of the large-scale production.

In this framework, a three-month project was carried out in collaboration with the group of Dr. Joerg Kaiser at the research laboratories of Project Competence-E of the Karlsruhe Institute of Technology (KIT) in Karlsruhe, Germany. The project was intended to be an explorative study of Silicon-based anodes with large-scale-oriented technologies and facilities and it focussed on the development of an anode made of pure-Si nanopowder. In addition, in collaboration with 3M, a multinational company, the author was involved in the activity of the host group, aimed at building anodes with a proprietary silicon-based alloy as active material.

Academic literature reports examples of silicon-carbon anodes from slurries, but little or no emphasis is put on the processes, that can in fact dramatically impact on the final electrochemical performances. This becomes even more crucial in moving from lab-scale cells to large-area cells, as required by industrial production. Upscaling to large areas harshens the constraints on the output of each single processing step and sets then, on its own, a technological challenge.

The scope of this work was to fabricate silicon-based anodes with a drop-in approach using tools and techniques usually adopted for graphitic anode production, with the final aim to realize large-area cells (pouch cells of nominal capacity 10 Ah and 20 Ah) that go beyond the lab-scale dimension of first investigation.

Since the study with pure-silicon nanopowder has the character of a preliminary investigation, lab-scale swagelok cells were realized (3mAh) to allow for rapid testing aimed at improving processes, in view of large-area fabrication. With the silicon-based proprietary alloy, instead, the work of the group had the aim to start from the results obtained by the partner company on small-scale cells to implement upscaling to large area pouch cells.

The experimental details and main results on graphite/silicon(nanoparticles) anodes are presented in the following.

4.1 Silicon nanopowder/Graphite as active material

The fabrication and testing of silicon-based anodes conducted by the author has involved all of the steps *from powder to cell*.

While graphitic anodes are fully consolidated in the industrial production, silicon anodes are still to be developed in an upscalable form, where the drawbacks introduced by the material itself (see Chapter 1) need to be overcome by suitable material design and process engineering. Several slurry-based silicon-carbon anodes are investigated in the literature; however, they are often not suitable for upscaling because their composition or the processes involved are far from requirements and constraints typical of the industrial fabrication[5].

This explorative study centred on nanosized silicon aims then at providing some first indications for the design of silicon-based anodes oriented to implementation in large-area cells with ready-to-upscale techniques.

The first concern of this study was to define criteria for the choice of a suitable slurry composition for the anodes to be tested, and, in particular, the total amount of active material (i.e. silicon+graphite), the relative amount of silicon (Si) and graphite(G) in the mix, the amount of carbon black to be added to favour electric conductivity and the choice and amount of a suitable binder means.

In parallel to this, process parameters in mixing, drying and calendering needed adjusting in order to obtain acceptable quality of the final anode material.

The short time available for this project did not allow for a complete optimization of the composition and processing steps, which were instead designed on the basis of meaningful assumptions based on the study of industrial (where available) and academic literature.

Composition

Active materials

Based on a previous work by Erk et al.[6], developed at the BELLA lab at KIT, silicon nanoparticles in the form of nanopowders (<50nm diameter) provided by Alpha Aesar were chosen as the active material for anode fabrication. The advantage of nanometric size of silicon particles is their intrinsic mechanical stability. As shown by Hu and co-workers[7], in fact, a threshold size of ~150nm exists for silicon particles, below which no crack propagation occurs during lithiation/delithiation cycles. The choice of commercially available particles with diameter below 50nm for this project meets then this requirement.

For what concerns graphite, a mix of two commercial particles (5÷10 µm size), mentioned as G1 and G2 in the following, was used in a fixed weight proportion, as from previous optimization.

For this explorative study, silicon was meant to partially substitute for graphite as active material and an initial weight ratio of 1:1 Si:G was chosen for the tests. Examples of anodes made of silicon particles in the literature report a wide variety of compositional Si:G ratios, ranging from 1:3 [8] to 7:3 [9] or even pure silicon[6], [10], so the choice of a 1:1 ratio falls in between this range.

Even more important, if industrial-oriented applications are sought, is the total amount of active material on the total weight of the dry components of the slurry. Binders and conductive additives add weight and volume, thus negatively affecting the value of energy density of the cell and should then be reduced to a minimum amount. According to Dahn [5], to be relevant for industrial applications, the dry electrode material should include 86-96% of active materials. Examples of silicon anodes in the literature often report an active material content far below this threshold, probably because those works, aiming at an exploration on basic materials on a lab-scale, make use of non-optimized processes and then require higher amounts of binder and conductive additives for acceptable processing.

For this work, that has the character of an explorative study, a constraint was set on the total amount of the active material on the dry slurry composition, chosen to not below 78%.

Another important factor to be kept into account is the silicon particle size. Little attention is dedicated to this feature, with literature reporting particles sizes from tens of nanometres to tens of microns, or even omitting to mention it. Particle dimension is crucial in determining the surface area of the silicon powder, which impacts on dry and wet processing first and on the final electrochemical behaviour of the complete anode later, especially in SEI-formation dynamics and hence on irreversible capacity losses. Smaller particles (nm) tend to form agglomerates of micrometric dimension, thus making dry mixing with other components difficult to be homogeneous. Moreover, the higher surface area could affect the interaction with the binder solvent, and then the ability of the binder to properly disperse and effectively build up a connecting network.

Binder

A binder is effective if it allows for an excellent long-term cycling behaviour of the Si-graphite-composite electrode during which a considerable amount of Si remains electrochemically active. This is only possible if electrode disintegration is prevented by an intense connection between the strongly swelling Si particles and the graphite matrix [8]. Moreover, the binder should provide good adhesion between the coated active film and the current collector (copper in this study).

The choice of the binder was led by a careful literary review. Graphitic anodes usually include a binder made of Polyvinylidene fluoride (PVdF) dissolved in N-methyl-2-pyrrolidone (NMP), which is inert towards lithium and electrolytes. PVdF-NMP, though, is not suitable to effectively accommodate the large volume expansion of silicon anodes in lithiation and only upon annealing can the performances be slightly increased[11], [12]. Moreover, NMP is toxic [13], [14] and water-based binders are increasingly being adopted as alternatives, such as those based on carboxymethyl cellulose (CMC), with or without the addition of styrene-butadiene rubber (SBR), or poly-acrylic acid (PAA), all of them requiring water as a solvent/dispersing phase[9], [10], [15].

CMC is a thickening means well known in many applications, such as food industry or non-food healthcare products. Since CMC is a stiff and brittle polymer, the addition of SBR is commonly meant to provide the binding network with higher flexibility, in order to face expansion and swelling of the electrodes in operation. Si electrodes using CMC binder show vastly improved cycling performance compared to the conventional PVdF[6], [9], [10]. The binding mechanisms, though, are still to be investigated in more details in order to conclude whether the addition of SBR be beneficial or not, as outlined by Li et al. [10].

The cycle life improvement when using PAA and CMC is attributed to the high values of the polymer elastic modulus [16] and the formation of a covalent chemical bonds between the functional groups of the polymers and the surface oxide of the Si particles [8], [17], [18].

Since PAA offers high concentration of functional groups and tuneable mechanical properties, it has been successfully used as a binder in Si-based anodes, with good stability over hundred cycles, as shown by Magasinski et al.[16]. The choice of PAA as highly performing binder in Si-based anodes has been confirmed also by the comparative work of Erk et al. [6].

We then chose to adopt LiPAA as a binding means for our work, for its being water-based and for the increased performances with respect to other binders in silicon-containing systems. LiPAA was made by neutralizing PAA with $LiOH{\cdot}H_2O$ in distilled water (not prepared by the author).

The effectiveness of the binder is related not only to its ability to prevent electrode disintegration, but also to the adhesion that it promotes between electrode coating and metallic foil used as current collector. No specific mechanical adhesion tests were done in this work, only simple observation of the response of coated dry electrodes to bending by hand.

The binder content was set to 11.5÷12.0%, basing this value on the existing literature (5-20% generally reported in works with PAA[16], [19], [20]) and adapting it during experimental processing. Too low binder content would turn into cracking and pulverization of the dry coating, while too high a content would add non-active weight, thus reducing the active material weight fraction, and possibly have a negative impact on the electrical conductivity of the anode, since most of the common binders are non-conductive.

Processing

The processing steps hereafter described are the result of a rough empirical optimization based on trial-and-error approach and led by the criteria learned from the host group's experience and valuable discussion.

The mixing step, both at a dry and a wet level, i.e. with binder, is critical for obtaining a homogeneous dispersion of all of the components of the slurry. Process parameters and tool design, such as, for example, the stirring rotational speed, the ratio between stirrer diameter and vessel diameter, the shape of the stirring head have high relevance at this stage, since they can determine whether agglomerates are effectively disintegrated and materials dispersed homogeneously. Agglomerates of the dimension of tens of micrometers can detrimentally affect the quality of the coating, both in terms of distributions of the different materials and of uniformity in thickness. Moreover, the presence of agglomerates reduces the film integrity because they are difficultly integrated in the binder network and then tend to easily detach from the film. Needless to say, agglomerates of such dimension alter the local composition of the film, hence its electrochemical and mechanical properties. To be homogeneous, compact and uniform, a coated film strongly depends on this initial processing step.

In the frame of the present work, we decided to use small amounts of Silicon for each processed batch, in the order of 2-8 g and each batch of slurry had an approximate volume of 20-40 ml. We opted for tools of reduced dimension, because the tools normally in use in the group were optimized for volumes as high as 200 ml or more. Therefore, mixing procedure was far from optimized.

The two kinds of graphite powders and carbon black were dry-mixed by hand and then mixed to some of the LiPAA, while Silicon powder was dispersed by hand in the rest of LiPAA. The two suspensions were first separately stirred in glass beakers by a mechanical overhead disc stirrer (rotational speed 300÷1000 rpm), and then put together to complete mixing. The disc stirrer was also moved, at fixed intervals, up and down along its axis, so to improve overall mixing.

During mixing, the viscosity of the slurry was adjusted by introduction of deionized water, that is, the LiPAA solvent, to ensure a uniform coating afterwards. Too viscous slurry would leave uncoated areas during doctor-blading, while too aqueous binder would result in inhomogeneous thickness due to the flow motion of the film on the copper sheet during handling.

Once the mixing was over, after about 2-3h, the slurry was evacuated under a vacuum bell while being slowly stirred by a magnet for around 10min, in order to remove as much as possible the residual gas introduced by stirring. Bubbles of residual gas would otherwise nucleate in the slurry during drying, introducing uncontrolled voids and brittleness in the film.

Right after evacuation, the slurry was coated on a copper sheet (10µm thick) by doctor-blade technique, by regulating the slit to 100µm. The coated sheets were then immediately dried in a vacuum oven at 130°C for 40min to let the binder solvent (i.e. water) evaporate.

Since, after coating, the composite electrodes are highly porous, they are typically calendered under high pressures in order to achieve uniform thickness, a high volume fraction of active material and a high coating volumetric capacity[5], [19], [21]. Before cutting, then, our coated copper sheets underwent calendering by means of a manual hydraulic press (applied load $6*10^4$N). As recently described by Du et al.([22] and references therein), besides increasing the electrode density, calendering generally leads to improved electrode cycling stability, coating adhesion and electrical conductivity. However, excessive pressure can turn into very low porosity of the electrode and blockage of the liquid-phase Li+ diffusion from the electrolyte to the electrode particle, thus resulting in high electrode impedance and reduced rate performance and reversible capacity. Therefore, a minimum electrode porosity must be maintained, with optimized porosities being about 10–40% by volume.

Cell type

Electrodes were then cut in discs of 12mm diameter by a punching machine, while discs of 11mm diameter were cut out of a sheet of commercial NMC on aluminium to be used as counterelectrodes. The difference in diameter between anode and cathode ensures that, despite any possible misalignment of the two electrodes during assembling, the active area of the cell is well known, being limited by the smaller of the two electrodes. Swagelok-type cells were then assembled in a dry room with fibre glass discs as separator and an electrolyte made of EC:DMC (1:1 w/w) with 3% wt. vinylene-carbonate (commercially available), which fluoroethylene-carbonate (FEC) was added to (10% v/v).

Half-cell configuration is often used for explorative studies in academic research, so to ideally analyse the behaviour of one single electrode. Nevertheless, we chose to work with full cells with the same cathode as used in final application, to avoid the mitigating effect of the litihum foil used as counterelectrode on the irreversible losses. When lithium foil is used as counterelectrode, it provides an ideally unlimited reservoir of lithium ions to the anode, hence mitigating the effect of irreversible losses of the available litihum due to the formation of the SEI layer or to the irreversible alloying with the active material (i.e. in cycling, not all of the lithium can be effectively extracted from the Li_xSi alloy).

After assembling, prior to start testing, the cells were left in rest for some hours.

Electrochemical testing

The performances of the cells were evaluated by an Arbin BT2000 electrochemical station.

Tests were performed under constant-current constant-voltage conditions (CCCV) between 3.0 V and 4.2 V cell voltage, at a current rate depending on the kind of test. First, the cells underwent a formation step at C/10 for the first charge/discharge cycle and C/2 for the following 6 cycles. Then, a long-life test followed where the cells were cycled under CCCV at C/2 for up to 200cycles. In some cases, before the long-life test, a C-rate test was performed by cycling the cells at increasing C rate for 15 cycles (C/10, C/5 and C/2 for 5 cycles each).

4.2 Results and discussion

Despite the many assumptions beneath the definition of a slurry composition and some experimental difficulties arisen in mixing[1], the realization of Si/C composite anodes was successful and allowed for building full operating cells.

The results of this explorative study are based on anodes made from three batches of slurry prepared with different composition, namely Si_02, Si_04 and Si_06 (details in table 4.1). The choice of the composition was driven by assumptions and by the first electrochemical results obtained, as discussed in the following.

---

[1] During mixing, the Si/graphite slurry looked visibly far from standard graphite slurries. Due probably to the different *philia* of Si and graphite with water (Si is hydrophilic while graphite is hydrophobic), the slurry tended to include much air during stirring, thus resulting in a foam-like mass. Excessive porosity would result in a coated film with poor mechanical stability, so the issue was alleviated by repeating the evacuation step several times, each immediately before every DrBlade coating.

Batch	Composition (% on dry)					
	Si	G1	G2	Tot act mat	Carbon Black	Binder (Li-PAA)
Si02	44	20	24	88	2	10
Si04	43	20	23	86	2	12
Si06	41	18	20	79	10	12

of the three batches of slurry, where the values are given as % of the total dry mass. The column in grey sums up the active material content in the slurry (= silicon+graphite)

In figure 4.1(a), charge/discharge curves of Si_02 are shown for the first 7 cycles. Initial capacity is lower than expected: calculations based on the active material load (0,00182g/cm^2) and theoretical capacity of the composite active material (1950mAh/g), the cell should provide a nominal capacity of ~4mAh, while only 2mAh were measured as charge capacity. 30% capacity (charge) was lost in the first cycle and the capacity retention after 7 cycles was ~65%.

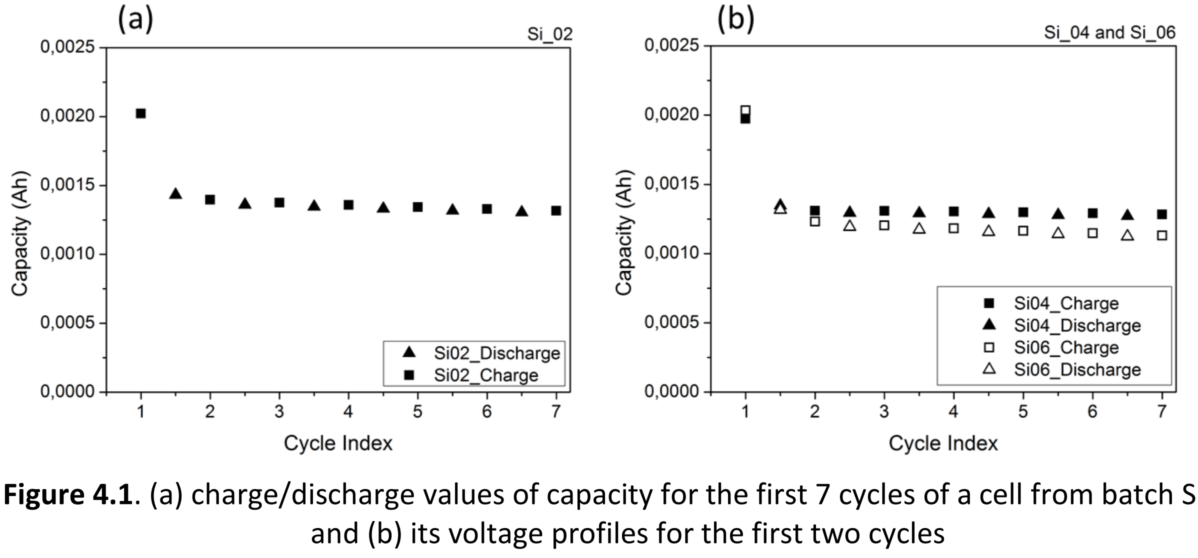

Figure 4.1. (a) charge/discharge values of capacity for the first 7 cycles of a cell from batch Si_02 and (b) its voltage profiles for the first two cycles

Besides the loss of active Li due to SEI formation on large surface area Si nanoparticles, one major reason for capacity losses during cycling was thought to be the mechanical brittleness of the coating. In anodes made with brittle films, fragments can easily detach either in calendering and cell assembly or in operation, due to mechanical stresses of volume expansion and shrinkage. Consequently, portions of active material are lost or remain inactive due to loss of electrical contact. Inactive material can also be responsible for an initial capacity lower than estimated (overestimation of the weight of active material), as well as the partial oxidation of Silicon particles (overestimation of the theoretical capacity of active material).

In order to improve the cohesion of the film, the binder content in slurries Si_04 and Si_06 was increased from 10% weight ratio on dry slurry components to 12%, as reported in table1. This would in principle improve also the adhesion to the current collector made of Al foil. In addition, the carbon black content was increased in Si_06 with respect to Si_04 to test its influence on the electrical conductivity of the anodes. In particular, insufficient electrical conductivity could negatively affect the capacity retention, because it would not allow for a fast enough kinetics of lithium insertion and extraction, thus preventing the anode from working at its full capacity.

With an increased binder content, the films obtained from batches Si_04 and Si_06 visibly appeared as less brittle. Figure 1(b) shows charge/discharge curves over 7 cycles of full cells where the anode is either Si_04 or Si_06.

Table 4.2 compares the value of capacity retention and initial capacity of the three cells with anodes from batch Si_02, Si_04 and Si_06 and shows that the increase in binder content is not as effective as expected in increasing capacity retention. While between Si_04 and Si_02 the capacity retention is improved by the addition of binder, this effect is not registered in comparing Si_06 and Si_02.

	Si02	**Si04**	**Si06**
Capacity retention% (charge)			
1st-2nd	69,3	66,5	60,6
7th-1st	65,3	65,0	55,7
7th-2nd	94,3	97,7	91,9
Target capacity (mAh)	4,01	3,92	4,48
Capacity% (reached /target)	50,4	50,3	45,3

Table 4.2. Data of capacity retention for the three kinds of cells. Capacity retention is calculated after 2 cycles (1^{st}-2^{nd}), 7 cycles (7^{th}-1^{st}) and between 7^{th} and 2^{nd} cycle to exclude the contribution from first-cycle irreversible losses, mostly due to SEI formation.

From data in figure 4.2, referred to long-life cycling after the formation step (cycles 30^{th} to 200^{th}), information on capacity retention (discharge) of the three kinds of cells can be drawn. After 200 cycles the capacity retention is 30% for Si_02, 29% for Si_04 and 27% for Si_06, confirming that the contribution of the binder content to the overall mechanical stability is not a factor that leads capacity retention.

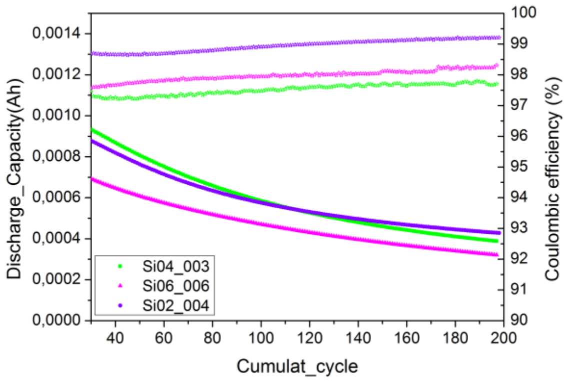

Figure 4.2. Long-life cycling at C/2: discharge capacity values of cells from slurries Si_02, Si_04 and Si_06 and their coulombic efficiency

From the previous analysis, three facts can be outlined:

(a) a difference exists between expected and actual initial capacity, where the calculation of the expected value is based on weight of the film, relative content of active material in the film and theoretical capacity of active materials (Si and C).

(b) the capacity retention after 200 cycles is ~30% for all the different cells. The increase in binder content does not improve this figure.

(c) an increase in the carbon black content does not improve capacity retention. This means that carbon black content, in the range of concentrations under analysis, is not a limiting factor for the anode performance and can therefore be set, in future tests, to the lowest tested value (2% w/w on total dry slurry weight) to minimize inactive material content. This does not imply, though, that electrical conductivity needs no further investigation. It has to be noted here that also the SiOx layer surrounding Si particles plays a role in the overall conductivity; however, its elimination would require Si particles to be pre-treated with hydrofluoric acid and that all successive fabrication steps be done under oxygen/moisture-free atmosphere. This would introduce too severe constraints and changes in the production processing and is therefore to be avoided to the scopes of this study.

For what concerns initial capacity and capacity retention (points (a) and (b)), their limitation is thought to be caused by unsatisfactory mechanical properties of the anode film, which can be influenced by several factors, attaining most likely to the details of the processing steps (e.g. effectiveness of mixing procedures, calendering).

The effect of the binder content has been discussed above and its amount has been increased when moving from Si_02 to Si_04/06. Indications that can be drawn for future tests, rather than on further increasing binder content in the slurry, rely on optimizing each single process step by separately testing the effects of different procedures on film cohesion, brittleness and homogeneity.

The importance of a mixing procedure that gives homogeneous films has been discussed in the introduction of this chapter and becomes relevant in observing SEM images, showing agglomerates in the coated anode films. Agglomerates alter the local properties of the film and constitute easily-detachable fragments, as clearly evidenced in figure 4.3(a), where a visible crater is left from a detached agglomerate. It is then necessary to optimize the mixing procedure in terms of: relative diameter of the stirrer and the vessel (this can help breaking agglomerates), rotational speed and time, shape of the stirrer (this can promote effective multi-directional mixing). Moreover, the order of addition of the different components of the slurry can affect mixing, due also to the different character (hydrophilic/hydrophobic) of the involved materials towards water (see also footnote 1).

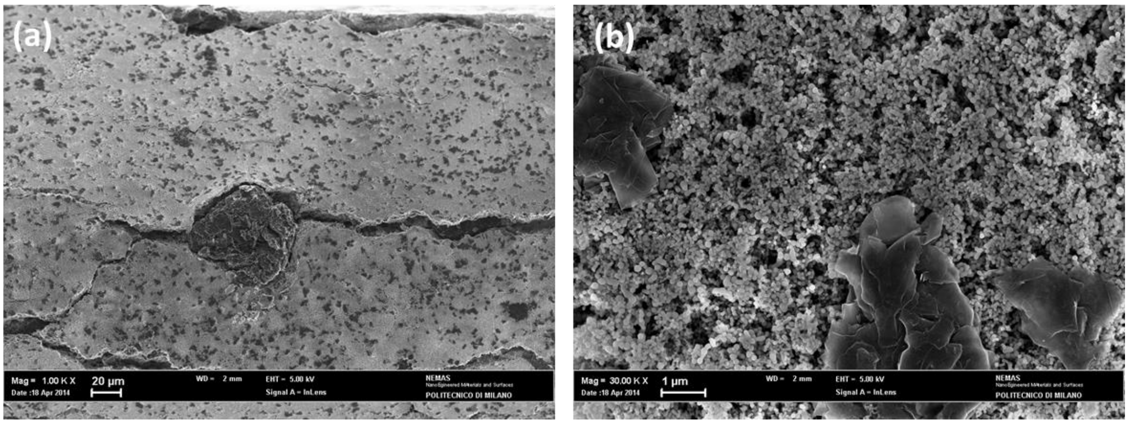

Figure 4.3. SEM micrographs in top-view of (a) an example of agglomerate of ~70µm diameter. (b) A zoomed view of Si_04 film, showing the different scale of Si and graphite particles.

Among process steps, calendering plays a crucial role for the final mechanical properties of the film. As described by Dahn and coworkers, too low a calendering pressure/ too short a time would turn ineffective in reducing the coating porosity, while excessive pressure would close all of the pores, making it impossible for the electrolyte to reach the whole anode, thus not exploiting the full anode capacity[5]. In addition, too high pressure may damage the particles, increasing a concentration of defects that may block diffusion of lithium into the active mass[21]. For future tests, then, it is suggested to thoroughly investigate and optimize the calendering procedure.

Other processing steps, such as drying of the coated films, can also be optimized, for fast drying at low temperature is desired from the industrial point of view, but the impact of time and temperature on the final coating needs to be studied.

4.3 Conclusions to Chapter 4

In conclusion, this work presents the first steps of a feasibility study for the realization of composite silicon/graphite anodes for lithium-ion batteries to be realized by a drop-in approach, i.e. by adopting the technologies and processes currently in use for graphite anodes.

Si/C slurries (1/1 w/w) were prepared with almost 80% w active material and LiPAA in water as a binder and used as anodes in swagelok test cells with NMC as a cathode. The cells showed the ability to successfully run for at least 200 cycles, although with noticeable capacity fade and an initial capacity lower than estimated.

Limitations in initial capacity and in capacity retention are probably due to morphological and mechanical properties of the coatings. To reduce brittleness, anodes with an increased amount of binder were tested and showed no improvement in capacity retention. SEM reveals the presence of agglomerates (~70µm) in the anode structure, which are thought to strongly contribute to capacity losses by enhancing fragmentation ad loss of electrical contact of some parts.

Future developments of this work should include optimization of the processing steps that most affect, at this stage, the mechanical properties of the film; in particular, mixing needs to be effective in avoiding formation of agglomerates and calendering should allow for a final residual porosity with minimized residual stresses. The two are not independent, since the variations in film thickness caused by the presence of agglomerates (~70µm on a film thickness of ~50µm) determine an irregular distribution of the calendering load, thus resulting in local over/under loading.

On the way to large-scale fabrication of Si/C slurry-based composite anodes, this first study aims at defining a starting point and outline a strategy for improvement.

References

[1] KIT Karlsruher Institut fuer Technologie, “Forschungsfabrik fuer Lithium-Ionen-Batterien,” 2014. [Online]. Available: http://www.youtube.com/watch?v=0Fhh2xhUerU.

[2] Reuters, “Samsung SDI to build electric car battery factory in China,” 2014. [Online]. Available: http://www.reuters.com/article/2014/01/23/us-samsung-sdi-idUSBREA0M03O20140123.

[3] Nissan, “The Compact Lithium-ion Battery,” 2014. [Online]. Available: http://www.nissan-global.com/EN/ENVIRONMENT/CAR/FUEL_BATTERY/DEVELOPMENT/LITHIUM_ION_BATTERY/.

[4] Wikipedia, “List of electric vehicle battery manufacturers.” [Online]. Available: http://en.wikipedia.org/wiki/List_of_electric_vehicle_battery_manufacturers .

[5] T. Marks, S. Trussler, A. J. Smith, D. Xiong, and J. R. Dahn, “A Guide to Li-Ion Coin-Cell Electrode Making for Academic Researchers,” *J. Electrochem. Soc.*, vol. 158, no. 1, p. A51, Jan. 2011.

[6] C. Erk, T. Brezesinski, H. Sommer, R. Schneider, and J. Janek, “Toward silicon anodes for next-generation lithium ion batteries: a comparative performance study of various polymer binders and silicon nanopowders.,” *ACS Appl. Mater. Interfaces*, vol. 5, no. 15, pp. 7299–307, Aug. 2013.

[7] X. H. Liu, L. Zhong, S. Huang, S. X. Mao, T. Zhu, and J. Y. Huang, “Size-dependent fracture of silicon nanoparticles during lithiation,” *ACS Nano*, vol. 6, no. 2, pp. 1522–31, Mar. 2012.

[8] N. S. Hochgatterer, M. R. Schweiger, S. Koller, P. R. Raimann, T. Wöhrle, C. Wurm, and M. Winter, “Silicon/Graphite Composite Electrodes for High-Capacity Anodes: Influence of Binder Chemistry on Cycling Stability,” *Electrochem. Solid-State Lett.*, vol. 11, no. 5, p. A76, 2008.

[9] W.-R. Liu, M.-H. Yang, H.-C. Wu, S. M. Chiao, and N.-L. Wu, “Enhanced Cycle Life of Si Anode for Li-Ion Batteries by Using Modified Elastomeric Binder,” *Electrochem. Solid-State Lett.*, vol. 8, no. 2, p. A100, 2005.

[10] J. Li, R. B. Lewis, and J. R. Dahn, “Sodium Carboxymethyl Cellulose,” *Electrochem. Solid-State Lett.*, vol. 10, no. 2, p. A17, 2007.

[11] J. Li, L. Christensen, M. N. Obrovac, K. C. Hewitt, and J. R. Dahn, “Effect of Heat Treatment on Si Electrodes Using Polyvinylidene Fluoride Binder,” *J. Electrochem. Soc.*, vol. 155, no. 3, p. A234, Mar. 2008.

[12] Y. Xu, G. Yin, Y. Ma, P. Zuo, and X. Cheng, “Simple annealing process for performance improvement of silicon anode based on polyvinylidene fluoride binder,” *J. Power Sources*, vol. 195, no. 7, pp. 2069–2073, Apr. 2010.

[13] K. LEE, “Toxicity of N-methyl-2-pyrrolidone (NMP): Teratogenic, subchronic, and two-year inhalation studies,” *Fundam. Appl. Toxicol.*, vol. 9, no. 2, pp. 222–235, Aug. 1987.

[14] SCCS (Scientific Committee on Consumer Safety), “Opinion on N-Methyl-2-pyrrolidone (NMP),” 2011.

[15] X. Feng, J. Yang, P. Gao, J. Wang, and Y. Nuli, “Facile approach to an advanced nanoporous silicon/carbon composite anode material for lithium ion batteries,” *RSC Adv.*, vol. 2, no. 13, p. 5701, Jun. 2012.

[16] A. Magasinski, B. Zdyrko, I. Kovalenko, B. Hertzberg, R. Burtovyy, C. F. Huebner, T. F. Fuller, I. Luzinov, and G. Yushin, “Toward efficient binders for Li-ion battery Si-based anodes: polyacrylic acid.,” *ACS Appl. Mater. Interfaces*, vol. 2, no. 11, pp. 3004–10, Nov. 2010.

[17] H. Wu, G. Yu, L. Pan, N. Liu, M. T. McDowell, Z. Bao, and Y. Cui, “Stable Li-ion battery anodes by in-situ polymerization of conducting hydrogel to conformally coat silicon nanoparticles.,” *Nat. Commun.*, vol. 4, p. 1943, Jan. 2013.

[18] B. Koo, H. Kim, Y. Cho, K. T. Lee, N.-S. Choi, and J. Cho, “A highly cross-linked polymeric binder for high-performance silicon negative electrodes in lithium ion batteries.,” *Angew. Chem. Int. Ed. Engl.*, vol. 51, no. 35, pp. 8762–7, Aug. 2012.

[19] Y.-S. Park, E.-S. Oh, and S.-M. Lee, “Effect of polymeric binder type on the thermal stability and tolerance to roll-pressing of spherical natural graphite anodes for Li-ion batteries,” *J. Power Sources*, vol. 248, pp. 1191–1196, Feb. 2014.

[20] Y. Liu, X. Guo, J. Li, Q. Lv, T. Ma, W. Zhu, and X. Qiu, “Improving coulombic efficiency by confinement of solid electrolyte interphase film in pores of silicon/carbon composite,” *J. Mater. Chem. A*, vol. 1, no. 45, p. 14075, 2013.

[21] J. . Gnanaraj, Y. S. Cohen, M. . Levi, and D. Aurbach, “The effect of pressure on the electroanalytical response of graphite anodes and LiCoO2 cathodes for Li-ion batteries,” *J. Electroanal. Chem.*, vol. 516, no. 1–2, pp. 89–102, Dec. 2001.

[22] Z. Du, R. a. Dunlap, and M. N. Obrovac, “High Energy Density Calendered Si Alloy/Graphite Anodes,” *J. Electrochem. Soc.*, vol. 161, no. 10, pp. A1698–A1705, Jul. 2014.

Chapter 5
Other applications for Silicon nanostructures: control of thermal conductivity

Thermoelectric materials can convert heat directly into electricity and increase energy efficiency of other devices if heat, otherwise wasted is used. During the past years, nanostructured silicon has been investigated as a thermoelectric material and nanostructured porous Si, in particular, has shown its promises because of the possibility to design it so as to maintain an effective electrical transport while significantly decrease its thermal conductivity.

The Si nanostructures presented in Chapter 2 showed characteristics and properties potentially interesting for the exploitation in the field of thermoelectric materials. The work here described deals with the fabrication and characterization of nanostructured hierarchical silicon porous films produced by PLD and the characterization of their thermal conductivity. Controlling the porosity provides a means to reduce the thermal conductivity with respect to the bulk material, as evidenced by the results obtained in the temperature range 300K to 370K with a differential 3ω measurement setup, in collaboration with the Interdisziplinares Zentrum fuer Materialwissenschaften and the Zentrum fuer Innovationskompetenz SiLi-nano of the Martin-Luther-Universitaet Halle-Wittenberg in Halle, Germany.

5.1 Thermal conductivity in thermoelectric materials

Thermoelectric materials can be used to directly convert heat to electricity, through the Seebeck effect, or for cooling or refrigeration through the converse Peltier effect. The efficiency for heat to electrical power conversion with a thermoelectric generator depends on the absolute process temperatures and temperature differences, as well as on the properties of the thermoelectric materials, i.e. the electrical conductivity σ, the Seebeck coefficient S and the thermal conductivity κ. These properties define a dimensionless figure of merit ZT, which needs to be maximized

$$ZT = \sigma S^2 T/\kappa ,$$

where T is the average absolute temperature of the hot and cold sides[1]. Therefore, as expressed by ZT, a good thermoelectric material has ideally a high electrical conductivity, a large Seebeck coefficient, because the current is driven by the voltage developed due to the Seebeck effect, and a low thermal conductivity to minimize the heat flow that tries to level the external temperature gradient through the material. In research, this has turned into engineering materials that are 'phonon-glass electron-crystal'.

Optimizing ZT requires a compromise between high S, σ and low k and the dependence of these properties on charge carrier concentration n cannot be neglected. A high charge carrier concentration favours a high electrical conductivity, since the electrical conductivity is given by $= en\mu$, where e is the elementary charge and μ the mobility of the charge carriers. On the other hand, the thermal conductivity should be as low as possible, but the electrical and the thermal conductivity are coupled through the electronic contribution to the thermal conductivity, which increases by increasing n. The total thermal conductivity is the sum of the lattice thermal conductivity (heat conduction by phonons) k_l and the thermal conductivity due to the charge carriers k_e. Given that the electronic thermal conductivity is related to the electrical conductivity by the Wiedemann-Franz law [2]: $k_e = L\sigma T = en\mu LT$ (where L is the Lorenz factor), the two quantities are not independent.

It is clear then that engineering thermoelectric materials deals with the limitations given by the interdependency of electrical and thermal transport. Several concepts have been proposed to overcome this limit and create novel thermoelectric materials. The most successful is to decouple heat and charge transport by nanostructuring[3]–[5]. This is meant to reduce the k_l contribution to the thermal conductivity without affecting the electrical properties of the materials and thereby to enhance the overall thermoelectric figure of merit. Indeed, a large majority of the increase in the figure of merit, ZT, of nanostructured thermoelectrics has been facilitated through a decreased k_l [4].

One of the main concepts that have been proposed to reduce the lattice thermal conductivity relies on the introduction of scattering interfaces at a length scale between typical electron and phonon mean free paths, thus disrupting heat but not charge transport.

Unlike its bulk form, nanostructured and nanoporous silicon may thus represent effective thermoelectric materials for low-cost applications due to their high electric conductivity as well as the non-periodic arrangement of nanoporous inclusions which cause a strong reduction of the thermal conductivity by phonon scattering and trapping[6], [7]. Moreover, the power factor, i.e. the product σS^2, may be increased by means of doping.

Besides efficiency, other important criteria for the applicability of thermoelectric materials are cost, availability, and processability. For many applications it might be better to find/design an inexpensive material with ZT around unity than finding an expensive material with record ZT. Bi2Te3 is the most widely used thermoelectric material and its alloying with Bi2Te3 and Sb2Te3 can further reduce the thermal conductivity. These alloys have peak ZT around unity at room temperature, while in the temperature range from 500–900K materials containing group-IV elements are commonly used for energy harvesting, such as PbTe, GeTe, or alloys like LAST (lead-antimony-silver-telluride) or TAGS (tellurium-antimony-germanium-silver) [8], [9]. In addition, SiGe alloys find also application in waste-heat recovery in vehicles [10] and in the powering of space-flight missions [11]. Many of these state-of-the art materials present clear disadvantages: Ge is expensive, Pb is poisonous and Te is one of the rarest stable accessible elements with a high price which is expected to further increase [12], [13]. It is therefore important to identify materials that are abundant, inexpensive and easily processable. Since silicon has great advantages in terms of abundance and processability compared to Bi2Te3, nanostructured Si is a high potential candidate for future thermoelectric applications[14].

Porous silicon is usually obtained by electrochemical etching of a silicon wafer in hydrofluoric acid[15], [16], while manifold techniques are known for the deposition of compact and porous silicon thin films, *e.g.* chemical vapor deposition (CVD) by silane precursor (SiH_4), molecular beam epitaxy or sputtering, which generally require elevated process temperatures. With respect to other deposition methods (e.g. CVD) that require high processing temperatures, the PLD technique that we adopted in this thesis can be advantageous, for we deposit at room temperature. Moreover, it does not require any harmful substance such as hydrofluoric acid or silane.

The porous silicon nanostructures that we fabricated by PLD as described in Chapter 2 could potentially show a lower thermal conductivity with respect to bulk silicon due to their morphology, i.e. nanostructuring and introduction of voids. Therefore, we set up a collaboration with the group of prof. Leipner at the Martin-Luther-Universitaet Halle-Wittenberg in Halle, Germany, in order to characterize the thermal conductivity k_l of some selected films grown by PLD. In addition, the same group and other groups in Halle (*Max Planck Institute of Microstructure Physics)* and Ilmenau (*Institut fuer Physik and Institut fuer Mikro- und Nanotechnologien, TU Ilmenau*) further characterized the films by means of microscopy and spectroscopy techniques and the results are discussed in a paper in preparation (*"Thin Si-based films for thermoelectric applications grown by pulsed laser deposition"*, K. Bertram, M. Trutschel, E. Biserni, A. Li Bassi, P. Bruno, E. Pippel, G. Eichapfel, M. Himmerlich, S. Krischok, H. S. Leipner, and M. Schade). Rather than providing conclusive indications on a novel thermoelectric material, the work here presented is intended to explore the potentiality of PLD-nanostructuring in tailoring one film property, namely k_l. We are aware that on the way to a real thermoelectric application, not only a reduction of k_l , but also high σ and S are necessary. The investigation of these properties, though, is beyond the scopes of this study.

5.2 PLD nanostructuring as a means to control thermal conductivity

We fabricated then two silicon films in different morphologies by means of room-temperature PLD and our collaborators at the *Interdisziplinares Zentrum fuer Materialwissenschaften* of the *Martin-Luther-Universitaet Halle-Wittenberg* in Halle, Germany, characterized their thermal conductivity by the 3ω method. In addition, thanks also to the support of the *Max Planck Institute of Microstructure Physics* and the *Institut fuer Physik and Institut fuer Mikro- und Nanotechnologien, TU Ilmenau*, they proceeded in characterizing the film composition, morphology and structure by suitable techniques.

As described in Chapter 2, the approach for growing films with desired morphology was to adjust the background gas pressure during pulsed laser deposition, so that cluster nucleation and growth could be to some extent controlled and hence the film porosity. For this study on the thermal conductivity, two target morphologies were chosen from those already explored and described in Chapter2, the one more compact induced at lower pressure (sample named Film5Pa) and the other one more porous (sample named Film40Pa) with columnar mesostructure, as shown in Figure 5.1. In the former, the disorder introduced by granular nanostructure is meant to scatter phonons while keeping a continuous morphology which is in principle beneficial for electronic transport; in the latter instead, the reduction of thermal conductivity is achieved by introducing a certain degree of porosity; within the range of explored porous structures described in Chapter2, the choice fell on the one grown at 40Pa as a trade-off between the need for porosity, required to reduce k, and the need for continuity and compactness to avoid negative effects on the electronic transport.

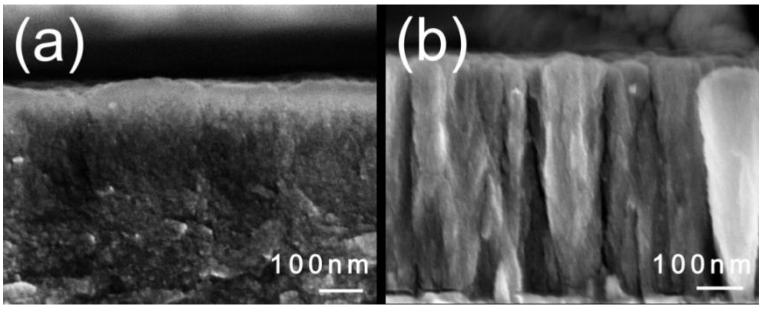

Figure 5.1 SEM micrograph of (a) Film5Pa and (b) Film40Pa

In details, we have grown Si films by ablating a translated and rotated silicon target (monocrystalline CZ, n^+-doped <100> wafer) with a KrF laser beam (λ=248 nm, pulse energy 400mJ, pulse duration 20 ns, repetition rate 20Hz, fluence 5 J/cm2). The substrates for deposition were cut out of a Si wafer (monocrystalline <100>) and placed at a distance of 50mm from the target. After reaching base vacuum of 3×10^{-3} Pa, Ar:H_2 gas (H2 <3 vol.%) was continuously fluxed as background processing gas and its pressure set to either 5Pa (Film5Pa) or 40Pa (Film40Pa) in order to induce the controlled growth of thin silicon films with different porosity. The addition of H_2 to Ar gas is aimed to reduce the degree of in-situ oxidation of silicon films during deposition by means of H_2 passivation, as described in Chapter 2. After deposition and during characterization steps, the samples were handled and stored in air.

A first rough characterization of the morphology and porosity of the samples was obtained by Scanning Electron Microscopy (SEM), which evidenced a compact nano-granular structure for Film5Pa and a nanoporous columnar one for Film40Pa.

In Chapter 2 we have presented the transmission electron microscopy (TEM) investigations in algae-like films grown by PLD at 100Pa. The scope of that investigation was to have a clear insight in the film nanostructure and to reveal and thorough characterize the presence of nanocrystalline phases in the film. In the films here analysed, instead, no crystalline phase is expected based on Raman spectroscopy (see Chapter 2); however, TEM has been performed in order to image the film nanostructure in terms of voids and thus extend the investigation of Chapter 2 to films grown at lower pressures. TEM was carried out using a JEM 4010 for bright-field imaging (BF-TEM) and diffraction patterning as well as a FEI TITAN for dark-field imaging (DF-STEM), operated at acceleration voltages of 400 kV or 300 kV, respectively. In addition, electron energy-loss spectroscopy (EELS) was performed inside the FEI TITAN to obtain information on the composition of deposited films.

High-resolution TEM and electron diffraction patterns evidence, as expected, an amorphous structure in both Film5Pa and Film40Pa. The comparison between BF-TEM and DF-STEM images in Figure 5.2 reveals density fluctuations attributed to either voids or caverns filled with molecules having a smaller atomic number than silicon.

As an additional analytical technique, EELS has been applied in order to achieve information about the local composition of the thin silicon films. Film5Pa shows silicon L23-edges typical of amorphous silicon (a-Si), while the spectrum of Film40Pa exhibits also the features of substoichiometric silicon oxides[17]. Partial oxidation in Film40Pa is also confirmed by X-ray photoelectron spectroscopy (XPS) analysis in a near-surface volume (up to 10nm).

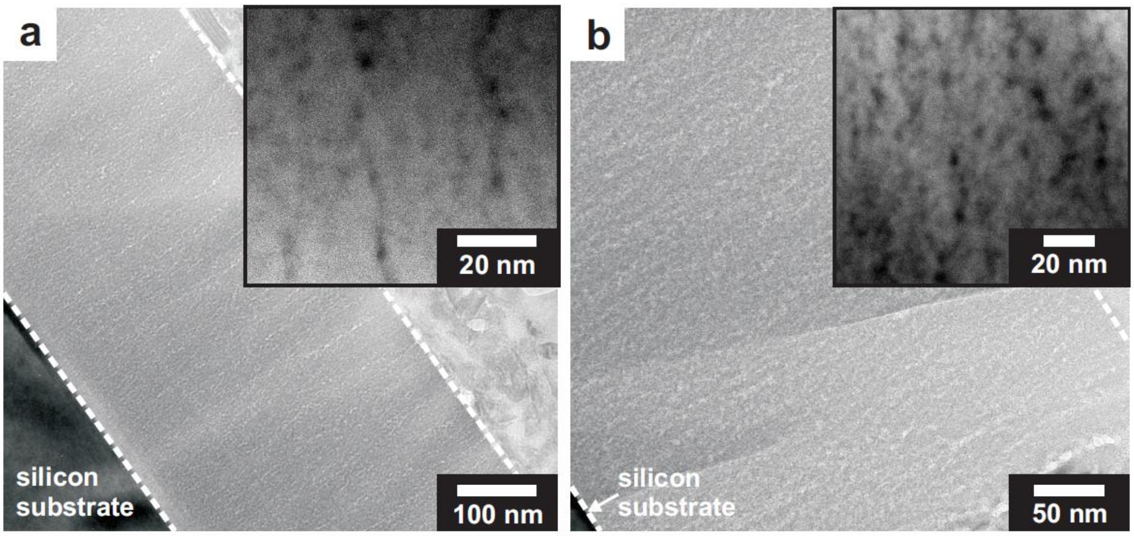

Figure 5.2[1]. BF-TEM images of Film5Pa (a) and Film40Pa (b). The silicon substrate is visible in the left lower part in each image. Additionally, DF-STEM images of each sample are presented as insets in order to point out the density fluctuations inside the thin films.

A differential 3ω measurement technique[18] was used to characterize the thermal conductivity of both thin films in comparison with a reference sample consisting only of the substrate (silicon wafer). For the 3ω measurements, an aluminium oxide layer of 100 nm was grown firstly on each sample by atomic layer deposition in order to prevent electric short cuts. Afterwards, a bolometer stripe with related contact pads composed of 10 nm Cr as adhesion agent and 90 nm Au was deposited by electron beam evaporation and photolithography.

The bolometer stripes were connected to the measurement setup with silver wires, each fixed on the contact pads by conductive silver. The deviation of the width between the bolometer stripes on the thin film and the reference was less than 3%. Since the width of the bolometer stripes is large compared to the thickness of the thin films and the thermal conductivity of the substrate is large, the heat transport through the thin silicon film can be assumed one-dimensional. The thin film thus acts as a thermal resistor and causes an increase of the temperature oscillations inside the sample. As a consequence, the difference ΔT_f between the temperature oscillations of the reference sample ΔT_{ref} and the sample with the thin film ΔT_{tf} is attributed to the thin film itself[18]:

---

[1] Figure 2 and Figure 3 in this chapter are courtesy of Dr. Martin Schade and Prof. Hartmut Leipner of the Martin-Luther-Universitaet Halle-Wittenberg in Halle, Germany.

$$\Delta T_f = \Delta T_{tf} - \Delta T_{ref} = P_l/l * \frac{t_f}{k_f 2b}$$

where P/l is the normalized heating power per unit length (P_l) applied to the bolometer stripe, $2b$ the width of the bolometer stripe, t_f the film thickness and k_f the thermal conductivity of the thin silicon film. Hence, transforming the equation above enables to obtain a value for the thermal conductivity k_f by using an averaged width of the bolometer stripes $2ba = (2b_{ref} + 2b_{film})/2$.

The calculated thermal conductivities of both films are presented together in Figure 5.3.

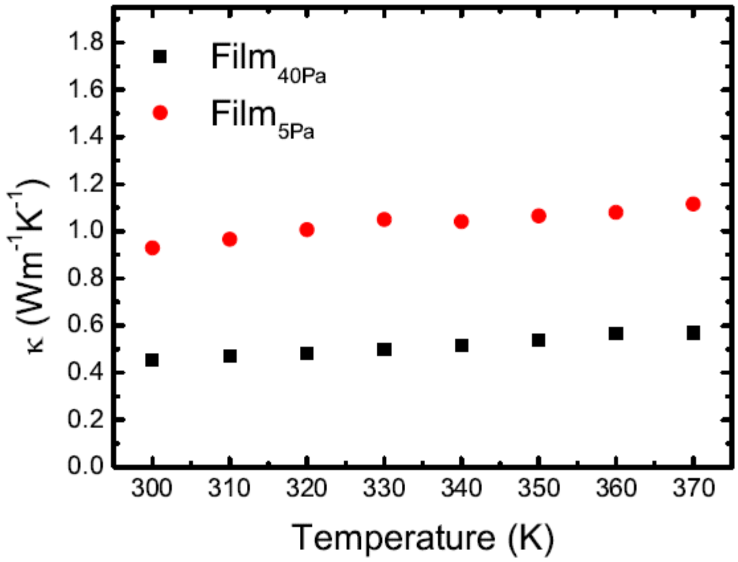

Figure 5.3. Thermal conductivity of both silicon thin films in the temperature range 300K to 370K. Both thin silicon films exhibit a reduced thermal conductivity compared to bulk silicon (149 W m^{-1} K^{-1}).

Focusing onto room temperature, the thermal conductivity of Film5Pa, made of amorphous Si, $k_{Film5Pa}$ =0.93 Wm^{-1}K^{-1} is distinctly smaller than that found for sputtered films[19], [20]. Interestingly, Film40Pa exhibits a $k_{Film40pa}$ = 0.46Wm^{-1}K^{-1}, that is two times smaller than that of common SiO$_2$ thin films[18], [21] or thin SiO$_x$ films fabricated by plasma enhanced CVD[22]. These values of k have been found using a heating power for the 3ω measurements of P_l =80 Wm^{-1} and confirmed also with P_l =2.8 Wm^{-1}.

One explanation for such a low thermal conductivity can be related to the low film thickness, which could be responsible for blocking the phonon modes with mean free paths larger than that of our films (around 400nm). However, this cannot be the only reason for the reduced k values found, since larger k values have been found for comparable films, exhibiting no noteworthy changes in k by exceeding 250 nm film thickness[23]. In addition, it has been shown that influences on k cannot be expected for film thickness higher than approximately 250 nm[24] and therefore the origin of phonon scattering and the resulting low thermal conductivity have to be caused by the density variations inside the films.

5.3 Conclusions to Chapter 5

In conclusion, we have investigated the possibility of tailoring thermal conductivity of nanostructured silicon films grown by PLD. The study shows that, by nanostructuring during growth, we can obtain a notable reduction in thermal conductivity of such silicon films, as indicated by the thermal characterization performed. As from the structural and compositional characterization, we suggest that the reduced thermal conductivity of the thin films is caused by two main reasons, i.e. the partial oxidation, more pronounced in Film40Pa, and the fluctuations in density (due to porosity in Film40Pa) that feature both films.

Irrespective of the exact physical mechanism causing the reduced thermal conductivity, such thin silicon films are promising candidates to become low-cost thermoelectric materials. Nevertheless, electrical conductivity and Seebeck coefficient, not measured here, cannot be neglected on the way to application. In particular, for what concerns the electrical conductivity, which is suspected to be negatively impacted by oxidation, two strategies can be applied for improvement. The one is to reduce the degree of ex-situ oxidation of the films by handling them in controlled atmosphere[25], [26], contrary to what has been done here. The other one is to increase the number of free carriers by introducing the right amount of a suitable dopant during PLD fabrication; this can be done by suitably designing a composite target or by co-deposition from two targets of different materials[27]–[30], with good control of the final stoichiometry[31], and is suitable both for p and n type doping.

Perspective work should focus on the parallel improvement of thermal and electrical conductivity by materials designing and process optimization and on the measurement of the seebeck coefficient. Thanks to its versatility, PLD appears then to be a promising technique.

References

[1] H. J. Goldsmid, *Introduction to Thermoelectricity*, XVI. Springer, 2010, p. 242.

[2] R. Franz and G. Wiedemann, “Ueber die Wärme-Leitungsfähigkeit der Metalle,” *Ann. der Phys. und Chemie*, vol. 165, no. 8, pp. 497–531, 1853.

[3] M. S. Dresselhaus, G. Chen, M. Y. Tang, R. G. Yang, H. Lee, D. Z. Wang, Z. F. Ren, J.-P. Fleurial, and P. Gogna, “New Directions for Low-Dimensional Thermoelectric Materials,” *Adv. Mater.*, vol. 19, no. 8, pp. 1043–1053, Apr. 2007.

[4] P. Pichanusakorn and P. Bandaru, “Nanostructured thermoelectrics,” *Mater. Sci. Eng. R Reports*, vol. 67, no. 2–4, pp. 19–63, Jan. 2010.

[5] J. R. Szczech, J. M. Higgins, and S. Jin, “Enhancement of the thermoelectric properties in nanoscale and nanostructured materials,” *J. Mater. Chem.*, vol. 21, no. 12, p. 4037, Mar. 2011.

[6] M. Maldovan, “Narrow Low-Frequency Spectrum and Heat Management by Thermocrystals,” *Phys. Rev. Lett.*, vol. 110, no. 2, p. 025902, Jan. 2013.

[7] W. Kim, J. Zide, A. Gossard, D. Klenov, S. Stemmer, A. Shakouri, and A. Majumdar, “Thermal Conductivity Reduction and Thermoelectric Figure of Merit Increase by Embedding Nanoparticles in Crystalline Semiconductors,” *Phys. Rev. Lett.*, vol. 96, no. 4, p. 045901, Feb. 2006.

[8] M. S. El-Genk and H. H. Saber, “Performance analysis of cascaded thermoelectric converters for advanced radioisotope power systems,” *Energy Convers. Manag.*, vol. 46, no. 7–8, pp. 1083–1105, May 2005.

[9] S. H. Yang, T. J. Zhu, T. Sun, J. He, S. N. Zhang, and X. B. Zhao, “Nanostructures in high-performance (GeTe)(x)(AgSbTe(2))(100-x) thermoelectric materials.,” *Nanotechnology*, vol. 19, no. 24, p. 245707, Jun. 2008.

[10] K. Ikoma, M. Munekiyo, K. Furuya, M. Kobayashi, T. Izumi, and K. Shinohara, “Thermoelectric module and generator for gasoline engine vehicles,” in *Seventeenth International Conference on Thermoelectrics. Proceedings ICT98 (Cat. No.98TH8365)*, 1998, pp. 464–467.

[11] D. M. Rowe, *Thermoelectrics Handbook: Macro to Nano*. CRC Press, 2005, p. 1008.

[12] S. K. Bux, R. G. Blair, P. K. Gogna, H. Lee, G. Chen, M. S. Dresselhaus, R. B. Kaner, and J.-P. Fleurial, “Nanostructured Bulk Silicon as an Effective Thermoelectric Material,” *Adv. Funct. Mater.*, vol. 19, no. 15, pp. 2445–2452, Aug. 2009.

[13] K. Zweibel, “Engineering. The impact of tellurium supply on cadmium telluride photovoltaics.,” *Science*, vol. 328, no. 5979, pp. 699–701, May 2010.

[14] N. Yang, G. Zhang, and B. Li, “Ultralow thermal conductivity of isotope-doped silicon nanowires,” *Nano Lett.*, vol. 8, no. 1, pp. 276–80, Jan. 2008.

[15] J. de Boor, D. S. Kim, X. Ao, D. Hagen, a. Cojocaru, H. Föll, and V. Schmidt, “Temperature and structure size dependence of the thermal conductivity of porous silicon,” *EPL (Europhysics Lett.*, vol. 96, no. 1, p. 16001, Oct. 2011.

[16] J. de Boor, D. S. Kim, X. Ao, M. Becker, N. F. Hinsche, I. Mertig, P. Zahn, and V. Schmidt, “Thermoelectric properties of porous silicon,” *Appl. Phys. A*, vol. 107, no. 4, pp. 789–794, Mar. 2012.

[17] M. Schade, N. Geyer, B. Fuhrmann, F. Heyroth, and H. S. Leipner, “High-resolution analytical electron microscopy of catalytically etched silicon nanowires,” *Appl. Phys. A*, vol. 95, no. 2, pp. 325–327, Jan. 2009.

[18] J. H. Kim, A. Feldman, and D. Novotny, “Application of the three omega thermal conductivity measurement method to a film on a substrate of finite thickness,” *J. Appl. Phys.*, vol. 86, no. 7, p. 3959, Oct. 1999.

[19] S.-J. Moon and J. H. Choi, “Estimation of Thermal Conductivity of Amorphous Silicon Thin Films from the Optical Reflectivity Measurement,” *J. Nanosci. Nanotechnol.*, vol. 13, no. 9, pp. 6362–6366, Sep. 2013.

[20] D. Cahill, M. Katiyar, and J. Abelson, “Thermal conductivity of a-Si:H thin films,” *Phys. Rev. B*, vol. 50, no. 9, pp. 6077–6081, Sep. 1994.

[21] T. Yamane, N. Nagai, S. Katayama, and M. Todoki, “Measurement of thermal conductivity of silicon dioxide thin films using a 3ω method,” *J. Appl. Phys.*, vol. 91, no. 12, p. 9772, 2002.

[22] A. Irace and P. M. Sarro, “Measurement of thermal conductivity and diffusivity of single and multilayer membranes,” *Sensors Actuators A Phys.*, vol. 76, no. 1–3, pp. 323–328, Aug. 1999.

[23] T. Zhan, Y. Xu, M. Goto, Y. Tanaka, R. Kato, M. Sasaki, and Y. Kagawa, “Phonons with long mean free paths in a-Si and a-Ge,” *Appl. Phys. Lett.*, vol. 104, no. 7, p. 071911, Feb. 2014.

[24] M. E. Siemens, Q. Li, R. Yang, K. A. Nelson, E. H. Anderson, M. M. Murnane, and H. C. Kapteyn, “Quasi-ballistic thermal transport from nanoscale interfaces observed using ultrafast coherent soft X-ray beams.,” *Nat. Mater.*, vol. 9, no. 1, pp. 26–30, Jan. 2010.

[25] K. Matsumoto, M. Inada, I. Umezu, and A. Sugimura, “Correlation between Natural Oxidation Process and Photoluminescence Properties of Hydrogenated Si Nanocrystallites Prepared by Pulsed Laser Ablation,” *Jpn. J. Appl. Phys.*, vol. 44, no. 12, pp. 8742–8746, Dec. 2005.

[26] I. Umezu, K. Matsumoto, M. Inada, T. Makino, and A. Sugimura, “Correlation between surface oxide and photoluminescence properties of Si nanoparticles prepared by pulsed laser ablation,” *Appl. Phys. A*, vol. 79, no. 4–6, Jul. 2004.

[27] I. Hanyecz, J. Budai, A. Oszkó, E. Szilágyi, and Z. Tóth, “Room temperature pulsed laser deposition of Si x C thin films in different compositions,” *Appl. Phys. A*, vol. 100, no. 4, pp. 1115–1121, May 2010.

[28] I. Umezu, T. Yamaguchi, K. Kohno, M. Inada, and A. Sugimura, “Preparation of SiN x film by pulsed laser ablation in nitrogen gas ambient,” *Appl. Surf. Sci.*, vol. 198, pp. 376–378, 2002.

[29] B. Eisenhawer, D. Zhang, R. Clavel, a Berger, J. Michler, and S. Christiansen, “Growth of doped silicon nanowires by pulsed laser deposition and their analysis by electron beam induced current imaging.,” *Nanotechnology*, vol. 22, no. 7, p. 075706, Feb. 2011.

[30] D. H. Lowndes, D. B. Geohegan, A. A. Puretzky, and D. P. Norton, “Synthesis of Novel Thin-Film Materials by Pulsed Laser Deposition,” *Science (80-.).*, vol. 273, no. 5277, pp. 898–903, 1996.

[31] J. Schou, “Physical aspects of the pulsed laser deposition technique: The stoichiometric transfer of material from target to film,” *Appl. Surf. Sci.*, vol. 255, no. 10, pp. 5191–5198, Mar. 2009.

Conclusions and perspective work

The focus of the work reported in this dissertation is the synthesis and characterization of silicon nanostructured thin films and their engineering to make them suitable for specific energy applications in the fields of energy production and storage.

The study, which is mainly experimental, has been given a strongly applicative cut and developed around two parallel concerns. On the one hand, understanding the properties of the silicon nanostructured material allows for their tailoring by suitable processing, as described in Chapter 2. On the other hand, the synthesis heads for exploitation in innovative devices. The approach is based on the fabrication of tailored silicon nanostructures by Pulsed Laser Deposition (PLD), their characterization by suitable microscopic and spectroscopic techniques and the optimization of their functional properties for the target application. In particular, the main applicative energy field explored is that of silicon anodes for lithium-ion batteries, and the related activity is summarized in Chapters 3 and 4**.** In addition, good confidence with the fabrication process opened the way for explorative studies on the properties of the material and the possibilities to tune them to make them suitable for application in photovoltaics (Chapter 2) and thermoelectrics (Chapter 5).

Thanks also to a fruitful network of national and international collaborations, it was possible not only to study and engineer the material properties, but also, in the case of anodes for lithium ion batteries, to realize proper working devices.

For what concerns the basic investigation on Silicon nanostructures and on the PLD process to obtain them, as described in Chapter 2, the main goals were the understanding and tuning the material properties by means of a good control over its features –namely, porosity at the nanoscale and formation of nanocrystals. Under some specific process conditions, the fabrication allowed to grow hierarchically nanostructured films composed of Si nanocrystals embedded in a columnar porous amorphous matrix. A thorough investigation revealed the formation not only of “bulk” crystals, but also of amorphous-crystalline core-shell and core-shell-shell embedded nanostructures.

The fabrication of silicon nanocrystals via PLD represents a good alternative, with respect to the existing literature, to obtain these structures at room temperature without any further high-temperature steps and offers the possibility to tailor the properties of the crystals and of the amorphous matrix. Si nanocrystals can find application in various energetic fields, with Quantum-Dot photovoltaics being one of the most challenging ones. Up to now, though, the partially oxidized amorphous silicon matrix is not believed to provide sufficient electrical conductivity to be suitable for straightforward integration in a solar cell device, but the proposed approach can nevertheless be developed more extensively to address this target, e.g. by further reducing oxidation, and/or doping the matrix.

Also nanoporous silicon can be successfully applied to several fields related to the energy generation and storage, as shown for the core research work of this dissertation, i.e. the development of nanostructured porous Si anodes for Lithium-ion batteries. In this framework, this dissertation shows a study of innovative solutions to address the two main drawbacks of silicon anodes in lithium ion microbatteries, i.e. volume expansion and SEI, by means of suitably designed anodes.

The Si nanostructures synthesized by PLD and thoroughly characterized, showed in fact characteristics and properties suitable for interesting exploitation in this field and have been then optimized for this purpose. In particular, as described in Chapter 3, silicon-carbon anodes have been prepared, based on PLD as a fabrication process, with different approaches. All the proposed solutions rely on coupling the ability of porous silicon to accommodate the large volume expansion during lithiation and the stabilizing effect of carbonaceous layers from a chemical (stable SEI layer) and mechanical (buffering effect) point of view. Thanks to Si/C coupling, all the proposed anodes show very good stability over cycling, even reaching up to 1000 cycles. Among the anode architectures proposed, the one based on a Si layer deposited on a substrate made of carbon nanotubes allows for obtaining self-standing flexible anodes, heading for application in bendable devices. In all cases, the approach to fabrication has been led by the need to minimize the processing effort, both in terms of number of steps required and of temperatures involved, so as to orient the work to possible up-scaling.

Moving to larger scale production, the work described in Chapter 4 deals with the fabrication of Si/C anodes from slurries involving nanometric powders (Si), using methods and techniques typical of the industrial production. This activity was developed during a period of three months spent at the Project Competence-E group at Karlsruhe Institute of Technology (KIT), Karlsruhe, Germany. The author prepared the anodes from powder to cell and tested them electrochemically. Feasibility of partial substitution of Si for graphite with a drop-in approach in current productive processes has been shown, but further optimization is surely needed for what concerns slurry composition and fabrication process parameters. Despite the fact that this work is somehow self-standing for what concerns techniques and aims, continuity with PLD-films can be found in the scale that features the anodes developed at KIT, which are based on silicon nanoparticles and keep, also in their final structure, a nanostructured morphology.

On the way to large-scale fabrication of Si/C slurry-based composite anodes, this first study aims at defining a starting point and outline a strategy for improvement. Future developments of this work should include optimization of the processing steps that most affect, at this stage, the mechanical properties of the film, in particular mixing and calendering.

As from the existing literature, another possible application for nanoporous silicon is the field of thermoelectric materials. Although proper thermoelectric characterization has not been performed, the nanostructured Si grown by PLD showed properties potentially interesting for an application in this field. Controlling the porosity provides a means to reduce the thermal conductivity with respect to the bulk material, which is one of the key figures to evaluate a thermoelectric material. Chapter 5 investigates then the possibility of tailoring thermal conductivity of nanostructured silicon films grown by PLD. The study shows that, by nanostructuring during growth, it is possible to obtain a notable reduction in thermal conductivity of the films, making them promising candidates to become low-cost thermoelectric materials. Perspective work should focus on the parallel improvement of thermal and electrical conductivity by materials designing and process optimization and on the measurement of the Seebeck coefficient.

Acknowledgements

I thank the Italian Institute of Technology (IIT) for founding my research activity at the Center for Nanoscience and Technology (CNST-IIT) led by Prof. Guglielmo Lanzani in Milano, Italy, through a dedicated scholarship.

Besides the work done, the invaluable wealth I can carry along from this adventure lasting three years are the people who travelled with me, either for a just a short path or for the whole distance.

Starting from the people geographically far away, I thank the groups that hosted me for the periods spent abroad. Prof. Alex Yan and Dr. Ulaganathan Mani of the Nanyang Technological University in Singapore have kindly supported my stay, made cheerful by my flatmates, Vivi and Alan. A special thanks goes then to the whole Competence-E group, led by Dr. Joerg Kaiser at the Karlsruhe Institute of Technology, Germany. They taught me very much, both from a scientific and a practical point of view. In particular, besides Dr. Kaiser's guidance, very helpful was the support of Dr. Madhav Singh, who kindly shared his time and knowledge. Thanks Ramona Hahn, Olivia Wiegand, Valentin Wenzel, Steffen Schmelzle, Kevin Stella, Johannes Schauer, Boris Bitsch.

My thanks go to all of the people I collaborated with, who made this adventure possible with their expertise, be they far away or close-by: all of the people at the Energy Department of the Politecnico di Milano, with special mention to Dr. David Dellasega and Dr. Valeria Russo; Dr. Rosaria Brescia and Ms. Alice Scarpellini of the IIT in Genova, Italy, for a longlasting fruitful collaboration; Dr. Ming Xie of the Boulder University in Boulder, CO, US; Mazdak Hashempour of the Politecnico di Milano; Katrin Bertram and Hartmut Leipner of the Martin-Luther-Universitaet Halle-Wittenberg in Halle, Germany. My special and cheerful thanks go then to Dr. Nadia Garino of the CHSR-IIT in Torino, Italy, for her tutoring on lithium-ion batteries. I owe much to her valuable and kind support.

Looking closer, I cannot miss to aknowledge all of the people working at the CNST-IIT, who made this experience rich, round and unforgettable. In particular, I like to mention my cheerful mates of the PLD group for making life in the lab as rich as I could not even hope for. We have explored the meaning of being a team and I believe I got much more than what I left.

Finally, I would like to express my deepest gratitude to Dr. Paola Bruno and Prof. Andrea Li Bassi for supervising my research activity in this long adventure. They have been invaluable mentors, providing guidance, sustain, careful revision: but, above all, I sincerely thank them for encouraging me to develop my own new ideas. I learned much from them.

My thanks go then to my family, who never failed to support my choices, and to my boyfriend, who fills my days with joy.